

Automated Rockfall Detection from Thermal Imaging

Development and Application of Automated Rockfall
Recognition Using Computer Vision Approaches Applied to
Thermal Video

FINAL REPORT

PREPARED FOR

NATIONAL INSTITUTE OF OCCUPATIONAL SAFETY AND HEALTH
BAA#: 75D301-22-R-61070

PREPARED BY

GEOTECHNICAL CENTER OF EXCELLENCE
School of Mining and Mineral Resources
The University of Arizona

Contents

1	Executive Summary	3
2	Introduction.....	6
3	Project Personnel.....	8
4	Automated Rockfall Detection.....	9
4.1	Thermal Imaging for Rockfall Detection	9
4.2	Algorithmic Process.....	9
4.2.1	Tailoring Results to Sites	11
4.3	Deployment and Testing.....	11
4.4	Alarming, Recording, and Georeferencing.....	13
4.4.1	Alarming for Hazardous Fall Events	13
4.4.2	Recording for Further Analysis.....	14
4.4.3	Georeferencing.....	15
4.5	Research Findings and Future Work.....	19
5	Rockfall Monitoring System Developments and Upgrades	21
5.1	Mobile Monitoring Platform	21
5.2	Development of a Prototype Tactical Rockfall Monitoring System	22
5.2.1	Technical Specifications	23
5.2.2	Design Considerations for Extreme Environments	24
5.2.3	System Installation, Transport, and Portability	24
5.2.4	Issues Encountered	25
5.3	Future Work.....	25
6	Rockfall Forecasting based on Empirical Correlations and Statistical Modeling.....	27
6.1	Data Collection and Collation	27
6.1.1	Rockfall Data Collection and Collation	28
6.1.2	Meteorological Data.....	30
6.2	Data Analysis	35
6.2.1	Data Validation	35
6.2.2	Exploratory Data Analysis.....	35
6.2.3	Logistic Regression Modeling	38
6.3	Discussion	42
6.4	Limitations and Future Work	46
7	Knowledge Dissemination and Impact	47
7.1.1	Journal Articles	47
7.1.2	Refereed Proceedings	47

- 7.1.3 Presentations47
- 7.1.4 Educational Outreach Events48
- 7.2 Student Involvement and Impact.....48
- 8 Conclusions and Future Work49
 - 8.1 Development of Marketable Tactical Thermal Rockfall Monitoring System49
 - 8.1.1 Comparison with Alternative and Complementary Technologies.....50
 - 8.2 Development of Prototype Strategic Thermal Monitoring Tools50
 - 8.3 Rockfall Forecasting and Statistical Modeling51
- 9 Acknowledgments52
- References53
- Appendix A: Details of Automated Rockfall Detection Process.....55
 - A.1: Overall Algorithmic Process55
 - A.2: Movement Tracks.....55
 - A.3: Create Averaged Background55
 - A.4: Compare current image to background.....56
 - A.5: Identify motion regions56
 - A.6: Motion prediction57
 - A.7: Track assignment.....57
 - A.8: Evaluate Movement58
 - A.9: Alarm58
 - A.9.1: Visual58
 - A.9.2: Audio59
 - A.9.3: File output.....59
- Appendix B: Meteorological Data and Modeling Results60
 - B.1 Precipitation Events60
 - B.2 Weight of Evidence and Information Value61
 - B.3 Logistic Regression Outputs70
 - B.4 Meteorological Summaries72
 - B.5 Meteorological Trends.....73
 - B.6 Receiver Operating Characteristic Curves.....74
 - B.7 Coefficients, Odds Ratio, P-Values, and Confidence Intervals for Preliminary Model Runs. ..75
- Appendix C: Data Access78

1 Executive Summary

This document is the Final Report for the “Development and Application of Automated Rockfall Recognition using Computer Vision Approaches applied to Thermal Video from Open Pit Mines” project (NIOSH BAA#: 75D301-22-R-61070), referred to herein as the Automated Rockfall Recognition Project. This work represents the second phase of the Geotechnical Center of Excellence’s (GCE) research into the use of long-wave infrared (thermal) cameras as a solution for detecting, tracking, and alarming for rockfall in open pit mining environments. The Phase 1 Application Testing Project showed that rockfall can be reliably observed in the thermal infrared. Phase 2 has produced an algorithmic solution that automatically detects and alarms for rockfall in real-time, which marks a significant advancement in monitoring and mitigating rockfall hazards in mining environments. A list of significant observations and recommendations is provided below.

1. **Algorithm Development.** Phase 2 successfully developed an automated method for detecting and alarming for rockfall events using thermal video. The algorithm operates efficiently on hardware with limited processing power, making it suitable for deployment on rugged laptops without high-end GPUs. The detection system tracks multiple objects, utilizing predictive filtering and motion heuristics based on object movement rather than predefined shapes. This approach eliminates the need for machine learning and retraining, ensuring consistent performance across varied environments.

The technology readiness level (TRL) of the prototype system is estimated at a TRL6 as automated detection has been successfully demonstrated in relevant environments. Future work includes refining the algorithm, enhancing data acquisition systems, and incorporating feedback from industry focus groups. Continued development will focus on creating a commercially viable solution for tactical monitoring of safety-critical areas, with potential applications extending to failure forecasting based on empirical correlations. Future advancements will enhance algorithm efficiency, incorporate additional geotechnical applications, and improve user interfaces for diverse hardware environments. Predictive capabilities based on meteorological data will be expanded, and alarming systems will be refined to include frequency-based triggers for prediction of larger slope instabilities.

2. **Prototype Tactical Monitoring System.** A prototype tactical monitoring system was developed, featuring a thermal camera, rugged laptop, and robust power system, designed for deployment in extreme environments. The system's design ensures operational efficiency and adaptability, with future work focused on enhancing its portability and reliability.
3. **Deployments and Testing.** The automated rockfall detection algorithm and prototype tactical monitoring system were tested during a series of deployments over three stages:
 1. Initial deployments at the San Xavier student mining laboratory (SX Mine) and a Nevada mine site highlighted issues with remote connection and power reliability, which were addressed in subsequent troubleshooting.
 2. Secondary deployments to local sites and testing focused on achieving real-time detection using the prototype tactical monitoring system’s hardware, revealing processing power limitations that were mitigated through algorithmic optimizations and multi-core processing.
 3. Further deployments to sites near the University of Arizona including the SX Mine were conducted to test more-efficient software versions. The improved software

demonstrated successful real-time motion processing with video archiving, resolving previous lag issues.

Testing revealed the need for a lightweight, efficient algorithm suitable for slower computing hardware and identified non-critical software features for removal. The system's portability and ease of setup can be improved, and future iterations will address power system reliability and reduce deployment complexity.

- **Rockfall Forecasting.** Data collection and analysis from thermal video and meteorological recordings provide insights into the factors influencing rockfall initiation. The report details a methodology for processing and analyzing this data, highlighting the potential significance of solar irradiance and precipitation in forecasting the probability of rockfall.
- **Recommendations for Future Work.** Additional research paths and recommended future work resulting from this project include:
 1. Comparison with alternate and complementary technologies. The thermal rockfall monitoring solution developed as part of this project will provide important cross-validation functionality and has the potential to improve the effectiveness and reliability of other rockfall detection systems. The prototype software and data collection system should be thoroughly evaluated against complementary monitoring solutions (e.g., Doppler radar, LiDAR, photogrammetry) using a quantitative assessment framework.
 2. Development of prototype strategic thermal monitoring tools. Observations made by the GCE, along with prior studies, suggest additional geotechnical use cases for thermal imagery that have the potential to enhance miner safety (e.g. Guerin et al., 2019; Schafer et al., 2023; Rosser et al., 2007). Potential strategic applications to be explored further include:
 - a. Detection, delineation, and evolution of groundwater seeps.
 - b. Quantitative evaluation of catch bench performance.
 - c. Monitoring of large-scale slope instabilities to inform slope management and time-of-failure predictions (Schafer et al., 2023; Rosser et al., 2007).
 - d. Systematic methods for characterization of rock bridges (Guerin et al., 2019).
 3. Further development of the algorithm and data collection system to a marketable monitoring software. The Phase 2 prototype software establishes a groundwork for developing a commercially viable software system to detect, track, and alarm for rockfall. Additional work is needed prior to commercialization, including:
 - a. Gathering feedback from industry focus groups, incorporating research findings regarding complementary technologies, and developing a front-end user interface to increase usability and facilitate deployment across various operating systems and hardware.
 - b. Researching necessary hardware, power systems, and computing capabilities to improve the prototype.
 4. Additional research toward rockfall forecasting. Preliminary correlations between rockfalls detected using the Phase 2 algorithm and concurrent meteorological data highlight the potential to forecast the probability of rockfall events based on environmental forces. Continued research on this topic should include:

- a. Strategic deployments of our mobile thermal rockfall detection system specifically targeting rockfall data collection in a variety of climates through seasonal weather patterns, heavy dust/smoke particulates, inclement weather events, and other meteorological phenomena.
- b. Exploring advanced statistical methods and machine learning algorithms to further investigate potential correlations and assess their potential to forecast probabilities of rockfall.
- c. Testing equipment installed on the slope of interest for in-situ data collection of meteorological parameters and surface temperatures at the rock face. This will reduce uncertainties related to measurements acquired at varying distances from the slope.

2 Introduction

The Geotechnical Center of Excellence (GCE) at the University of Arizona has identified the use of thermal infrared cameras and computer vision algorithms as a potential solution for detecting, tracking, and alarming for rockfall in open pit mining environments. Thermal cameras are particularly valuable as monitoring tools due to their ability to provide situational awareness throughout the diurnal cycle and in various lighting and atmospheric conditions where visible-light cameras have reduced effectiveness. This allows for near-continuous real-time monitoring, which is crucial for the detection of potential hazardous movements and the initiation of preventative measures to protect both personnel and equipment. Thermal cameras can detect rockfall due to the thermal gradient that occurs across surface rocks exposed to solar heating and atmospheric cooling and underlying rocks which heat and cool more gradually. This differential heating and cooling gives rocks dislodged from the surface of a pit slope different thermal signatures relative to the surrounding rock face and the freshly exposed rock. This variation in thermal properties allows the exposed, falling, or scoured rock surfaces to be detected using thermal imaging.

The work presented here represents the second phase of the GCE's research into the use of thermal infrared cameras as part of a comprehensive rockfall monitoring solution. The Application Testing Project, referred to herein as Project Phase 1, established the effectiveness and reliability of thermal imaging cameras to detect and document rockfall events in surface mining operations. Specific aims of project Phase 1 included:

1. Characterization and alignment of necessary parameters for rockfall detection with capabilities of existing commercial off-the-shelf (COTS) thermal imaging systems.
2. Implementation of a testbed Mobile Monitoring Platform (MMP) to enable systematic evaluation of six representative COTS cameras with mine operators.
3. Development of a process model to inform detection and identification of rockfalls from thermal imaging videos and understand the feasibility of human monitoring with thermal imaging systems.
4. Evaluation of the MMP prototype system by conducting a series of tests under a variety of realistic mining conditions at nine open-pit mines across the western US and Canada.

At the conclusion of Phase 1, rockfalls were identified via manual inspection of recorded thermal video, which is time- and cost-prohibitive. The primary goal of Phase 2 was to develop an automated rockfall recognition system for open pit mines using thermal video cameras to detect and alarm for rockfalls in real time, facilitating geotechnical risk management and increasing safety. This report details the accomplishments and findings of Phase 2, which included three aims:

1. Development and application of an automated detection algorithm using long-wave infrared (LWIR) thermal video.
2. Deployment and testing of a prototype system for real-time, tactical monitoring of rockfall in open pit mining environments.
3. Empirical analysis of the relationship between rockfall and meteorological factors to provide insight into times of increased risk for rockfall.

Section 4 of this report documents the results of Phase 2, Aim 1, which produced an algorithm to automatically detect and alarm for rockfall in real time using COTS thermal cameras and computer hardware. This algorithm has been demonstrated on rockfall from multiple mine sites, including over

3,800 hours of thermal video from two Phase 1 sites. The algorithm performance was evaluated using one week of thermal video taken prior to the Leo failure at the Bingham Canyon mine, indicating comparable rates of rockfall detection between the algorithm and a human observer and illustrating an exponential acceleration of rockfall events prior to failure (Schafer et al. 2023). Section 5 discusses Phase 2, Aim 2, which identified desirable video characteristics, including data collection and storage methodologies, for use in automated rockfall detection. A prototype standalone tactical system was also developed that can run the detection algorithm in real-time and may be deployed in minutes by a single operator. Section 6 documents Phase 2, Aim 3, which evaluated environmental conditions to determine their effect on the likelihood of rockfall. Environmental data from multiple sources was evaluated across the entire deployment period for two mine sites, revealing a statistically significant effect of both solar irradiance and rainfall intensity on rockfall occurrence.

3 Project Personnel

The success of the Phase 2 Thermal Imaging Project was made possible through the collaborative efforts of the GCE research team. Each team member brought unique skills and expertise to the project, contributing to successful completion of overall project objectives and milestones. Contributors included:

- **Brad Ross, Principal Investigator.** Dr. Ross led the project by setting the strategic vision, ensuring alignment with project goals and overseeing major project decisions.
- **Julia Potter, Co-Principal Investigator.** Potter was responsible for the overall management of the project, coordinating team activities, oversight of the project budget, and ensuring that milestones were met.
- **Leonard Brown, Co-Principal Investigator.** Dr. Brown contributed expertise in algorithm development, ensuring the quality and accuracy of the code and prototype software.
- **Chad Williams, Co-Principal Investigator.** Dr. Williams provided critical advice on the practical applications of monitoring technologies and strategies for effective deployment in the field.
- **Benjamin Meyer, Software Engineer.** Meyer developed the necessary algorithms for the thermal imaging project, working closely with the PI and Co-PIs to implement and refine the software solutions.
- **James McNabb, Senior Engineer.** McNabb supported project management tasks and participated in fieldwork activities, ensuring smooth execution of field operations and data collection.
- **Bobby Prescott, R&D Engineer.** Prescott assisted with development of prototype data collection system, including interfacing with manufacturer (GroundProbe), and with field operations and data collection.
- **Christian Ortmann, Computing Sciences Researcher.** Ortmann focused on the empirical correlation of thermal imaging data, working under the guidance of senior team members.
- **Rahul Jadhav, Undergraduate Researcher.** Jadhav contributed to the project by reviewing thermal video footage from Phase 1 and documenting instances of rockfalls.
- **Gavin Hughes, Undergraduate Researcher.** Hughes assisted with gathering and organizing weather data and testing portability and ease of setup of the prototype tactical system.
- **John Keefner, Project Advisor.** Keefner offered valuable feedback and insights on the applications of monitoring technologies and their deployment strategies, helping to shape the practical aspects of the project.
- **Jose Restrepo, Graduate Research Assistant.** Restrepo worked on upgrading the MMP under the supervision of the Senior Engineer.
- **Yash Sihag, Undergraduate Researcher.** Sihag assisted in compiling and organizing the final report.
- **Greatness Ojum, Undergraduate Researcher.** Ojum reviewed Phase 1 thermal footage, documenting instances of rockfalls and guided Phase 2 undergraduate researchers with rockfall documentation procedures as needed.
- **Daouda Berthe, Undergraduate Researcher.** Berthe reviewed Phase 1 thermal footage, documenting instances of rockfalls.

4 Automated Rockfall Detection

An automated method of detecting and alarming for rockfall and other hazardous falling objects has been developed as part of project Phase 2, Aim 1. The automated tracking system utilizes long-wave infrared (LWIR or “thermal”) video to monitor rockfall at all stages of the diurnal cycle, through dust and light-to-moderate precipitation. The automated detection approach is driven by the characteristics of the prototype system hardware and by our subject matter (falling rock). The Dell Rugged Latitude laptop used in the prototype system includes an Intel I7-8650U processor and lacks an NVIDIA graphics processing unit (GPU). Operating within these hardware constraints required the use of a CPU-based algorithm that does not leverage Compute Unified Device Architecture (CUDA)-based parallelism that could be run on an NVIDIA GPU. The prototype tactical system’s processor limitations have necessitated prioritizing computational efficiency during development, resulting in an algorithm that does not require a high-end CPU or graphics card to run in real time.

Rockfall can include large and easily visible singular rocks, slides of aggregate material, or falling objects that are only evident on thermal video from the scouring left by their impact with the rock face. Due to the irregular structure of slope surfaces in open pit mines and similar environments, rockfall can drastically change direction and shape from frame to frame as falling objects are deflected, broken apart, or dislodge other material. Based on these characteristics, the algorithm utilizes predictive filtering and motion heuristics, in which multiple objects are simultaneously tracked and their movements are characterized as hazardous or not.

4.1 Thermal Imaging for Rockfall Detection

Commercially available uncooled thermal cameras are low resolution and record at slower frame rates when compared to modern visual-light cameras. Despite these drawbacks, thermal cameras are capable of operation day or night, through light to moderate particulates such as dust or smoke, and in conditions of light to moderate precipitation that would render visual-light cameras ineffective. As rocks dislodge or impact slopes, there is a thermal difference between the freshly exposed or scoured area and the surrounding rock face, as well as between the falling rock and the surrounding face. These differences are detectable through thermal imaging and can provide greater contrast than may be seen with a visible-light video of rocks falling past similarly colored material. Phase 1 of our project proved that thermal cameras are effective in revealing rockfall throughout the diurnal cycle and in extreme ambient temperatures (ranging from -32°C to 50°C).

4.2 Algorithmic Process

A software algorithm has been implemented to detect and characterize object motion and then to issue alarms where appropriate. The rapidly changing shape of rockfall events based on the interaction between moving or fragmenting rock and underlying slope structure makes the subject material very difficult to characterize or track based on similar corners or edges as is done in most machine learning methods of object recognition and tracking. This reinforces the need for a solution based on how an object moves rather than the object’s specific characteristics (size, shape). The algorithm for rockfall detection and tracking consists of the following steps:

- 1. Background Generation:** To minimize detections due to pixel flicker in thermal video, we generate a background image from the average of the previous 50 frames. This is used to minimize false motion detections from slight brightness flickering of pixels (common in this style of thermal camera).

2. **Background segmentation:** The resulting background image is then compared to the current frame of video, and any pixels varying in intensity from their corresponding background are identified as possible moving objects.
3. **Blob Detection:** These motion detections are grouped into areas or regions of motion by combining nearby pixels. This consolidates close movement detections, allowing the system to more efficiently characterize motion than would otherwise be possible.
4. **Location Prediction:** Expected locations for all previously identified moving objects are estimated using predictive Kalman filters (Kalman, 1960). These filters consider previously known locations of the object plus current velocity to judge likely location.
5. **Track Assignment:** Observed current-frame motion is compared with the expected locations of all previously identified moving objects using a Hungarian/Munkres algorithm with thresholding (Munkres 1957). Motion near the predicted location of tracked objects is used to extend movement paths. Motion outside of those matches causes the creation of new track assignments (recognition of new moving objects). Any other identified objects are flagged as “unseen” until motion is visible along an object’s expected path.
6. **Motion Characterization:** The paths of all identified moving objects are evaluated against the characteristics of a “hazardous falling object”. For this study, characteristics used to define hazardous fall include direction and speed of movement (velocity).
7. **Alarming:** Alarms are triggered when tracked objects meet the motion characterization criteria. Alarm options currently include screen representation of motion path, audio alert, console/JSON outputs, or logging to text or CSV files.

Figure 4-1 presents an example of the algorithm’s tracking results on a human-initiated rockfall. Figure 4-2 illustrates important algorithmic steps and results on rockfall caused by a planned blast at an open pit mine. The automated rockfall detection can focus on rockfall of different scales and shapes and can track a single object or multiple fall events simultaneously.

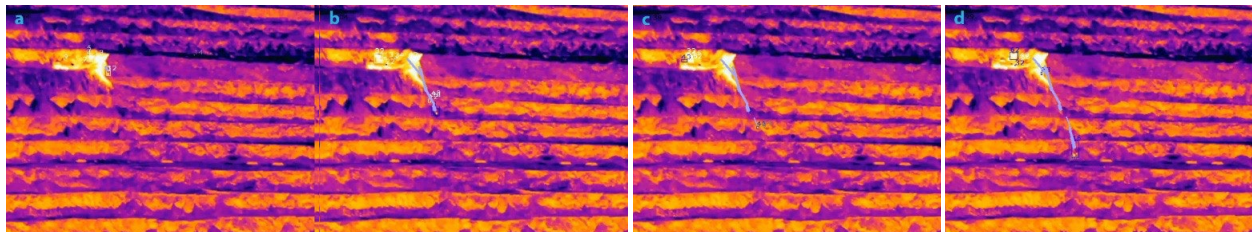


Figure 4-1. Example of algorithm tracking results on a human-initiated rockfall. a) frame taken one second after initial detection of rockfall. b) frame taken six seconds after initial detection of rockfall. c) frame taken eight seconds after initiation of rockfall. d) frame taken thirteen seconds after initiation of rockfall.

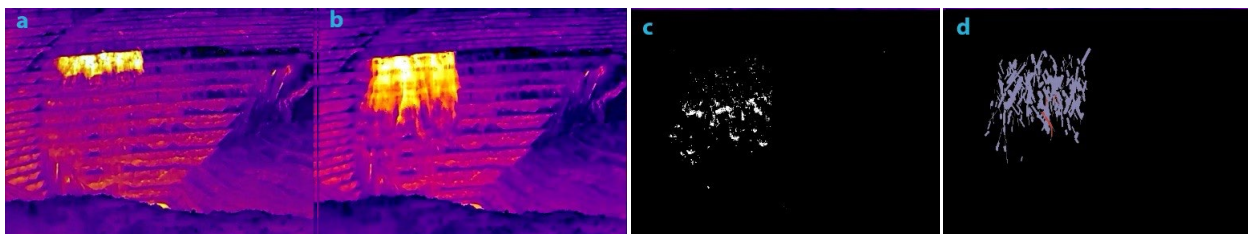


Figure 4-2. Example of algorithm performance on rockfall caused by a planned blast at an open pit mine. a) frame taken 7 seconds after blast event. b) frame taken 15 seconds after event. c) subtracted background showing instantaneous differences / motion in current frame vs previous 50 frames, taken 15 seconds after event. d) tracked fall detections from start of video clip to current frame.

4.2.1 Tailoring Results to Sites

A preliminary graphical user interface (GUI) was developed to enable tailoring of the algorithm to site specific requirements. Key parameters for background segmentation and motion characterization are defined by the user based on deployment site characteristics. These include video stabilization options, controls for minimum and maximum speeds for a fall detection, how long a tracked object can be stationary or unseen before being retired from consideration, maximum distance that a motion could be considered as part of an existing fall, and which angles of motion should be considered as hazardous falls. The GUI also includes a masking option to exclude areas of noninterest from consideration and methods for defining expected fall angles based on the orientation of the pit walls in the camera frame (Figure 4-3).

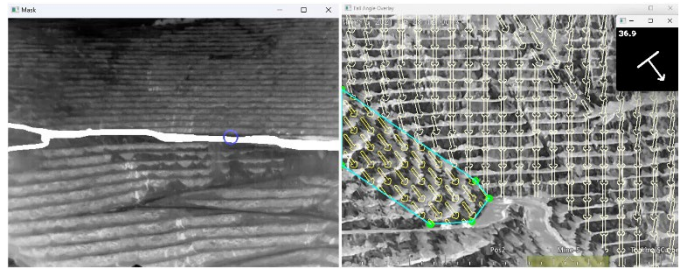


Figure 4-3. Interface options for site characterization, including an example of the masking feature applied to an active haul road (left) and an example of user-defined expected angle of rockfall for deployment sites without three-dimensional topographic data (right).

4.3 Deployment and Testing

The automated rockfall detection algorithm and prototype tactical monitoring system were tested during a series of deployments over three phases:

1. Initial deployments of the prototype system and a preliminary version of the algorithm were completed at the San Xavier student mining laboratory and a Nevada mine site. These tests highlighted issues with remote connection and power reliability, which were addressed in subsequent troubleshooting.
2. The prototype system was re-deployed at the SX mine with an updated version of the algorithm to evaluate real-time detection performance. These tests revealed computing performance limitations that were mitigated through algorithmic optimizations and multi-core processing.
3. The final testing stage was again conducted at the SX Mine. During this phase, the improved software demonstrated successful real-time motion processing with video archiving, indicating that the issues observed during testing Phases 1 and 2 had been resolved.

More details about the test deployments and lessons learned are summarized in the following subsections.

Testing Stage 1 – Video Archiving and Recording (August – September 2023). Initial deployments consisted of several tests at the University of Arizona (UArizona)’s SX Mine in August 2023. Testing at the SX Mine yielded successful recording and archiving of thermal video. The system was subsequently deployed in September 2023 for two days of testing at a mine in Nevada. Several issues were encountered during testing at the Nevada Mine. The system was able to record and archive video during the first day of testing, but remote connection was unsuccessful. There was also significant lag in tracking live rockfalls. After troubleshooting, the system was deployed for a second day of testing to archive video without simultaneous tracking. During this time, the power components of the prototype system experienced an unexplained failure which ended data collection earlier than anticipated. The system was transported to GroundProbe’s Tucson facility for

troubleshooting, where the issue was identified as a faulty charge controller and addressed. However, concerns regarding the reliability of the power system persisted due to intermittent outages during subsequent deployments which persisted through stages 2 and 3. Future deployments were limited to mines within driving distance of UArizona to allow for more efficient troubleshooting.

Testing Stage 2 – Initial Algorithm Implementation (October 2023). A second phase of testing performed between the GCE’s offices on the UArizona campus and at the SX Mine commenced in October 2023. This phase focused on assessing the system’s ability to perform real-time detection. While the prototype successfully detected movement in real-time, limitations in the laptop computer’s processing power were observed. The system was not able to concurrently perform real-time detection while also archiving recorded video for subsequent analysis.

Testing Stage 3 – Algorithm Optimization (October 2023 – March 2024). The issues observed during Testing Phase 2 provided valuable insights that led to improved algorithm efficiency. Each stage of the algorithm was evaluated to determine causes of delay and potential processing improvements as follows:

- Roughly 15% of the algorithm’s processing time was consumed by an optical flow calculation used only in the video stabilization operation on the camera input. Phases 1 and 2 of testing revealed no significant detection benefits resulting from the stabilization process, so the video stabilization step was removed.
- Archiving the original thermal video without the algorithm outputs accounted for roughly another third (32%) of processing time. Archiving original video will be optional in a production version of the system but is vital during development as it allows the original video to be re-processed using the latest software improvements.
- Another 18% of processing time was spent waiting for user interaction (checking for user keystrokes, etc.). No opportunities for efficiency improvements were identified for this necessary step.
- Initial versions of the algorithm ran on a single CPU core and sequentially processed each frame of video, creating bottlenecks in the archiving, screen display, and user interaction steps.

The detection software was redesigned to take advantage of multiple CPU cores, allowing separate processes to handle motion detection, alarming, video archiving, etc., and improving the overall speed and efficiency of the software. A comparison between the sequential and multiprocessing versions of the software was performed in October 2023, using two example videos (one showing a human-induced single rockfall and one showing a 12-minute video of secondary rockfall following the Leo failure event at Bingham Canyon Mine on May 31, 2021). Both source videos were recorded at 15 frames per second, and both were tested using the development laptop’s Intel i9-12900H processor. Comparison results are outlined below:

- Processing the human-induced rockfall test video with 668 frames:
 - The sequential algorithm finished in 26 seconds (25.7 FPS)
 - The multiprocessing algorithm finished in 11 seconds (60.7 FPS)
- Processing the post-Leo failure video with 10,982 frames:
 - The previous sequential algorithm finished in 438 seconds (25.1 FPS)
 - The new multiprocessing algorithm finished in 162 seconds (67.8 FPS)

Detection results were identical between the two algorithm versions on each example video, indicating that the increase in speed did not cause any loss in effectiveness. The shorter video processing speed was improved by a factor of 2.3×, while the longer video processing was improved by a factor of 2.7×. This outcome reflects the cumulative effects of bottlenecks in sequential processing that become more pronounced on longer inputs.

Testing with the improved software solution running on the prototype tactical system's hardware was completed between January and March 2024. This testing involved real-time processing on live video from three minutes up to 11 hours. The first successful live testing of the multiprocessing algorithm's output on human-initiated rockfall was done at the University of Arizona San Xavier Mining Laboratory site on January 26. Six human-initiated rockfall events were recorded during this test. The algorithm was able to run in real time, processing rockfall detection/tracking and producing two video output streams (original unprocessed video and detection results video). The original video recording allowed for masking and re-running the algorithm after returning from the site (also on the same hardware). Observations from this test included:

- The unmasked algorithm output detected 5 of 6 human-initiated rockfalls, as well as multiple non-rockfall events caused by moving vegetation.
- After masking vegetation patches and regions outside of the slope the algorithm successfully identified all 6 human-initiated rockfall events and no false positive events.
- Both the masked and non-masked output registered and tracked secondary motion of rocks dislodged by the thrown rocks. Two of these events occurred during the test, and each was correctly identified as rockfall by both runs of the algorithm.
 - The unmasked test misidentified these secondary rockfalls as new rockfall events or associated them with vegetation-induced false positive events.
 - The masked algorithm test correctly associated the secondary rockfalls with their initiating “parent” rockfall events.

All field tests showed successful real-time motion processing with simultaneous archiving of video, indicating successful resolution of the lag issue discovered in Testing Phase 2.

4.4 Alarming, Recording, and Georeferencing

To be useful for improving personnel safety and slope stability awareness, the rockfall tracking algorithm must include methods to alert for and record tracked hazardous fall events. As seen in Figures 4-1 and 4-2 in Section 4.2, one such alerting method is visual. The algorithm can also generate audio alerts. Textual records are written to external files for future analysis, and the algorithm can also store visual results of rockfall tracking or copies of the original video feed. Georeferencing can also be performed to link 2D locations of rockfall with 3D points on an existing map of mine sites. Taken together, these features provide a framework for accurate, repeatable, and verifiable location of detected rockfall events.

4.4.1 Alarming for Hazardous Fall Events

Video alerting. As rockfall events are detected, the algorithm displays a visible track of motion on screen. These tracks are separately identified and are individually colored to distinguish separate events that are simultaneously visible or even simultaneously occurring. Figure 4-4 depicts the results of the automated rockfall detection algorithm on several human-initiated rockfall events at the SX Mine. Note that some colors are used in multiple movement tracks. This is due to two of the

falling rocks dislodging other material, which moves and is tracked separately but still associated temporally and spatially as the same event.



Figure 4-4. Still image depicting multiple rockfall traces from a test of the prototype tactical system at the SX Mine. Each color overlaying the grayscale background indicates a separate fall event (some of which include a secondary fall representing dislodged material). Line thickness varies based on the amount of moving material observed.

Audio alerting. The automated rockfall detection program can currently generate audio alerts if running on a Windows-based computer system. The default audio alert is a Windows system error sound, and repeats every 0.5 seconds while an active fall event is being tracked.

4.4.2 Recording for Further Analysis

The automated detection software offers multiple options for recording rockfall events. Such recordings can be used for archival purposes, reprocessing, or for export as data in other analyses.

Recording of rockfall video. The visual rockfall detection results can be written to a video file for record keeping or further analysis. Video output options include a single frame with a real-time overlay of tracked falling object paths or a three-frame side-by-side video showing original video feed, motion detection results, and tracked falling object paths (allowing easy visualization of why certain movements were classified as hazardous falling objects). Each subframe has the same resolution as the original video, for an overall output size with the same vertical resolution and three times the horizontal resolution as the input source.

Recording of original video feed. The unprocessed video input received by the algorithm can be separately saved to an archival video file. This allows for reprocessing the video with future, improved versions of the detection software.

Output to text files. The algorithm can write data to external text files (in plain text or comma-separated-value format) for use in record keeping and later analysis. Such textual records (including each detected event's time of initiation, its starting location, the video file source of the event, and the frame number of the event initiation) were used in the comparison between human and algorithm rockfall detection (Section 4.5) and in the empirical correlation portion of the project (Section 6).

4.4.3 Georeferencing

To enable more advanced alarming, a workflow for georeferencing fall events has been developed. This is used to provide site operators with three-dimensional coordinates that match their site positioning scheme, allowing for rapid delineation and communication of areas experiencing rockfall hazards. The Georeferencing workflow developed for this project requires the input of a 3D map such as those frequently generated by on-site survey teams for operations and planning. The initial setup for georeferencing is a multi-stage process and must be repeated occasionally as progressive mining alters the mine topography. The result is an efficient algorithmic process involving matching 2D screen locations of movement with a table containing the corresponding 3D georeferenced coordinates.

Outline of georeferencing process. The following stages are used in the georeferencing workflow:

1. **Camera calibration:** The thermal camera's intrinsic parameters are determined using a calibration grid tool which measures field of view, focal length, and linear distortion characteristics of the individual camera lens (Figure 4-5). The manufacturer camera specifications are insufficient for this determination because of potential inconsistencies or flaws in the camera lens production. This can lead to subtle image distortions that affect the 2D to 3D georeferencing calculations, with the error increasing as a function of the distance between the camera and the slope.

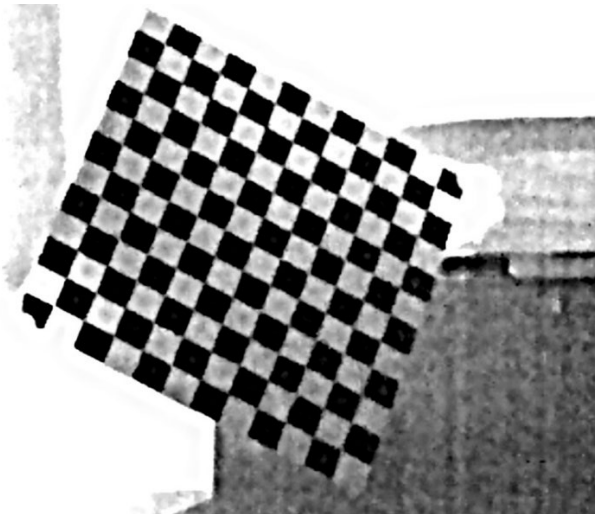


Figure 4-5. Thermal camera lens calibration device as viewed by the FLIR A400 camera: This device consists of a 16-gauge steel plate with a precise vinyl checkerboard pattern overlaying part of the surface. The thermal contrast between vinyl and exposed steel allows the thermal images to be used in standard calibration tools designed for visible-light cameras.

2. **3D mine representation:** A digital rendering of the mine site or area of interest is generated by drone photogrammetry, LiDAR scan, or other technology and saved as a point cloud. This can be viewed in 3D software such as CloudCompare (Figure 4-6). The location coordinates of the 3D mine representation will often be received in the site grid coordinate system with an offset applied (in CloudCompare or other software) to center the model on screen. This

offset must be noted, since it will be applied to 3D location values later in the process to ensure that the georeferencing output matches site grid coordinates.

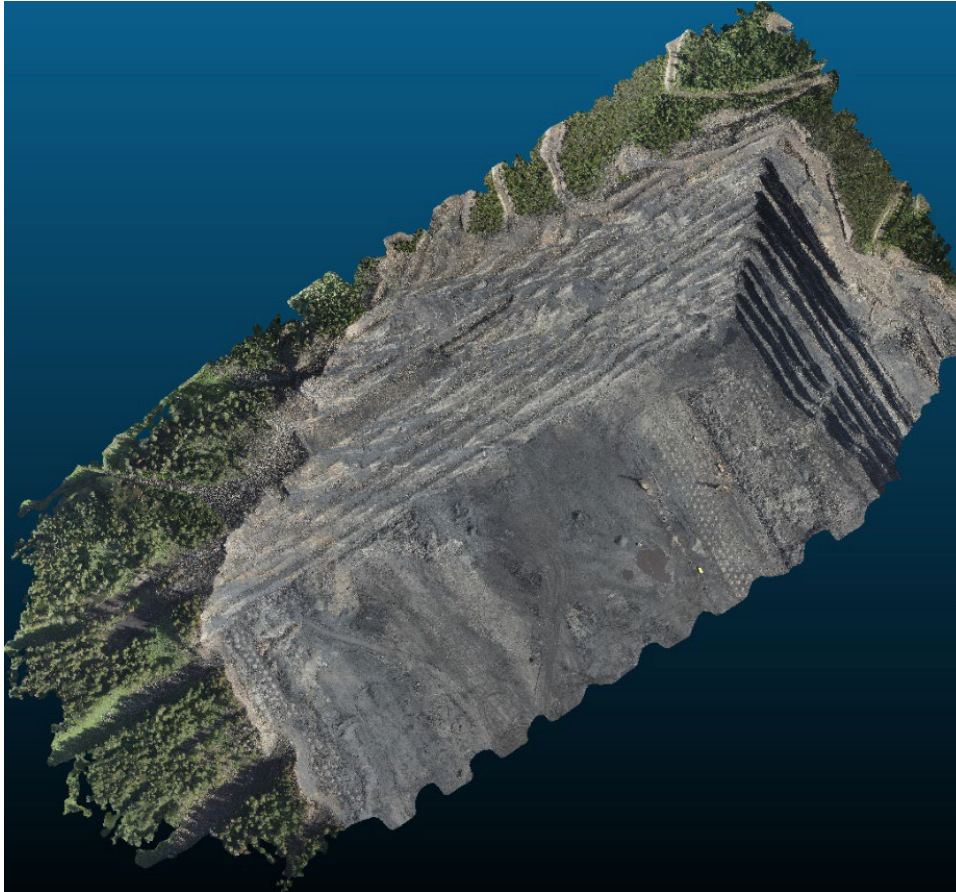


Figure 4-6. 3D point cloud collected from Mine 7, viewed in CloudCompare (top-down view).

3. DEM export and conversion: Using export options in 3D software such as QGIS, Pix4D, or CloudCompare, the 3D point cloud is viewed orthographically from above, converted into

elevation data, and exported as a grayscale TIFF or PNG image (Figure 4-7) or as a table of values representing the elevation of each point in the file.

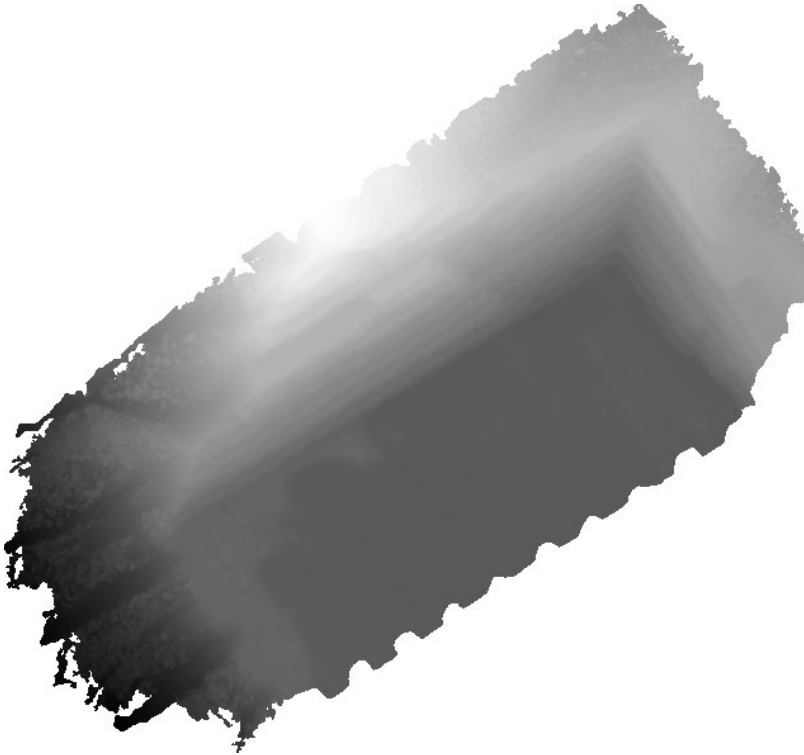


Figure 4-7. Grayscale heightmap generated from Mine 7 point cloud (lighter areas correspond to higher elevations).

4. Heightmap import to Unity: Either output from step 3 can be imported into Unity, a popular 3D development platform, and used to create a virtual duplicate of the slope face (Figure 4-8)



Figure 4-8. 3D model of Mine 7 pit slope generated in Unity from a digital elevation map (DEM) file

5. Camera placement in Unity: The unity camera is set at the same location (distance/elevation) relative to the target slope as the real-world camera at the deployment site (determined from the 3D point cloud and site reporting).
6. Per-pixel ray tracing: The Unity camera's view is set to the same resolution as the deployed thermal camera. Using raytracing techniques, a line is sent from the Unity camera's focal point through each resulting pixel and evaluated to determine whether (and where) that ray impacts the scene (Figure 4-9).

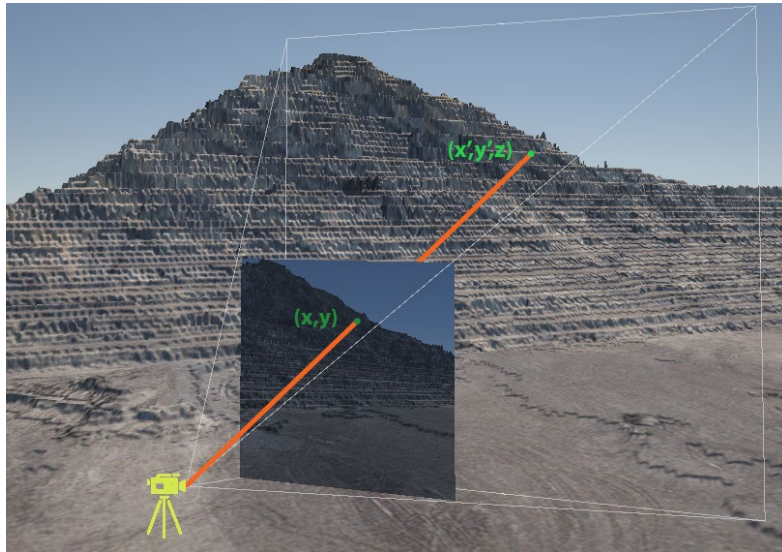


Figure 4-9. Raytracing for 2D to 3D correlation. A virtual camera is positioned in Unity to match the relative placement of a real-world thermal camera (placement shown by the yellow camera, with a field of view outlined in white). The camera generates a 2D image of the mine slope (shown as the rectangular inset image). A vector (or ray, shown as a thick orange line) is drawn from the virtual camera location through the 2D coordinate (x,y) at the camera's focus length and extends until it intersects the 3D slope model. The 3D location of the ray/slope intersect (x',y',z) is recorded.

7. Accounting for nonlinear distortion: A preliminary method of maintaining accuracy in cases of nonlinear (fisheye) lens distortion has been developed, using the distortion parameters provided by camera calibration in step 1 to adjust the direction of each ray cast in step 6. This distortion correction is still being tested at the end of the project period.
8. Generation of 2D to 3D projection map: The 3D location of each ray's intersection is output to a comma-separated values (CSV) file arranged by position of the original camera pixel.
9. Translation of 3D coordinates to mine grid: The CSV file resulting from the previous step contains Unity coordinates (accurate spatial coordinates from an arbitrary 3D origin point) rather than real-world locations. These must be translated to the mine grid used on site by adding the offset noted in step 2.
10. Export of projection map to rockfall tracking software: The finalized map of 3D equivalents for each pixel is imported to the rockfall detection algorithm as a two-dimensional array.
11. Dual 2D/3D outputs: In a method parallel to that used in masking regions of noninterest, the screen location of each tracked rockfall is compared to the imported 2D to 3D map, and

both screen coordinates and the corresponding real-world location are output by the algorithm.

Caveats for the georeferencing process. This georeferencing workflow uses a periodically generated 3D representation of the mine in order to locate real-world coordinates corresponding to 2D screen coordinates of motion detection. Due to this, the positional accuracy of the rockfall tracking algorithm's 3D output is directly dependent on the frequency of 3D updates from new photogrammetry/lidar/other surveys of the site. Additionally, the current method of accounting for nonlinear distortion due to lens curvature (the "fisheye" effect, which is likely to increase with wider camera field of view) is still being tested for accuracy. Finally, many mines use site-specific coordinate systems rather than longitude/latitude, UTM, or WGS84. The initial calculations of 3D coordinates from Unity to the Mine grid can be time consuming if the 3D representation of the mine received from the site is not a point cloud already calibrated to the site grid.

4.5 Research Findings and Future Work

Early versions of the rockfall detection algorithm were developed on significantly faster computers than the prototype tactical system's laptop and were tested using archived video rather than live rockfall events. The lag between real-time events and detection results in Testing Phase 2 highlighted the need for an algorithmic solution that was developed to perform well on slower hardware. Some initial assumptions of necessary features (such as automatic motion stabilization to counteract camera shake) were found to be non-critical during testing.

Comparisons to Human Rockfall Detection. The GCE's thermal video archives include recordings capturing the Leo slope failure at Bingham canyon mine as well as several days prior (acquired during Phase 1). This video was used in multiple papers (Wellman et al. 2022, Schafer et al. 2024) to demonstrate an increasing frequency of rockfall events prior to a major slope failure. Prior research using this video relied on manual selection of rockfall events. In May 2024, the automated rockfall detection algorithm was used to process the same video. A plot of the cumulative rockfall events observed by manual selection and automated detection is included in Figure 4-10. A comparison of detection locations for human and algorithmic rockfall detection is shown in Figure 4-10. The comparison reveals similar cumulative frequency curves between human and automated rockfall detections, although human observers found instances of rockfall not detected by the algorithm and vice versa.

Events that were not detected by the algorithm were primarily short rockfall located near the western edge of the failure (the right portion of the image shown in Figure 4-10). Evaluation of these events revealed that the rockfalls in this region demonstrated low visual contrast and had overall movement distances below the minimum distance parameter used during video processing, implying that results could be improved through more careful calibration of the algorithm parameters for the site. These differences account for the shallower rockfall frequency acceleration in algorithm detections versus human detections from mid-day on May 30, 2021, until the time of failure on May 31, 2021. The algorithm also detected events that were not detected by the human observer. Some of these were due to the algorithm's ability to track multiple motions and evaluate the entire camera view in each frame. Notably, there was a sudden increase in detections by the algorithm at mid-day on May 29, 2021, when a planned blast resulted in multiple rockfalls from the explosive force. The human observer recognized the rockfalls as occurring due to human action rather than part of the natural slope failure, so discounted these movements. The algorithm recognized objects falling in a

hazardous manner, so included these events in the count. Both evaluation methods show an exponential increase in rockfall frequency prior to the failure, confirming the results of Shafer et al. (2023) and Wellman et al. (2022).

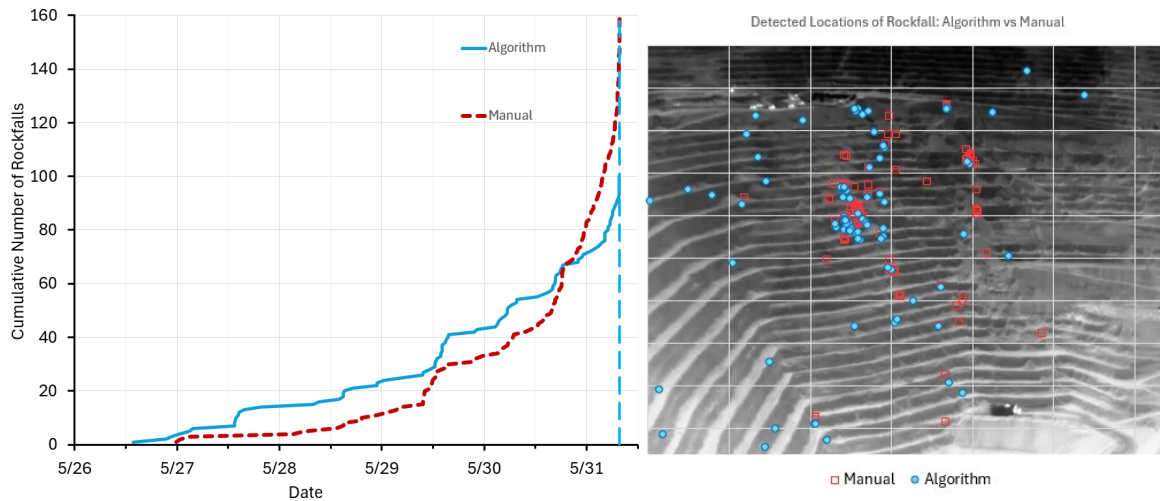


Figure 4-10. Comparison of human-detected and automatically detected rockfall. (left) Cumulative rockfalls logged by human observer (red) versus automated rockfall detection algorithm (blue) leading up to the Leo failure at Bingham Canyon Mine, Utah on May 31, 2021. Modified from Schafer et al. 2023. (right) Locations of rockfall events detected by human observers (red squares) and the automated rockfall detection algorithm (blue circles) over the five days prior to the Leo failure at Bingham Canyon Mine in Utah. Modified from Schafer et al. 2023.

The prototype software establishes the groundwork for development of a commercially viable software system for detecting, tracking, and alarming for rockfall. Further developments will focus on gathering feedback from industry focus groups, incorporating research findings regarding complementary technologies and additional geotechnical applications, and designing a front-end interface for deployment across various operating systems to align with diverse user hardware preferences. The tracking algorithm will undergo continuous updates to enhance software efficiencies and remain aligned with advancements in hardware computing capabilities. The determination of appropriate site-specific algorithm parameters (vectors for motion heuristics and sensitivity thresholds appropriate for separating true movement from background noise) will be improved. Where digital elevation models are available, the expected angle of rockfall will be automatically calculated based on three-dimensional topographic data and each pixel will be georeferenced with a 3D coordinate, resulting in more accurate tracking and alarming of rockfall events. Future work on the algorithm will also include options for discounting detections during times of heavy precipitation or planned blast events to allow isolation of the relation between rockfall and the underlying slope movement. The Unity game engine used in the georeferencing component of the algorithm is capable of significantly higher accuracy than the single location per pixel used in the current 2D to 3D workflow. By comparing brightness levels of multiple pixels at the point of motion, a weighted balance between two pixels could be computed and then used to calculate a ray for locating the true source of motion with sub-pixel accuracy.

Comparison with Machine Learning Techniques. Ongoing research efforts also include attempts to apply machine learning with the expanded data set provided by the algorithm testing to detect rockfall from thermal video data. The results of this study will be compared to the current heuristic-based algorithm in terms of both accuracy and processing requirements. This comparative analysis will be used to identify which approach is most effective for real-time rockfall detection.

5 Rockfall Monitoring System Developments and Upgrades

Two platforms for gathering thermal video data were utilized during Phase 2. The first is the Mobile Monitoring Platform, a trailer with three externally mounted thermal cameras and one bispectral (visual and thermal) pan/tilt/zoom camera, which was built during Phase 1 and continues to be deployed to mine sites during Phase 2 to gather additional video for use in algorithm development, rockfall library expansion, and video quality analysis. This system is useful for extended deployments (gathering data over the course of weeks or months with minimal human interaction). The second platform is a prototype tactical monitoring system with self-contained power, network, and computing resources. This system is meant to be deployable on short notice to provide real-time alarming for personnel working under potentially hazardous slopes.

5.1 Mobile Monitoring Platform

During project Phase 1, a mobile monitoring platform (MMP) was designed and constructed in collaboration with IDS GeoRadar to evaluate the effectiveness of detecting rockfall from thermal video. The MMP was designed to transport the cameras and associated equipment to various mines and project sites, manage thermal video recording and archiving, and monitor camera performance and video output quality. The system includes the mechanical, power, communications, computing, and recording components necessary for deployment and comparative evaluation of up to four thermal cameras. Several upgrades were made as part of project Phase 2, Aim 3 to allow for continued data collection with the MMP. The original hardware components of the MMP and associated upgrades are detailed in Table 5-1. All cameras trialed as part of this project are summarized in Table 5-2.

Table 5-1. MMP Components and Associated Upgrades

Component	Notes	Upgrades Made During Phase 2
Trailer	Manufactured by Aluminum Trailer Company Trailers and modified by IDS GeoRadar	An improved 20,000 lb. trailer coupler was added after the original coupler pin began to warp.
Inverters	2x 250VA Victron inverters	The inverters were upgraded to accommodate power requirements for upgraded equipment.
Battery array	8x deep cycle 12-volt marine batteries (Full River Battery Co) enclosed in Quickbox housings	All batteries were replaced.
Solar panels	6x Q.PEAK DUO-G5 315-330 solar panels – 3x affixed to the MMP roof, 3x ground deployable	N/A
Charge controller	Outback Power Flex Max 80 Charge Controller	The charge controller was replaced due to power issues experienced in Phase 2.
Battery charger	DeltaQ IC 1200W charger	N/A
Cellular connectivity	Sierra Wireless RV50 modem; Proxicast antenna	N/A
Satellite connectivity	Starlink High Performance receiver	This is new equipment added in Phase 2

Component	Notes	Upgrades Made During Phase 2
Ethernet	Wired WAN port to connect to site networks	N/A
Video recording	FLIR Meridian Net Video Recorder (NVR)	Replaced with a ThinkStation P3 Tiny Workstation with a faster CPU and more memory.
Extra video storage	5TB Seagate portable hard drive	A 22Tb external hard drive system was added to provide adequate data storage for longer-term deployments.
Control System	FLEXSQ5 Supervisory Control and Data Acquisition (SCADA)	N/A
Solar Irradiance	IMT Solar irradiance sensor Si-V-10TC	N/A
Temperature	2x thermistors – 1x external, 1x internal	N/A
Rain Gauge	Rainwise Tipping Bucket Rain Gauge 111-PVMet 500	It was observed that the anemometer was interfering with the accuracy of rain gauge measurements. The devices were separated to address this problem.
Anemometer	TheisClima Anemometer	

Table 5-2. Thermal Cameras Deployed on the MMP

Camera Model	Thermal Field of View	Thermal Resolution (native)	Radiometric output ¹	Phase 1	Phase 2
FLIR A400	14° × 10°	320×240	Yes	Yes	No ²
FLIR A700	42° × 32°	640×480	Yes	No	Yes
FLIR FC-632-ID	32° × 26°	640×480	No	Yes	Yes
AXIS Q1941-e	6.2° × 4.6°	384×288 ³	No	Yes	No ⁴
AXIS Q8752-e ⁵	17° × 12.8°	640×480	No	Yes	Yes

5.2 Development of a Prototype Tactical Rockfall Monitoring System

To facilitate deployment and scalability, a prototype tactical monitoring system was developed. The system is a mobile, tactical rockfall detection solution designed for algorithm testing and on-site data collection. The system was manufactured by GroundProbe at their facility in Tucson, Arizona, under the guidance of the GCE, which outlined the necessary system requirements and provided feedback throughout the design process. Among its key capabilities, the system was designed to be transported in a pickup truck or other light vehicle and installed in less than one hour by a single person. Figure 5-1 shows the prototype system deployed at a mine in northern Nevada.

¹ Can provide temperature data for every pixel in the camera's field² Replaced with FLIR A700 scientific thermal camera for Phase 2

² Replaced with FLIR A700 scientific thermal camera for Phase 2

³ Effective recorded resolution: 320×240⁴ Removed from MMP for most of Phase 2 due to problems with high video compression producing too much noise for rockfall identification

⁴ Removed from MMP for most of Phase 2 due to problems with high video compression producing too much noise for rockfall identification

⁵ Includes pan-tilt functionality and a visible-light camera

5.2.1 Technical Specifications

The FLIR FC-632-ID camera serves as the system's imaging component. This is a security-grade thermal camera with a relatively accessible price point (around \$8,000 as of this writing) as well as the ability to output high bitrate (low compression) video. The camera features a 32° horizontal field of view, resolution of 640 × 480 pixels, and a maximum framerate of 30 frames per second. Its uncooled vanadium oxide microbolometer provides consistent performance with less need for maintenance than more expensive cooled thermal detectors. The camera has an operating temperature range of -50 °C to 70°C (-58 °F to 158 °F).



Figure 5-1. Prototype tactical monitoring system deployed with Tripod 2 at a mine in Nevada.

The system was designed such that other thermal cameras can be utilized with an appropriate mount. This flexibility allows for customization based on specific project requirements or advancements in thermal imaging technology. The computing component of the prototype system is

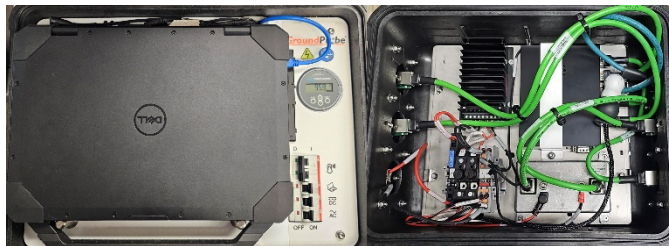


Figure 5-2. The prototype system processing unit (left) and PoE injection system (right).

a Dell Latitude 5424 Rugged Laptop, which was selected for its robust construction and reliability. Equipped with an Intel i7-8650U processor, 16 GB of RAM, and 1TB NVMe Storage, it offers adequate performance for data collection and storage. The laptop is housed in a rugged case along with an additional 256 Wh rechargeable LiPO4 battery which allows for approximately 5 hours of continuous operation in areas

lacking reliable line power. The unit can also accept 120V AC power to facilitate prolonged deployment. Power-over-Ethernet (PoE) connectivity streamlines the integration of imaging and computing components. Figure 5-2 shows the processing, battery, and PoE components of the system.

The prototype system has two tripod options (Figure 5-3):

1. Tripod 1: A heavy-duty fixed-height metal tripod designed for long-term deployments in rugged environments.
2. Tripod 2: A lightweight and adjustable surveyor's tripod that can be easily adjusted to meet the needs and characteristics of a worksite for short-term, tactical deployments.



Figure 5-3. Prototype tactical system tripod options: *(left)* heavy-duty tripod option, shown with prototype system camera, processing unit, and PoE system in an office environment; *(right)* lightweight tripod option, shown with thermal camera (remainder of standalone system not visible), shown during a deployment test.

5.2.2 Design Considerations for Extreme Environments

The prototype system was engineered to withstand the conditions prevalent in mining environments, while ensuring operational efficiency and adaptability. All system components are enclosed with robust weatherproof storage boxes, engineered to endure extreme environmental conditions. These enclosures provide protection against heavy precipitation, snow, temperatures from -30 degrees to 130 degrees Fahrenheit, dust ingress, and wind speeds exceeding 80 miles per hour. The FLIR FC-632-ID camera is rated IP66 and IP67 (dust-tight and capable of withstanding powerful water jets or submersion in 1 meter of water for periods of 30 minutes). The processing unit, battery components, and power system are housed in Pelican cases with all internal components secured in place. Additionally, all connecting cables between the components (not including the alternating current power cable for line charging) feature rugged, weatherproof sheathing, cable glands between cable and connector, and rubber gaskets used as pressure seals for the connectors. The AC power connector from the processing unit case uses a gasketed insert to prevent water and dust intrusion when not in use.

5.2.3 System Installation, Transport, and Portability

Setup of the system's physical and software components can be completed in approximately five minutes when using default settings. However, software setup time varies by the amount of tailoring (e.g., region masking, fall angle definition, etc.) necessary for the site conditions. The prototype

system was designed to be lightweight enough that it could be transported to an observation site and installed by a single person on foot. This can be achieved when deployed with Tripod 2. Deployment with the more rugged Tripod 1 requires transport with a light vehicle. The weight of each system component and of the resulting total system with different tripod configurations are approximated in Table 5-3. Long-distance transport of the unit requires ground shipping using hazardous materials labeling due to the size of the battery, which exceeds FAA guidelines for lithium batteries on domestic flights.

Table 5-3. Approximate Weight of Prototype System Components

Component	Weight (kg)
Processing Unit	17
Power-over-Ethernet System	4
Camera and Case	4
Cables	<1
Tripod 1	20
Tripod 2	7
Total Weight with Tripod 1	45
Total Weight with Tripod 2	33

5.2.4 Issues Encountered

While deployed at a Nevada mine during Testing Phase 1 (Section 3.3.2), the power components of the prototype system experienced an unexplained failure which ended data collection earlier than anticipated. The system was transported to GroundProbe's Tucson facility for troubleshooting, where the issue (a faulty charge controller) was identified and addressed. However, concerns regarding the reliability of the power system persisted due to intermittent outages during subsequent deployments. Future deployments were limited to mines within driving distance of UArizona to allow for more efficient troubleshooting.

5.3 Future Work

The two prototype data acquisition systems provided valuable insights that will inform future system builds. Building upon experience gained in Phase 2, future work will include enhancing the tactical system for tactical monitoring in safety-critical areas when rapid data generation and alarming are needed (e.g., personnel working in high rockfall risk areas). Considerations and anticipated future work needed to meet this goal include:

- Incorporating alternate computing infrastructure options to better meet the demands of simultaneous data processing and storage. Strategies include using more powerful and efficient embedded computing systems, such as NVIDIA's Jetson series of high-performance GPUs.
- Exploring an alternate power system design with increased reliability which meets all applicable requirements for domestic air travel in the US.
- Exploring more compact solutions such as an all-in-one, wheeled and weatherproof casing. The cameras tested with the Version 0 prototype use a PoE interface that required a local ethernet network with a power-injection solution. This prototype currently has separate

cases for the PoE network, computing/battery unit, and camera. The inter-case cabling and tripod must be carried separately from these three cases. While the entire system can be carried by a single person, a more consolidated solution would increase ease of deployment.

6 Rockfall Forecasting based on Empirical Correlations and Statistical Modeling

This section documents efforts to model empirical relationships between the GCE's rockfall and meteorological data sets in furtherance of rockfall event forecasting. The aim of this work is to establish relationships between environmental forces and rockfall events to assist geotechnical engineers in developing weather-related trigger action response plans for rockfall. It is well documented that meteorological cycles and events impact slope stability, affecting both natural and engineered slopes (Robinson et al., 2017; Sidle, 2007; Beale & Read, 2013). However, existing rockfall frequency data sets lack the temporal resolution for assessment at timescales that are relevant to mining operations. Preliminary interpretations of meteorological impacts on rockfalls detected using thermal cameras were made during project Phase 1 (Wellman et al., 2022). The analysis documented here builds on the Phase 1 interpretations by employing statistical methods on rockfall and meteorological data optimized for assessing these relationships. Rockfall data sets were generated using the GCE's rockfall detection algorithm presented in Section 4 on archived thermal video collected during Phase 1 deployments. These data were evaluated with concurrent on-site weather data using logistic regression to quantify the relationship between the various meteorological factors and rockfall initiation.

Previous studies, such as Nissen et al. (2022) and D'Amato et al. (2016), have utilized logistic regression for correlating rockfall observations on natural slopes with meteorological forces. However, the rockfall datasets analyzed in these studies differ significantly from the algorithmically generated data evaluated here. Data analyzed in previous studies include historical rockfall accounts and public records going back 200 years (Nissen et al., 2022), and periodic LiDAR scanning coupled with high-resolution photography collected over several years (D'Amato et al., 2016). The findings of these studies vary, however both D'Amato et al. (2016) and Nissen et al. (2022) concluded that precipitation appears to have a first-order effect on rockfall initiation. D'Amato et al. further concluded that thermal ice dilation during the thawing side of a freeze thaw cycle significantly contributed to rockfall initiation. Complimenting this, a study by Nigrelli et al. (2022) utilized in-situ monitoring to measure rock mass temperature, finding that solar irradiance may have a strong influence on the heating of bare rock surfaces more so than external air temperature, which may further influence instabilities (Nigrelli et al., 2022). Additionally, Macciotta (2019) conducted a meta-analysis of studies and methods for correlating environmental forces with rockfall, concluding that adopting a probabilistic approach to quantifying rockfall may be the next step in predicting a seemingly random natural process.

The relatively low temporal resolution of the data sets used in these previous studies limited the researcher's correlation analyses to the scale of months or years, which is insufficient for the purpose of predicting rockfall based on real-time or forecasted meteorological events. In contrast, the data presented in this study contain continuous time series of rockfall data down to the hour scale, providing a significant advantage for evaluating these correlations at sub-24-hour timescales, which are most relevant to active mining operations.

6.1 Data Collection and Collation

Two mines were investigated in this analysis, a steelmaking coal mine in British Columbia, Canada (Mine 7), and a copper porphyry mine in Arizona (Mine 8). The climates at these sites provided a unique opportunity to evaluate the influence of freeze-thaw cycles, precipitation, and solar irradiance on rockfall. Data collected at Mines 7 and 8 includes thermal video recordings from the

FLIR FC-632-ID and meteorological data from the MMP FlexScada recording unit, as well as near- or on-site weather stations. Meteorological data considered in this analysis includes temperature, precipitation, solar irradiance, and wind. The MMP was deployed at Mine 7 between January 27th and April 13th, 2022. Mine 7 was selected to evaluate the impact of freeze-thaw cycles on rockfall occurrence. The Mine 8 data set was recorded between June 21st and September 13th, 2022. Mine 8 was selected to analyze the impact of extreme heating cycles and heavy rainfall. Summary statistics for meteorological parameters considered are provided for Mine 7 and 8 in Tables 6-1 and 6-2. This information is presented in graph form in Appendix B.4.

Table 6-1. Summary of Mine 7 Meteorological Data

	Temperature (C)	Precipitation (mm)	Wind (M/S)	Solar Irradiance (W/m ²)
Min	-29.87	0.00	0.00	0.18
Max	14.77	16.49	7.92	1045.47
Ave	-6.10	0.99	1.09	118.73
Total	-	76.29	-	-

Table 6-2. Summary of Mine 8 Meteorological Data

	Temp (C)	Precipitation (mm)	Wind (M/S)	Solar Irradiance (W/m ²)
Min	16.54	0.00	0.00	0.00
Max	46.38	29.08	5.40	1441.18
Ave	29.94	0.17	0.49	250.74
Total	-	334.34	-	-

6.1.1 Rockfall Data Collection and Collation

Rockfall data sets were generated from the archived thermal video for both Mine 7 and 8 deployments. The videos were processed using the GCE's rockfall detection algorithm presented in Section 4, resulting in near-continuous records of rockfall detection data when the thermal video feed was not obscured by extreme weather events. Algorithm parameters that dictate the sensitivity of rockfall detection were tailored for each site to minimize false positive detections. Additionally, areas outside of the slope of interest were masked by removing video frame coordinates from the algorithm input to ensure non-rockfall motion (e.g. mining operations) were not captured as false detections. The resulting data set consists of timestamp, pixel location, source filename, and frame number values associated with the initiation of movements classified as rockfall. The algorithm output was converted to a categorical (binary) hour-scale time series in which rockfall versus no rockfall is denoted. Daily rockfall data for Mine 7 and Mine 8 are summarized in Table 6-3 and Figures 6-1 and 6-2, respectively.

Table 6-3. Summary of Daily Rockfall Events by Mine Site

		Maximum	Minimum	Average Daily Rockfall over Deployment
Mine 7	Quantity	1635	9	257
	Date	7-Apr	13-Apr	-
Mine 8	Quantity	300	1	47
	Date	21-Aug	7-Jul	-

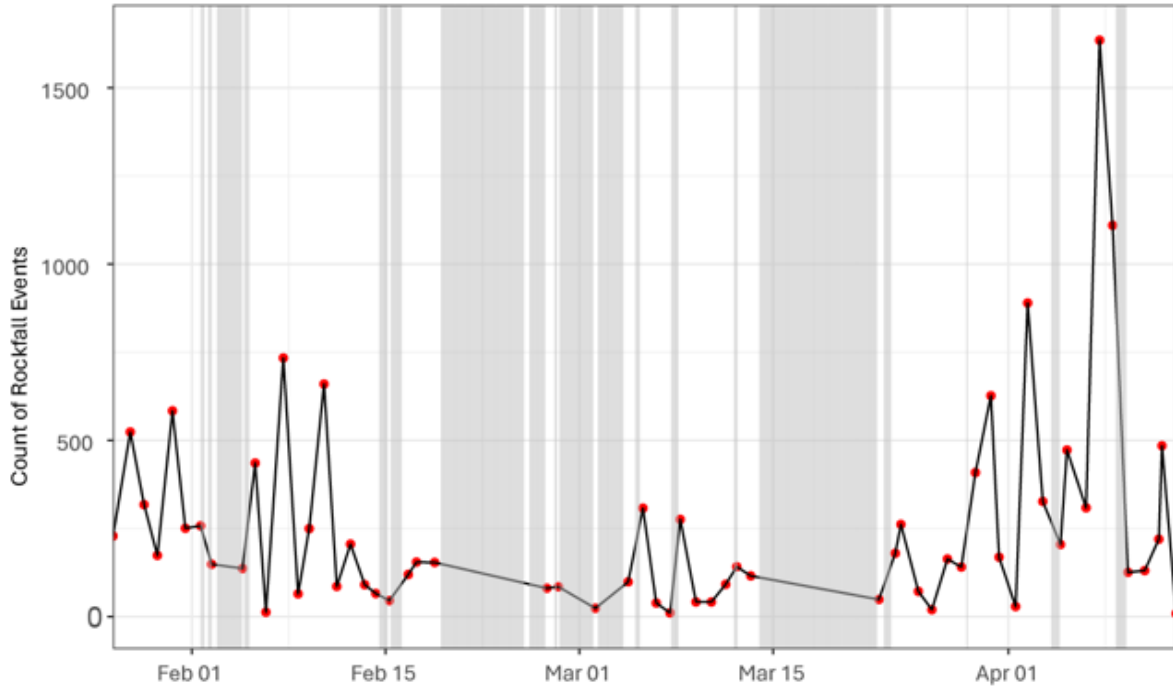


Figure 6-1. Time series representing the daily sum of detected Rockfall Initiations at Mine 7. Periods during which the slope was obscured by extreme weather events are represented by vertical grey bars.

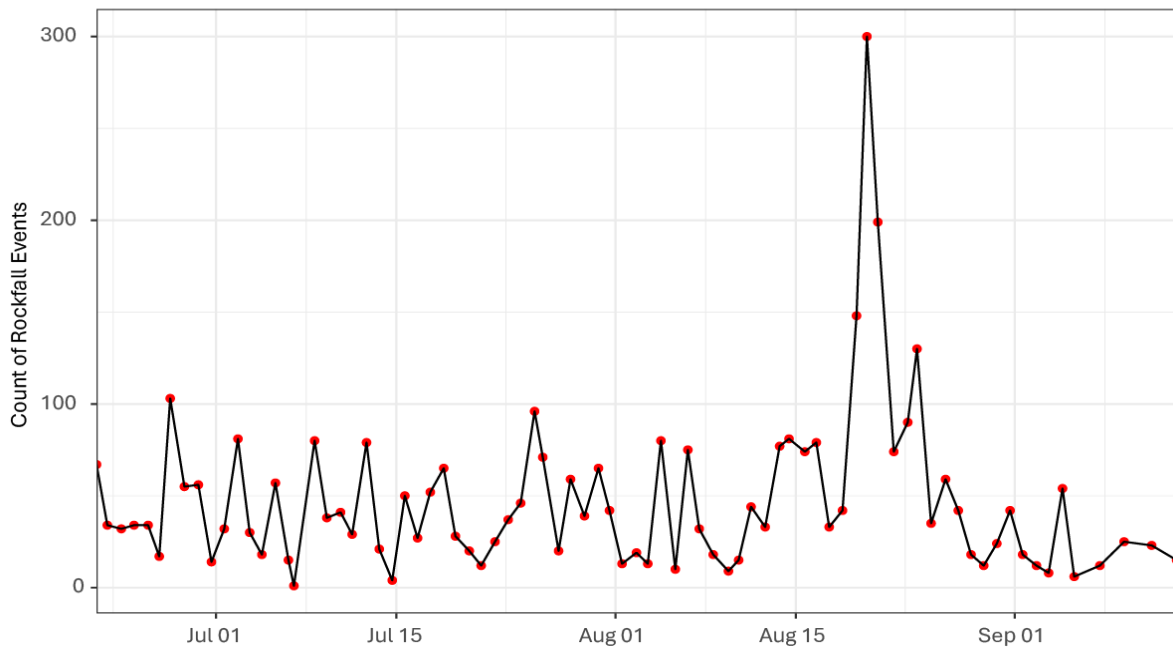


Figure 6-2. Time series representing the daily sum of detected Rockfall Initiations at Mine 8. No periods of slope obscurity occurred during this deployment.

6.1.2 Meteorological Data

Meteorological parameters collected during the Phase 1 deployments to Mines 7 and 8 included solar irradiance (W/m^2), temperature ($^{\circ}\text{C}$), precipitation (mm), and wind speed (m/s). More details about how and why these data sets were incorporated into the analysis are provided in the following subsections.

6.1.2.1 Temperature

Temperature was gathered via a temperature sensor set on the outside of the MMP to gather external temperatures. Temperature was sampled every minute over the course of the deployment and converted to an hour-scale time series representing the average over the hour. Past work by D'Amato suggests that temperature influences rockfall through the expansion and contraction of pore- and fracture-bound water (D'Amato et al., 2016). Additionally, thermal expansion of the overall rock mass has potential for initiating rockfall. As temperature was gathered during deployment, this meteorological parameter was a natural candidate for testing influence on rockfall. To further track the phase change and quantify the freezing of liquid water at Mine 7, freezing potential is calculated.

Freezing potential. Freezing potential can be considered a proxy for potential for ice growth (D'Amato et al., 2016) and is a measure of the temperature relative to the freezing point and the length of time over which temperature was below freezing. Positive freezing occurs when temperatures are below the freezing point and actively dropping, while negative freezing occurs when temperatures are below the freezing point but rising. As rising temperature approaches the freezing point, freezing potential approaches zero until the freezing point is surpassed and freezing halts. This is a cyclical process during each freeze-thaw cycle and has units of temperature*time (Figure 6-3). D'Amato et al. found that decreasing freezing potential was correlated with the cessation of ice growth, which was thought to result in the detachment of rocks previously bound by ice to their surrounding rock mass. Conversely, increasing freezing potential could serve to increase rock stability by stimulating ice growth, creating cohesive ice bonds between rocks. Equation 1 provides the integration needed to perform this calculation, where t_0 is time when temperatures dropped below freezing and t is the time of calculation. T_f is the temperature at which water freezes while $T(t)$ represents the temperature at the time of calculation. Freezing potential was only calculated for Mine 7 as Mine 8 did not experience freeze-thaw cycles.

Equation 1: Freezing Potential

$$FP = \int_{t_0}^t (T_f - T(t)) dt, T(t) < 0$$

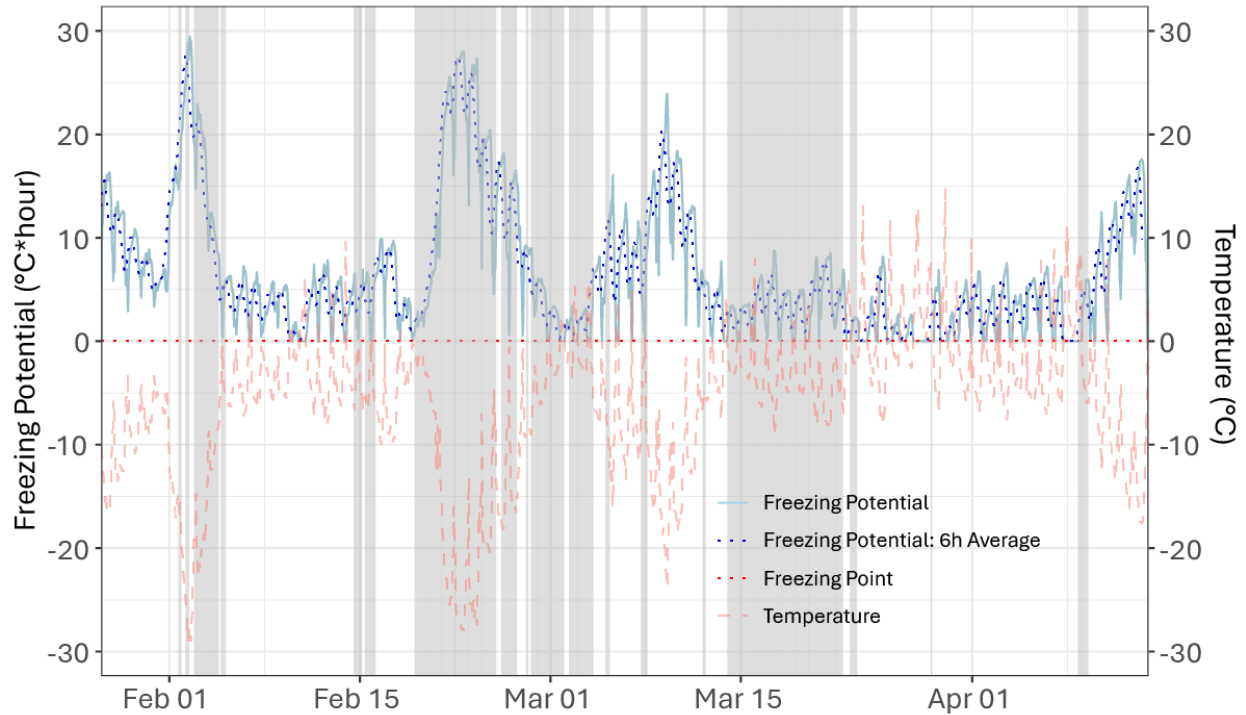


Figure 6-3. Timeseries showing freezing potential during Mine 7 deployment. Grey bars represent time periods for which the slope was obscured by heavy fog, rain, or snow.

6.1.2.2 Precipitation

Precipitation was sampled on five-minute intervals and then converted to an hour-scale time series representing the total precipitation recorded during each hour. To quantify the degree to which the rock mass is inundated with water or ice, the data was further delineated into two additional parameters: 24-hour precipitation and precipitation intensity.

24-hour Precipitation. The 24-hour precipitation represents the rolling sum of the total per-hour precipitation for the previous 24-hours.

Precipitation Intensity. Precipitation intensity is the average amount of precipitation per hour for a given storm or precipitation event. To calculate precipitation intensity, an appropriate Inter-Event Time Definition (IETD) must first be determined. IETD defines the minimum amount of time that must pass between precipitation events for a new event to be considered separate from previous events. Restrepo-Posada & Eagleson (1982) found that the inter-event periods for a given dataset will form an exponential distribution when filtered by an appropriate IETD. In other words, when the inter-event time periods are filtered such that they meet or exceed the IETD, the coefficient of variation (CV) of the inter-event time periods dataset will equal one (the mean of the data set will equal the standard deviation). This means that all rainfall between these inter-event periods are considered one precipitation event or storm. To determine the appropriate IETD for the Mine 7 and Mine 8 precipitation datasets, IETD values between one- and 24-hours were plotted against their associated coefficients of variation. Figures 6-4 and 6-5 show that the appropriate IETDs (where $CV=1$) for Mines 7 and 8 were determined to be 5.9 hours and 1.7 hours, respectively.

Using these IETDs, the precipitation dataset can be grouped into distinct events. The precipitation events identified for the Mine 7 and 8 datasets are presented in Figures 6-6 and 6-7 and in Appendix

B.1. Mine 7 experienced 30 distinct precipitation events while Mine 8 experienced 20. On average the precipitation events at Mine 8 were more than seven times as intense as the precipitation events at Mine 7. This is to be expected as precipitation at Mine 8 was recorded in Arizona during monsoon season, which is known for heavy precipitation over short periods. Additionally, Mine 7 precipitation includes both frozen and liquid precipitation, while Mine 8 includes only liquid precipitation, due to temperatures fluctuating around the freezing point at Mine 7, and temperatures staying above freezing at Mine 8.

6.1.2.3 Solar Irradiance

Solar irradiance was sampled every minute over the course of the deployment and converted to an hour-scale time series representing the average over the hour. Solar irradiance is the electromagnetic radiation emitted by the sun, measured over the area of exposure. As suggested by Nigrelli et al. (2022), solar irradiation can heat the surface of the rock mass to temperatures well above the static air temperature. This difference in temperature shows that solar irradiance is a strong driver of rock mass thermal heating outside of external temperature and may serve as a metric for thermal rock mass expansion, leading to rockfall.

6.1.2.4 Wind

Wind speed was sampled every minute over the course of the deployment via the MMP's onboard anemometer and converted to an hour-scale time series representing the average wind speed per hour. While no predetermined conclusions about wind causing rockfall are presented in this analysis, wind was included to test the possibility of an empirical relation with rockfall initiation.

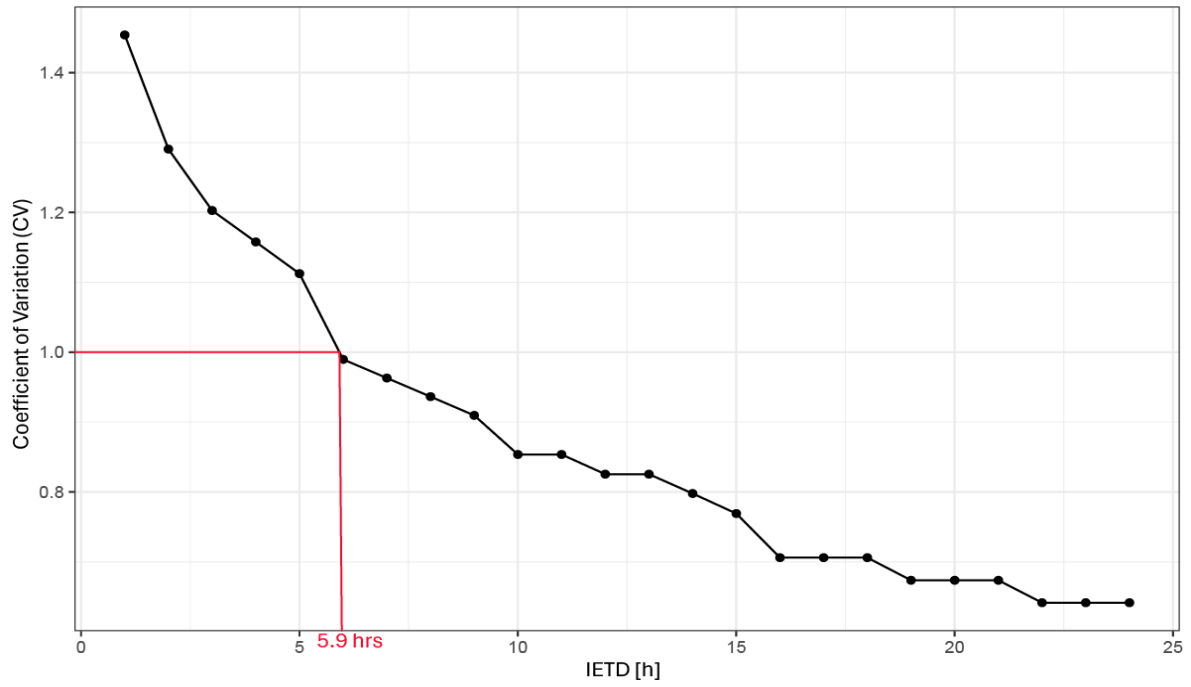


Figure 6-4. Coefficient of Variation vs Inter-Event Time Definition – Mine 7

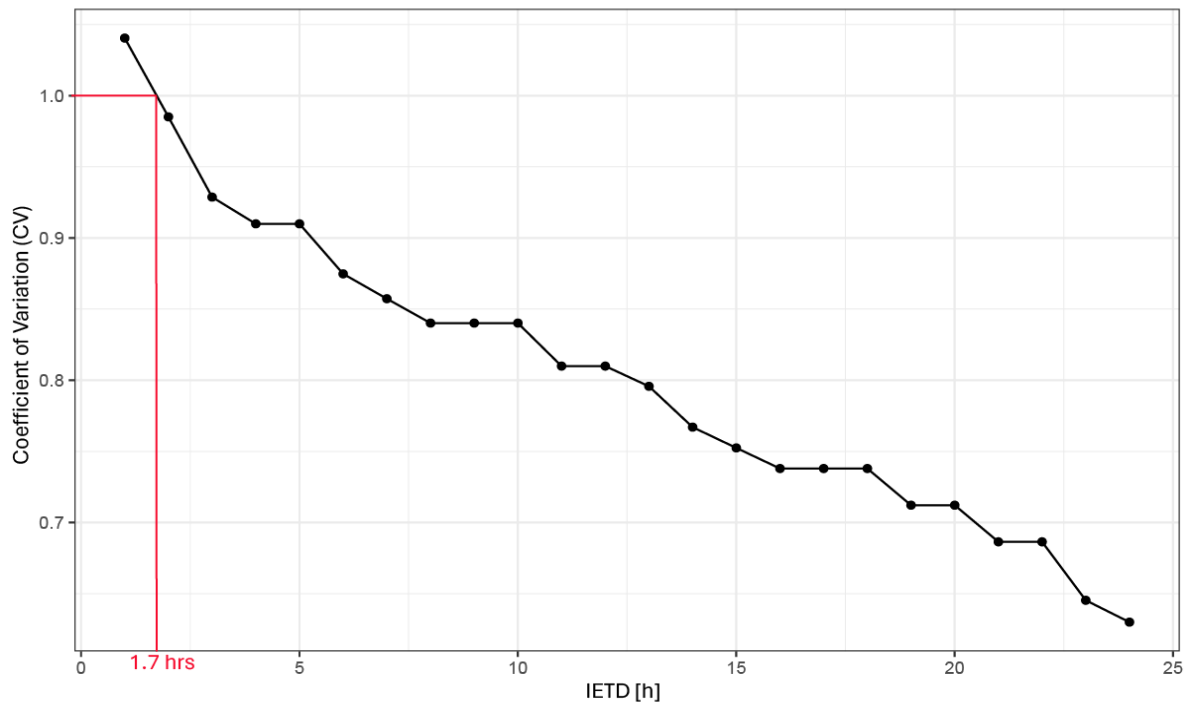


Figure 6-5. Coefficient of Variation vs Inter-Event Time Definition – Mine 8

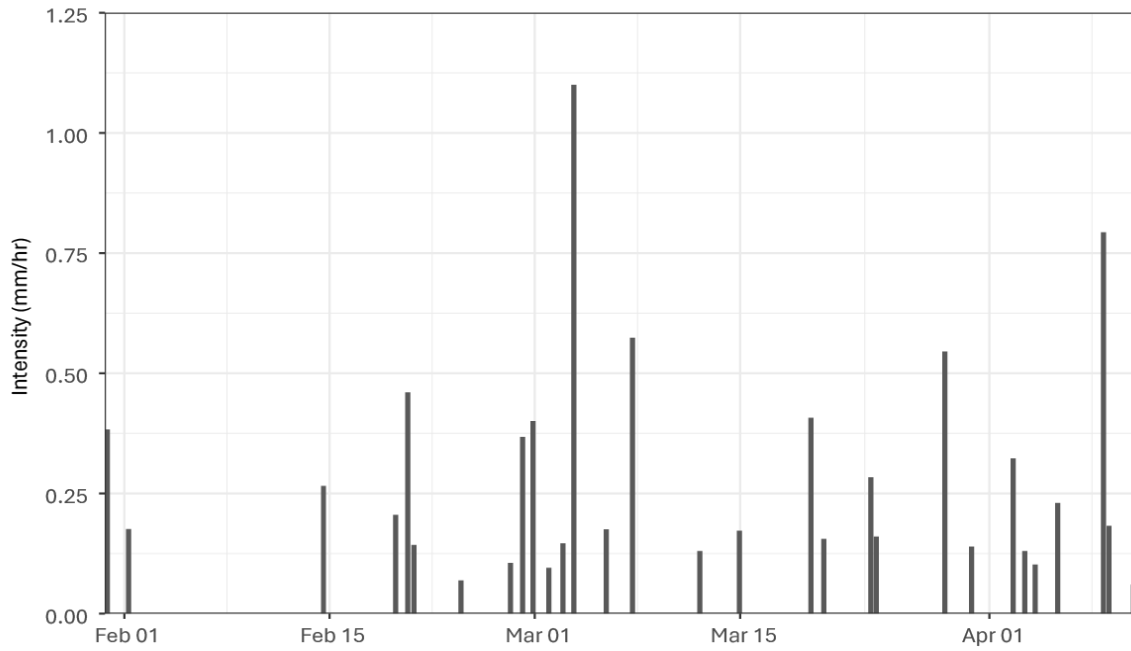


Figure 6-6. Precipitation intensity for all precipitation events observed during Mine 7 deployment.

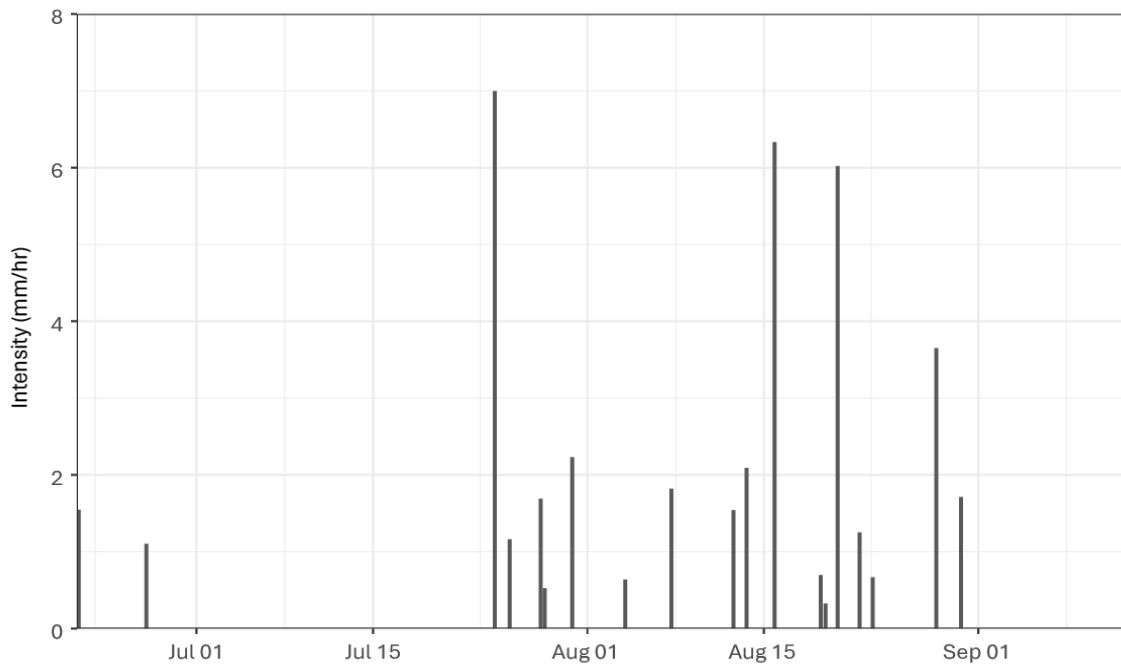


Figure 6-7. Precipitation intensity for all precipitation events observed during Mine 8 deployment.

6.2 Data Analysis

This section presents a detailed exploration of the relationship between rockfall events and meteorological factors. It begins by outlining the steps to validate the data, followed by a detailed discussion of the analytical and modeling techniques employed. The analysis incorporates Weight of Evidence (WoE) and Information Value (IV) to quantify the predictive strength of individual meteorological factors, providing an initial understanding of how specific meteorological conditions correlate with the likelihood of rockfall. Building on these findings, logistic regression modeling was used to create a more comprehensive predictive framework that accounts for the combined effects of multiple meteorological factors. The resulting model aims to capture the relationship between meteorological factors and rockfall events, offering a probabilistic approach to estimate rockfall risk under varying conditions.

6.2.1 Data Validation

During initial review of the Mine 7 thermal recordings, several intervals in which the slope under investigation was obscured due to meteorological events (e.g., heavy snow, precipitation, fog) were observed. Although thermal cameras generally perform better than visible light cameras in adverse weather conditions, the distance between the camera and the slope – approximately 7,500 feet – compounded the effects of the weather, at times fully obscuring the view of the slope. These obscured periods accounted for approximately 37% of the total observation period and were removed from both the rockfall and meteorological datasets prior to analysis.

In the initial review of the Mine 8 data, several instances were identified where frequency of detections was unreasonably high, and unlikely to be attributed to actual rockfall events. It was determined that the user-defined algorithm parameters for Mine 8 were overly sensitive, causing a large number of closely clustered false positives primarily triggered by cloud movement or airborne dust. To address this issue, a filter was applied to limit the detection frequency to one-per-minute. This adjustment effectively eliminated the majority of false positives while still preserving true positive results. In future applications, more site-specific tailoring of the algorithm parameters will help avoid this issue by better accounting for local environmental conditions.

6.2.2 Exploratory Data Analysis

Weight of Evidence (WoE) and Information Value (IV) were used to assess the predictive strength of the binned meteorological data and to quantify the overall importance of each meteorological variable in predicting rockfall initiation. These tools, commonly used in the financial and banking industry for credit scoring and risk modeling, have previously been applied by Nissen et al. (2022) to quantify the impact of meteorological data on rockfall initiation. WoE provides a means of converting continuous variables (e.g., temperature) into categorical variables. The first step in this transformation is binning of the continuous variable. Binning can be defined in several ways, including equal-width and equal-frequency binning. For this analysis, all meteorological parameters were broken into 20% bins representing five intervals of equal width across the range of the data set. WoE compares the distribution of events (instances where rockfall was observed) to non-events (instances where no rockfall initiation was observed) across different categories of a predictor variable (e.g., temperature), as defined in Equation 2 (Siddiqi, 2006, p. 81).

Equation 2: Weight-of-Evidence (WOE)

$$WoE = \ln \left(\frac{\text{percent of events}}{\text{percent of non-events}} \right)$$

Table 6-4 presents the bins defined for the temperature data set and associated distribution of rockfall events as an example.

Table 6-4. Example Bins for Temperature Data Set Collected at Mine 8 (n=2,017)

Bin ID	Bin Extents (°C)	Bin Count	% of Total	Non-Event count (Data without Observed Rockfall)	Event Count (Data with Observed Rockfall)
1	[16.54, 22.49)	239	11.8%	96	143
2	[22.49, 28.44)	693	34.4%	433	260
3	[28.44, 34.39)	520	25.8%	333	187
4	[34.39, 40.34)	437	21.7%	193	244
5	[40.34, 46.29)	128	6.3%	46	82
SUM		2017	100%	1101	916

For example, bin two in Table 6-4 contains 693 data points, or hours in which the average temperature fell between 22.49 and 28.44°C, out of 2,017 total data points. Of these data points, 260 are considered “Events”, or hours during which rockfall was observed, and 433 are considered “Non-Events”, or hours during which no rockfall was observed. The WoE value for this bin can be calculated by taking the natural log of 0.28 (percent of data points classified as Events out of all Events (n = 916) across all bins of temperature) over 0.39 (percent of data points classified as Non-Events (n = 1101) across all bins of temperature).

Information Value (IV) aggregates the WoE values to quantify the overall predictive power of a variable (Nissen et al., 2022). It helps assess how well a predictor can distinguish between events and non-events or, in the context of this analysis, which meteorological factors are most influential in predicting rockfalls. The IV is calculated by summing the contributions of the WoE across all categories of the variable, weighted by the difference in proportions of events and non-events (Equation 3).

Equation 3: Information Value (IV)

$$IV = \sum_{b=1}^{nbins} (\text{percent of events}_b - \text{percent of non-events}_b) \times WOE$$

Table 6-5 provides a summary of IV thresholds and interpretations as outlined by Siddiqi (2006). These values are used to assess the predictive power of individual variables in relation to the binary outcome being modeled. The WoE values represent an empirical correlation between the binned parameters that coincide with the most rockfall events and the IV values aim to quantify the strength of that correlation. An example of this process is provided in Table 6-6, which presents the inputs and resulting WoE and IV values for temperature at Mine 8. Figures 6-8 and 6-9 show the distribution of temperature data and the event empirical probability for the same example. Distributions and event empirical probability graphs for all meteorological parameters at Mines 7 and 8 are provided in Appendix B.2. Information Values for all meteorological parameters considered in this analysis are presented in Table 6-7.

Table 6-5. Information Value (IV) Thresholds and Corresponding Interpretations (Siddiqi, 2006, p. 81)

Information Value	Variable Predictiveness
< 0.02	Not useful for prediction
0.02 - 0.1	Weak predictor
0.1 - 0.3	Medium predictor
0.3 - 0.5	Strong predictor
> 0.5	Very strong predictor (rare in practice, may indicate overfitting)

Table 6-6. Weight of Evidence (WoE) and Information Value (IV) Calculation Results for Temperature at Mine 8.

Bin (°C)	Total Count	% of Total	Non-Event Count	Event Count	Event Empirical Probability ¹	WoE	Bin IV	Parameter IV
[16.54, 22.49)	239	11.8%	96	143	59.8%	5.82E-01	4.01E-02	1.89E-01
[22.49, 28.44)	693	34.4%	433	260	37.5%	-3.26E-01	3.57E-02	
[28.44, 34.39)	520	25.8%	333	187	36.0%	-3.93E-01	3.86E-02	
[34.39, 40.34)	437	21.7%	193	244	55.8%	4.18E-01	3.81E-02	
[40.34, 46.29)	128	6.3%	46	82	64.1%	7.62E-01	3.64E-02	

1: Event empirical probability refers to the proportion of observed Events. It is calculated as the ratio of the number of events to the total number of observations and reflects the observed likelihood of the event happening, based purely on historical data. In the context of this analysis, it represents the probability of a rockfall occurring based on the frequency of rockfall events in the dataset, without the influence of any predictive model.

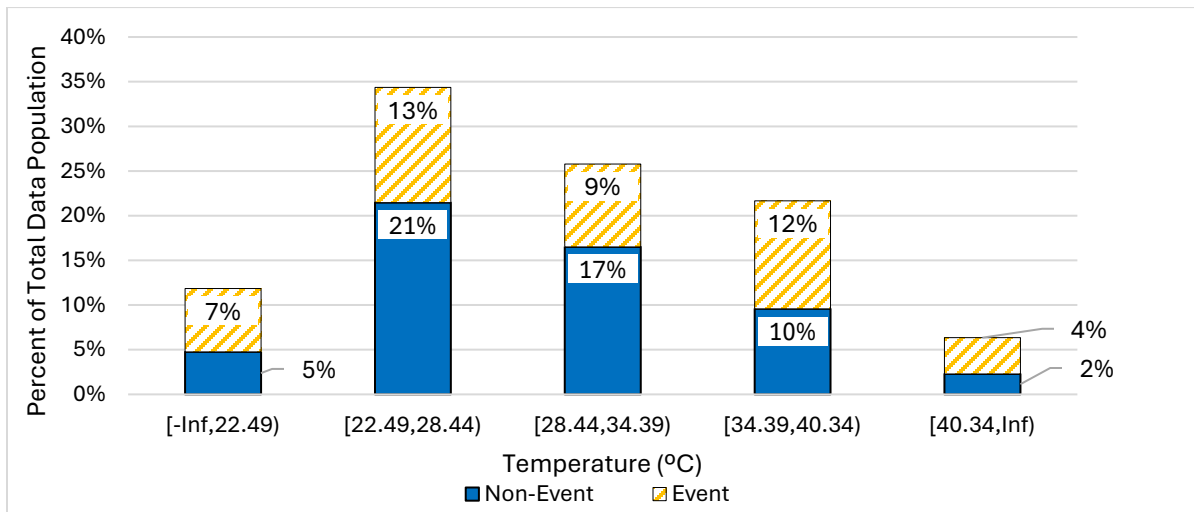


Figure 6-8: Example showing the distribution of Temperature data at Mine 8 (IV=0.189) across the defined bins, as well as the distribution of Non-Event and Event data within each bin. Temperature data points that do not correspond with a rockfall initiation are classified as Non-Events. Temperature data points that do correspond with a rockfall initiation are classified as Events.

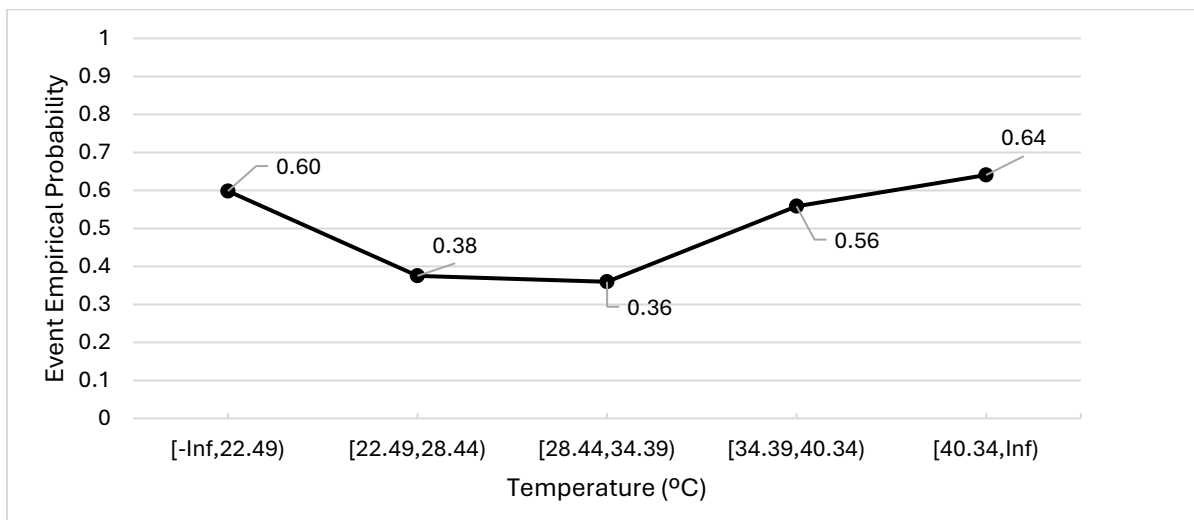


Figure 6-9: Event Empirical Probability for each bin of Temperature at Mine 8 (IV=0.189)

Table 6-7. Information Values (IV) for Evaluated Parameters at Mine 7 and Mine 8

Parameter	Mine 7 IV	Mine 8 IV
Temperature (°C)	0.028*	0.189**
Precipitation (mm)	0.015	0.052*
24hr Precipitation (mm)	0.064*	0.028*
Wind (m/s)	0.009	0.004
Solar Irradiance (W/m ²)	0.049*	0.092*
Precipitation Intensity (mm/hr)	0.013	0.047*
Freezing Potential (°C*hour)	0.085*	-

*denotes $IV \geq 0.02$; **denotes $IV \geq 0.10$

These results indicate that temperature, precipitation, and solar irradiance may serve as weak to moderate predictors of rockfall events. However, these correlations could be coincidental, necessitating further analysis. To determine the statistical significance of each parameter, a logistic regression model was applied as described in the following subsection.

6.2.3 Logistic Regression Modeling

Logistic regression is machine learning model commonly used to determine the predictive power of independent variables (e.g., meteorological parameters) on a binary outcome (e.g., rockfall or no rockfall). In the context of this study, logistic regression was used to quantify the relationship between meteorological parameters and rockfall occurrence. Logistic regression calculates the probability of the event by applying a sigmoid function to a linear combination of the predictor variables, as shown in the example provided in Figure 6-10. The upper half of the function represents one outcome (e.g., rockfall), and the lower half represents the other (e.g., no rockfall). Where $y=0.5$, there is equal likelihood of an outcome occurring or not occurring. As x increases, the probability of the outcome occurring increases.

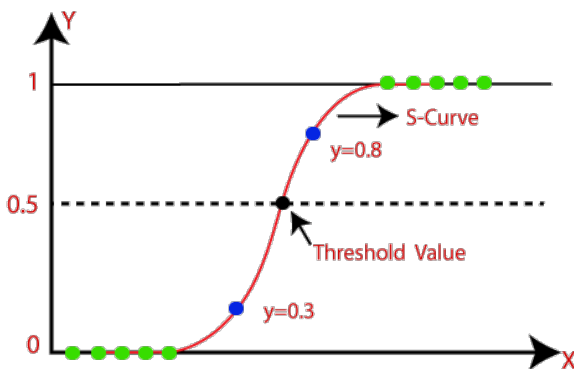


Figure 6-10: Example sigmoid curve representing a fitted logistic regression model. (Logistic Regression, n.d.). In the example, $y = 0.8$ indicates that there is an 80% probability of rockfall occurring, whereas $y = 0.3$ indicates a 30% probability of rockfall.

Typical outputs of logistic regression include:

1. **Predicted values** for each observation in the dataset. These values represent the model's estimated output (rockfall or no rockfall) based on each unique combination of predictor variables. This can be used to evaluate model performance in relation to the actual or observed data set.

2. **Coefficients** for each predictor variable. These provide a measure of the strength and direction of the relationship between the predictor and the probability of the outcome.
3. **Odds ratios (OR)** are calculated by applying the exponential function to each coefficient. They represent the degree to which the odds of the outcome change with each one-unit increase in the predictor variable. For example, an OR for temperature that is greater than 1.0 would indicate that as temperature increases, so do the odds of a rockfall. In contrast, an OR is less than 1.0 indicates that as temperature increases, the odds of a rockfall decrease.
4. **Confidence intervals**, which provide an estimate of the range of OR values estimated at 95% confidence.
5. **P-values** for each coefficient, which provide a measure of whether a predictor variable is statistically significant.

For this analysis, logistic regression was initially conducted using the raw, continuous data set for each of the meteorological parameters with information values indicating weak to moderate predictive power ($IV > 0.02$). These parameters include temperature, 24-hour precipitation, solar irradiance, and freezing potential for Mine 7 and temperature, precipitation, 24-hour precipitation, solar irradiance, and precipitation intensity for Mine 8. Appendix B provides the coefficients, odds ratios, p-values, and confidence intervals for each parameter for all model runs. Figure 6-11 presents Receiver Operating Characteristic (ROC) curves for Mines 7 and 8, respectively. ROC curves provide a metric for model performance by plotting the relationship between False Positive Rate (how often the model incorrectly predicts a rockfall) and True Positive Rate (how often the model correctly predicts a rockfall). An ROC curve for a perfect model would rise sharply to where $TPR=1$ and $FPR=0$. A totally random model would plot as a diagonal line from the origin to the top right of the graph. A model that plots along this line would perform no better than a model based on results determined by flipping a coin. The area under the curve (AUC) is therefore representative of model performance, with higher AUC values indicating a more effective model and AUC values close to 0.5 suggesting no predictive power. The results for Mine 7 show a low AUC of 0.56, indicating that the model is only slightly better than random guessing ($AUC=0.5$). The model for Mine 8 performed slightly better, with an AUC of 0.66, suggesting some discriminatory power.

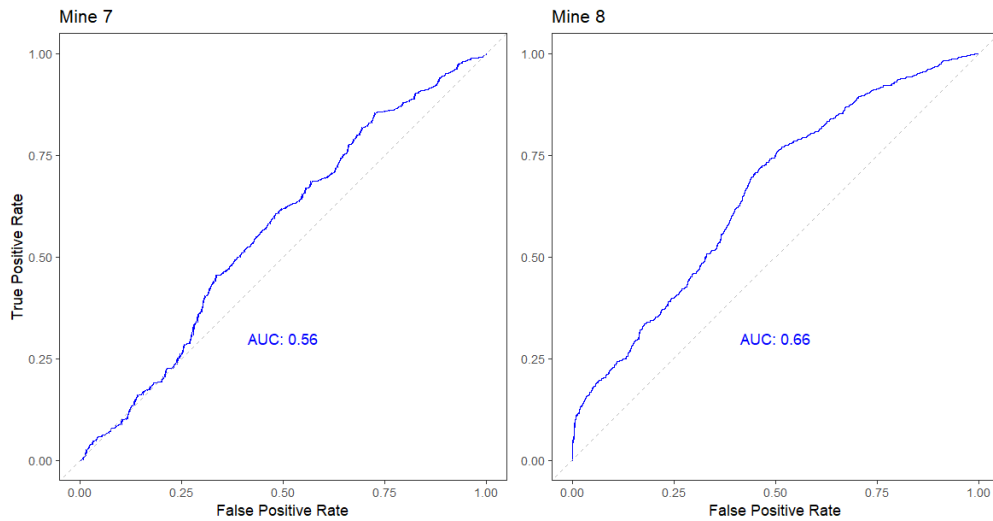


Figure 6-11: Receiver Operating Characteristics of the continuous meteorological data at each mine with no binning or trend scheme applied.

Model Refinement: Binning

To better capture nonlinear relationships between meteorological factors and rockfall risk, the raw meteorological data set was divided into 20% bins, similar to the WoE analysis performed in the previous section. This allowed for evaluation of how rockfall risk changes across distinct ranges. Figure 6-12 presents the results of logistic regression modeling using the binned parameter data for Mines 7 and 8. For Mine 7, the AUC increased slightly from 0.56 to 0.59, indicating a slight improvement in the model’s ability to predict rockfall. For Mine 8, however, the AUC remained relatively constant, with a slight decrease from 0.66 to 0.65. Both results suggest that binning alone does not significantly enhance model performance.

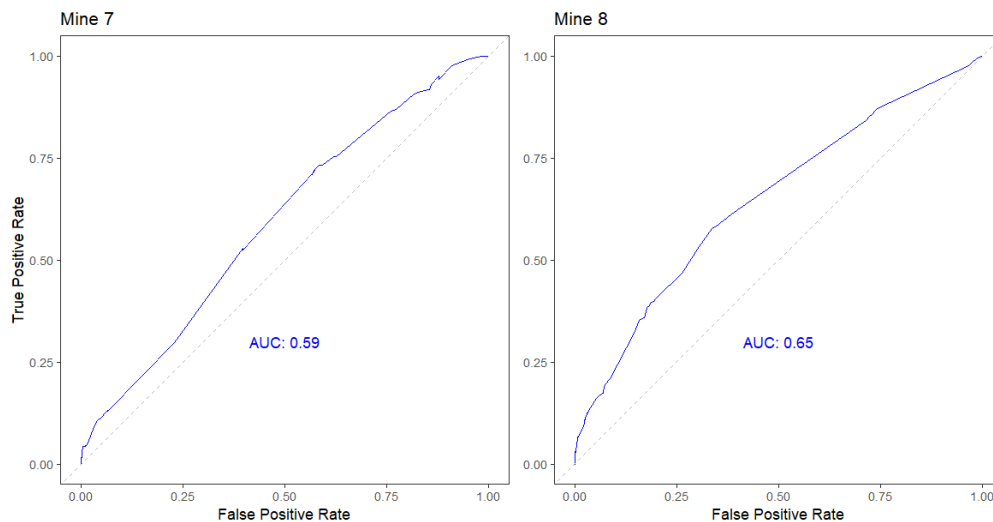


Figure 6-12: Receiver Operating Characteristics of the meteorological data at each mine with binned parameters, but no trend categorization.

Model Refinement: Trend Categorization

The data was further divided into three trend directions: increasing, decreasing or static. This categorization was done to account for how varying trends, such as changes in temperature, may differently impact rockfall risk compared to stable temperatures. Figure 6-13 presents the ROC curves for the trend-based analysis for Mines 7 and 8. This resulted in an AUC of 0.58 for Mine 7 and AUC of 0.70 for Mine 8, showing relatively static performance for Mine 7 and slightly improved performance for Mine 8.

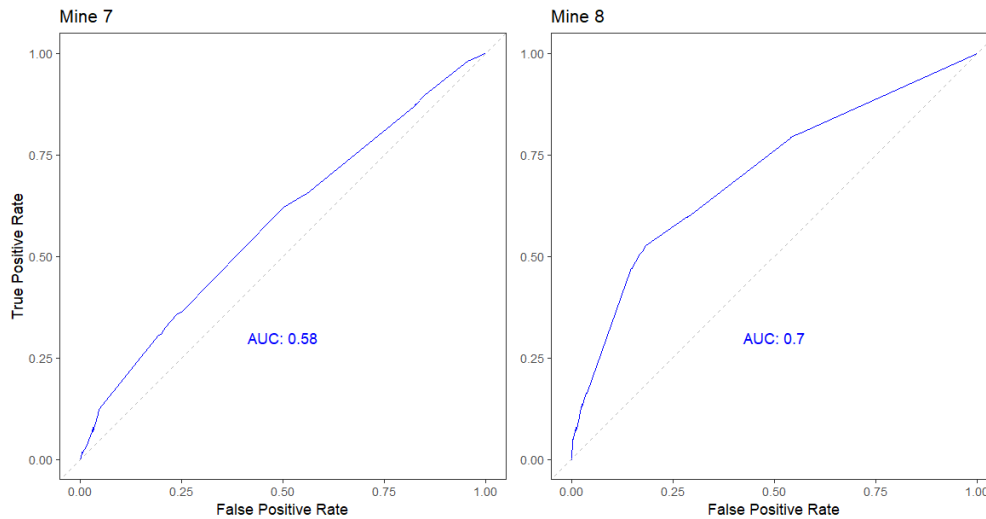


Figure 6-13: Receiver Operating Characteristics of the meteorological data at each mine with trend categorization, but no binned parameters.

Model Refinement: Combining Binning and Trend Categorization

Finally, the binning and trend categorization methods were combined to capture both the magnitude and directional trends in the data. Figure 6-14 shows the ROC curves for this combined analysis. The AUC value for Mine 7 improved to 0.66 and the AUC for Mine 8 increased to 0.77, indicating a substantial improvement in both models' ability to distinguish between rockfall and no rockfall. This suggests that combining both binning and trend categorization provides a more accurate model for predicting rockfall risk based on meteorological conditions.

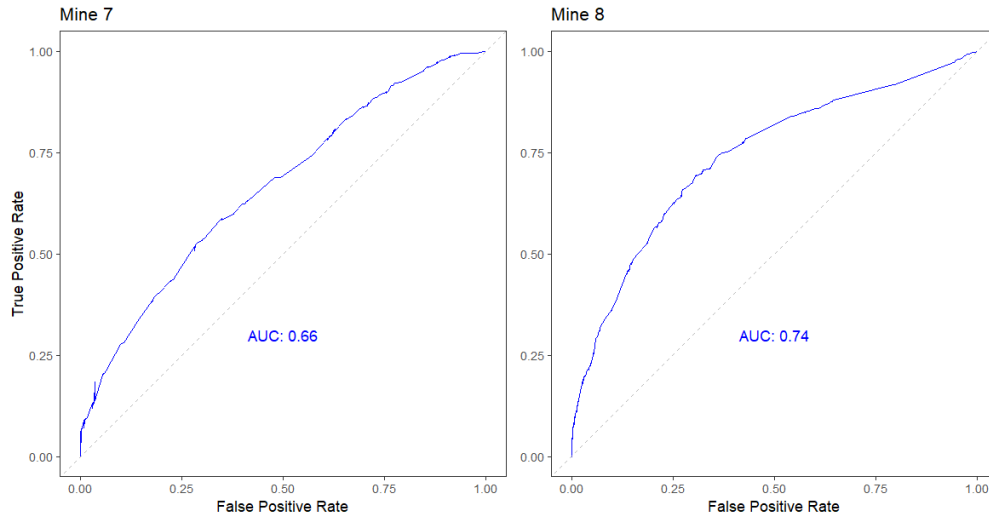


Figure 6-14: Receiver Operating Characteristics of the meteorological data at each mine with binned parameters and trend categorization.

6.3 Discussion

Table 6-8 provides a summary of the parameter inputs and resulting Receiver Operator Characteristic AUC values. The results show that models generated without any segmentation (e.g., binning, trend categorization) of the meteorological data have limited predictive power. This is believed to be due to the unsegmented meteorological data not adequately capturing potentially non-linear relationships between the input parameters and rockfall risk. Subsequent model runs incorporate segmentation of the parameters into 20% bins, categorization by trend, and a combination of approaches. Binning and trend categorization alone do not significantly enhance model performance, however, there is a marked improvement in predictive power when these approaches are combined. P-values for the final model results are provided by model input in Table 6-9. Odds ratios for the final model results are presented in Table 6-10. Coefficients, odds ratios, p-values, and confidence intervals are provided for all other model runs in Appendix B.7.

Table 6-8. Summary of Model Iterations and Associated Receiver Operator Characteristic AUC Values

Model Inputs	Mine 7		Mine 8	
	# of Input Parameters ¹	Area under ROC Curve ²	# of Input Parameters	Area under ROC Curve
Continuous meteorological data - no binning or trend categorization	4	0.56	5	0.66
Meteorological data – binned, no trend categorization	20	0.59	25	0.65
Meteorological data - categorized by trend, no binning	12	0.58	15	0.70
Meteorological data - binned and categorized by trend	60	0.66	75	0.77

1: Total number of parameters after binning and trend categorization
 2: Area under the curve (AUC) from the Receiver Operator Characteristic plots

The model inputs with p-values less than 0.05 (confidence level of 95%) are considered statistically significant. This means the parameter may have a meaningful effect on rockfall initiation, rather than

Table 6-9: Calculated P-Values of parameters fit to logistic regression model for Mine 7 (left) and Mine 8 (right).

Parameter	Mine 7					Mine 8				
	Interval		P-Values ^{1,2}			Interval		P-Values ^{1,2}		
	Min	Max	+	-	o	Min	Max	+	-	o
Freezing Potential (°C*hour)	0.00	5.89	0.151	--	0.070	Parameter Not Tested				
	5.89	11.78	0.232	0.260	--					
	11.78	17.68	0.438	0.940	--					
	17.68	23.57	0.220	0.965	--					
	23.57	29.46	--	0.837	--					
Temperature (°C)	-29.45	-20.61	0.910	--	--	16.54	22.49	0.006**	--	--
	-20.61	-11.76	0.833	0.420	--	22.49	28.44	--	--	0.936
	-11.76	-2.92	0.17	--	0.820	28.44	34.39	0.259	--	--
	-2.92	5.93	0.325	0.680	--	34.39	40.34	--	--	--
	5.93	14.77	--	--	0.678	40.34	46.83	--	--	0.994
Rolling Sum of Precipitation Past 24 Hours (mm)	0.00	1.89	0.063	--	0.004*	0.00	8.59	0.113	--	--
	1.89	3.78	0.013*	0.493	0.861	8.59	17.17	0.708	0.474	0.148
	3.78	5.68	0.431	--	0.518	17.17	25.76	0.147	0.013*	---
	5.68	7.57	0.001***	--	0.053	25.76	34.34	0.989	0.993	--
	7.57	9.46	0.732	0.001***	--	34.34	42.93	0.989	0.591	0.206
Solar Irradiance (W/m2)	0.18	209.06	0.001***	--	0.991	0.00	288.24	0.001***	--	0.910
	209.06	418.12	0.671	0.112	--	288.24	576.47	0.001***	0.003**	--
	418.12	627.18	0.109	0.032*	--	576.47	864.71	0.004**	0.250	--
	627.18	836.23	0.345	0.793	--	864.71	1152.95	--	--	--
	836.23	1045.47	0.857	--	--	1152.95	1441.18	--	--	--
Precipitation Intensity (mm/hr)	Not Modeled (IV < 0.02)					0.00	3.55	0.280	--	0.485
						3.55	7.11	0.985	--	--
						7.11	10.66	0.999	--	--
						10.66	14.21	--	--	--
						14.21	17.77	0.991	--	0.999
Precipitation (mm)	Not Modeled (IV < 0.02)					0.00	5.82	0.273	--	0.269
						5.82	11.63	--	--	--
						11.63	17.45	--	--	--
						17.45	23.26	--	--	--
						23.26	29.08	--	--	--

1: * p < .05, ** p < 0.01, *** p < 0.001; 2: (+)=increasing, (-)=decreasing, (o)=static

Table 6-10: Odds ratios for parameters fit to logistic regression model for Mine 7 (left) and Mine 8 (right).

Parameter	Mine 7					Mine 8				
	Interval		Odds Ratios ¹			Interval		Odds Ratios ¹		
	Min	Max	+	-	o	Min	Max	+	-	o
Freezing Potential (°C*hour)	0.00	5.89	1.966	--	1.855	Parameter Not Tested				
	5.89	11.78	1.876	0.728	--					
	11.78	17.68	3.026	1.124	--					
	17.68	23.57	4.397	0.926	--					
	23.57	29.46	--	1.617	--					
Temperature (°C)	-29.45	-20.61	1.285	--	--	16.54	22.49	3.151	--	--
	-20.61	-11.76	1.39518	0.344	--	22.49	28.44	--	--	0.674
	-11.76	-2.92	2.081458	--	1.371	28.44	34.39	2.450	--	--
	-2.92	5.93	1.599586	1.123	--	34.39	40.34	--	--	--
	5.93	14.77	--	--	1.265	40.34	46.83	--	--	1.069
Rolling Sum of Precipitation Past 24 Hours (mm)	0.00	1.89	0.364	--	0.272	0.00	8.59	2.282	--	--
	1.89	3.78	0.224	0.435	0.895	8.59	17.17	1.069	0.406	0.890
	3.78	5.68	0.471	--	2.069	17.17	25.76	0.731	0.395	--
	5.68	7.57	0.034	--	0.219	25.76	34.34	1.146	0.667	--
	7.57	9.46	0.663	0.037	--	34.34	42.93	1.108	0.879	1.262
Solar Irradiance (W/m2)	0.18	209.06	1.739	--	0.000	0.00	288.24	0.394	--	0.499
	209.06	418.12	0.866	0.587	--	288.24	576.47	1.270	1.884	--
	418.12	627.18	0.596	0.415	--	576.47	864.71	0.332	0.112	--
	627.18	836.23	0.680	1.209	--	864.71	1152.95	--	--	--
	836.23	1045.47	0.889	--	--	1152.95	1441.18	--	--	--
Precipitation Intensity (mm/hr)	Not Modeled (IV < 0.02)					0.00	3.55	2.360	--	0.982
						3.55	7.11	3.752	--	--
						7.11	10.66	2.238	--	--
						10.66	14.21	--	--	--
						14.21	17.77	3.146	--	--
Precipitation (mm)	Not Modeled (IV < 0.02)					0.00	5.82	1.794	--	0.510
						5.82	11.63	--	--	--
						11.63	17.45	--	--	--
						17.45	23.26	--	--	--
						23.26	29.08	--	--	--

1: (+)=increasing, (-)=decreasing, (o)=static

a chance occurrence. Statistically significant meteorological parameters (parameters with p-values less than 0.05 for one or more data sub-set) for Mine 7 include past 24-hour precipitation and solar irradiance. This outcome corroborates the finding by Nissen et al. (2022) that precipitation may be the most influential factor on rockfall. One key difference between that study and this work is the data set analyzed here includes significant snowfall during the Mine 7 deployment. This means the Mine 7 includes both liquid and frozen precipitation, whereas the data set used by Nissen et al. included only liquid precipitation. Solar irradiance had a statistically significant impact on rockfall initiation at Mine 7, however, 24-hour precipitation data subsets included the lowest p-values across all model inputs. Solar irradiance may influence rockfall occurrence through several mechanisms, including thermal expansion of the rock mass, differential heating of rock and air due to solar irradiance (Nigrelli et al., 2022), thawing of ice within rock fractures (D'Amato et al 2016), and increased pore pressure from ice melt.

At Mine 8, temperature, 24-hour precipitation, and solar irradiance have p-values indicating a possible effect on rockfall initiation, with solar irradiance as the most statistically significant parameter. Of the 3,819 rockfalls recorded at Mine 8, 2,368 initiations (61%) occurred between the hours of 07:00 and 17:00. This aligns with the finding that solar irradiance a statistically significant parameter and suggests the warming of rocks during the morning to mid-afternoon hours could be a contributing factor to rockfall initiation.

Solar irradiance and 24-hour precipitation proved to be the most statistically significant parameters at both sites. These mines are in very different climates, with Mine 7 located in southern British Columbia and Mine 8 in the high desert of Arizona. This implies that the influence of solar irradiance and 24-hour precipitation on rockfall initiation transcends local environmental factors unique to each site. Future work will focus on examining these parameters potential for widespread application in rockfall forecasting.

6.4 Limitations and Future Work

The findings of this study highlight the potential for quantitative empirical correlations between rockfall and meteorological forces, and they serve as a basis for continued research into rockfall forecasting. However, confident forecasting will require future work at sites exhibiting a wide diversity of climates, geology, slope design, and other factors, to identify potential site-specific and site-agnostic environmental forces that contribute to rockfall initiation. As part of this continued research, the rockfall detection algorithm's parameters will require further modification, and the results must be validated to bolster confidence in its ability to optimize true detections and limit false detections. Preliminary validation of the algorithm-generated rockfall datasets used in this analysis was conducted as described in Section 6.2.1. However, further validation is necessary to reduce the occurrence of false positives, or instances where non-rockfall movement is identified by the algorithm as rockfall. Ongoing work includes an in-depth validation process involving human review of each algorithm-generated rockfall detection. Future work should include re-running the same analysis and modeling procedures to determine whether the findings are influenced by this more detailed validation effort. Additionally, an evaluation of detection capabilities as a function of the distance between the thermal camera and slope of interest must be performed. The minimum detectable rock size decreases as a function of this distance, but the relationship has not been quantified. This is a critical step since the rockfall detection dataset is the basis for this type of analysis. However, it is possible that the analysis can be performed equally as well at varying distances if the relative patterns of rockfall are similar.

Lastly, the meteorological data analyzed for this study were collected at various locations throughout the mine sites, and therefore serve only as an approximation of the conditions at the slope of interest. All metrics besides precipitation were acquired at the MMP, which was located several thousands of feet away from each slope. Precipitation data was provided by the mine sites and was also collected from locations at significant distances from the slopes. The potential discrepancies between the measured and actual conditions of each slope likely varies between the meteorological factors. For example, isolated monsoon storms affecting the Mine 8 slope may not be captured by the precipitation gauges located elsewhere on the mine site, whereas air temperature measured on the MMP at each site may differ only slightly from the conditions at the slope.

7 Knowledge Dissemination and Impact

This section documents the contributions the project has made in terms of technical publications and presentations, as well as education and outreach efforts.

7.1.1 Journal Articles

Schafer, K., Wellman, E., Ross, B., Potter, J., Kemeny, J., & Williams, C. (2024). *Thermal Imaging Analyses of Pre-Cursory Rockfalls Leading to Large Slope Failures at the Bingham Canyon Mine, USA* [Paper submitted for publication, Rock Mechanics and Rock Engineering].

Wellman, E., Schafer, K., Williams, C., Ojum, G., Potter, J., Brown, L., Meyer, B., Ross, B., & Kemeny, J. (2024). *Observation of Rockfall in the Thermal Infrared* [Paper submitted for publication, Rock Mechanics and Rock Engineering].

7.1.2 Refereed Proceedings

Potter, J., Meyer, B., Ross, B., McNabb, J., Keefner, J., Williams, C., Brown, L., Prescott, B., Cabrejo, A. (2024) *Development of a Prototype Thermal Imaging Rockfall Detection System*. In American Rock Mechanics Association Symposium. Golden, Colorado.

7.1.3 Presentations

Thermal Imaging for Rockfall Detection, Julia Potter and Brad Ross, Colorado Department of Transportation, virtual presentation, December 8, 2022.

Thermal Imaging for Rockfall Detection, Julia Potter and Brad Ross, Association of Geohazard Professionals, virtual presentation, 15 December 2022.

Thermal Imaging for Rockfall Detection, Julia Potter and Chad Williams, Transportation Review Board Rockfall Management Subcommittee, Washington DC, 8 January 2023.

Comparison of Doppler Radar to Thermal Imaging for Rockfall Detection, Bobby Prescott (presenter), Edward Wellman, Brad Ross, Julia Potter, Chad Williams, Jake Davidson, R. Nielsen, SME MINEXCHANGE Annual Conference, Denver, CO, 27 February 2023.

Automated Detection of Rockfalls from Thermal Imaging Data, Benjamin Meyer (presenter), Leonard Brown, Julia Potter, Bobby Prescott, Brad Ross, Chad Williams, SME MINEXCHANGE Annual Conference, Denver, CO, 28 February 2023.

Thermal Imaging for Rockfall Detection, Leonard Brown, Learning Laboratories Quarterly Meeting, virtual presentation, 15 March 2023.

Application of Thermal Infrared Cameras for Rockfall Detection, Julia Potter, RocScience 2023 Conference, Toronto, ON, 22 April 2023.

Application of Thermal Infrared Cameras for Rockfall Detection, Julia Potter, Life of Mine – Maintaining Sustainability through Geoscience, virtual presentation, May 2023.

Thermal Imaging for Rockfall Detection: Project Updates and Standalone System Development, Benjamin Meyer, Bobby Prescott, and James McNabb, GroundProbe Users Conference, Tucson, AZ, August 18, 2023.

Thermal Imaging for Rockfall Detection, Leonard Brown, South Dakota School of Mines & Technology Seminar Series, virtual presentation, 13 September 2023.

Automated Detection of Rockfall in the Thermal Infrared, Benjamin Meyer and Julia Potter, Transportation Review Board Rockfall Management Subcommittee, Washington DC, 7 January 2024.

Automated Rockfall Detection Using Thermal Imaging: Recent Developments in Tracking, Prediction, and Alarming, Benjamin Meyer (presenter), Leonard Brown, Julia Potter, James McNabb, Brad Ross, Chad Williams, SME MINEXCHANGE Annual Conference, Phoenix, AZ, 28 February 2023.

Geotechnical Applications of Thermal Imaging: Observations and Recommendations, Julia Potter (presenter), Benjamin Meyer, Leonard Brown, James McNabb, Brad Ross, Chad Williams, SME MINEXCHANGE Annual Conference, Phoenix, AZ, 28 February 2023.

7.1.4 Educational Outreach Events

The research team assisted with several outreach events throughout the duration of the project, including:

- **Mining Engineering Day at Summer Engineering Academy (SEA) events between 2022 and 2024.** SEA is a summer outreach program for rising 9th through 12th graders, who want to learn more about engineering. Participating students were introduced to the role of monitoring in open pit mining, and specifically how thermal imaging and drones can be used to improve miner safety.
- **Mines for Limitless Minds, a mining-specific career fair organized by the School of Mining and Mineral Resources at the University of Arizona in 2022 and 2023.** The research team set up a “thermal portrait” booth, where students were introduced to the concept of thermal imaging for detecting movement. The GCE also organized a drone obstacle course as part of this event.

7.2 Student Involvement and Impact

Students involved in the project gained hands-on experience with thermal cameras and video monitoring systems. Multiple students assisted in managing the video recording and export process on the MMP through remote connections to the FLIR Meridian NVR system. Additionally, students were instrumental in reviewing the thermal video archives for rockfall events and extracting small video clips from the Phase 1 video archives for use in calibrating the automatic detection algorithm for individual sites. Students assisted in testing the physical setup of the prototype standalone system. Student assistance was also vital in project outreach. Students attended SME state and national conferences to spread awareness about the project as part of the University of Arizona booth while also giving conference attendees the chance to interact with and learn about thermal cameras through having thermal portraits made.

8 Conclusions and Future Work

Cost-efficient options for real-time rockfall detection and monitoring are a critical need in the mining industry. In a collaborative effort with NIOSH and industry partners, the GCE has demonstrated the viability of using commercial off-the-shelf thermal cameras and moderate computing hardware to automatically detect and alert for rockfall in open pit mining environments. Significant components of this work included the creation of an automated detection algorithm, new developments in rockfall monitoring systems, and new approaches for failure forecasting which will inform future strategic monitoring initiatives. Notably, a prototype tactical monitoring system using thermal imaging cameras has been successfully developed and tested in a non-active mining environment, achieving technology readiness level TRL6 (prototype demonstration in relevant environment). Using heuristics and motion filter approaches, the prototype system can reliably identify and track rockfall events under a variety of environmental and geotechnical conditions at rates that are comparable to human observers. Furthermore, the system facilitates longitudinal analysis of slope stability, leading to new findings, such as the potential influence of solar irradiance on rockfall initiation, which are useful in developing new predictive models for rockfall forecasting.

Field testing of the prototype system also yielded valuable insights to improve the hardware and software components. For example, deployment of the prototype system resulted in a greater understanding of the ideal physical characteristics of a thermal rockfall detection device as well as a more efficient software solution for real-time rockfall detection and tracking that will support less powerful computing devices. The resulting integrated hardware and software system represents a significant step toward enhancing situational awareness and addressing the safety risks posed by rockfall, which will continue to be improved through future research, testing, and prototyping.

Future work should focus on optimizing the data acquisition system for short-term, tactical monitoring of safety critical areas, while also exploring the applicability of this technology for long-term, strategic monitoring use cases. Three specific recommendations for future work are outlined below.

8.1 Development of Marketable Tactical Thermal Rockfall Monitoring System

To realize a commercially deployable system, the following two steps are required: 1) final development and adaptation of the Phase 2 algorithm and software for tactical applications and 2) final development and adaptation of the data acquisition system to a marketable tool for reliable, tactical monitoring of safety-critical areas.

Development and Adaptation of Tactical Monitoring Software. The Phase 2 prototype software establishes a groundwork for development of a commercially viable software system for detecting, tracking, and alarming for rockfall. Final development will include gathering feedback from industry focus groups, incorporating research findings regarding complementary technologies, and developing a front-end user interface to increase usability and facilitate deployment across various operating systems and hardware.

Development and Adaptation of Tactical Monitoring System. A tactical solution will involve further development of the existing standalone prototype, with enhancements made based on experience gained during Phase 2. For example, while setup and tailoring of the system can be done in less than 20 minutes, ease of portability could be improved. The separate computer, PoE system, camera, and tripod are difficult for a single operator to carry. Currently, the unit requires ground shipping as

“hazardous goods” due to battery size, limiting the ability to quickly deploy to a location beyond driving distance. The resulting product may be used for tactical monitoring of safety-critical areas when rapid data generation and alarming is needed (e.g., personnel working in high rockfall risk areas). Final development of the tactical monitoring system will include further research into necessary hardware, power systems, computing capability improvements, and additional prototype development.

8.1.1 Comparison with Alternative and Complementary Technologies

A robust monitoring program relies on the integration of diverse hazard detection technologies for cross-validating detections. Comparison with alternate and complementary technologies will also improve market awareness by identifying opportunities in the existing market. It is therefore important that multiple technologies are researched to identify synergies and potential integrations between tools. Commercially available real-time rockfall solutions are currently limited to Doppler radar units (e.g., IDS GeoRadar’s RockSpot, GroundProbe’s Petra), which are costly and have limitations in range, resolution, and atmospheric changes. Other solutions like LiDAR and photogrammetry can map rockfall locations and measure volumes but are trailing indicators lacking temporal resolution (Walton et al., 2023).

A thermal rockfall monitoring solution would provide important cross-validation functionality and has the potential to improve the effectiveness and reliability of existing systems. For example, combining a thermal monitoring solution with a Doppler radar unit could potentially improve overall system range, reliability, and situational awareness. Preliminary work comparing thermal imaging with Doppler radar units was completed during Phase 1 of the project, but this was done before the Phase 2 algorithm was developed (Prescott, et al., 2022). The Phase 2 algorithm provides new opportunities to improve detection reliability and sensitivity which should be thoroughly evaluated against Doppler solutions using a quantitative evaluation framework. Furthermore, combining thermal monitoring with LiDAR or photogrammetry would allow for post-rockfall analysis, including volumetric calculations and high-resolution mapping of initiation and deposition regions.

Throughout Phases 1 and 2, the GCE has fostered relationships with monitoring system providers, mining companies, and other individuals and researchers currently marketing or using these alternate technologies. These relationships should be leveraged to ensure a collaborative approach in comparing and integrating diverse hazard detection technologies. Field work may be completed using the Phase 2 prototype algorithm in conjunction with the GCE’s Mobile Monitoring Platform (developed during project Phase 1), the Phase 2 prototype data acquisition system, and an advanced prototype system discussed below (Section 8.3).

8.2 Development of Prototype Strategic Thermal Monitoring Tools

Phases 1 and 2 have demonstrated the efficacy of thermal video in reliable detection and tracking of rockfall in open pit mining environments (Prescott et al., 2022; Ross et al., 2022; Wellman et al., 2022; Schafer et al., 2023). Furthermore, previous work has documented the exponential increase in frequency of rockfall before a major slope failure event (Schafer et al., 2023). Observations made by the GCE, along with prior studies, suggest additional geotechnical use cases for thermal imagery that have the potential to enhance miner safety (e.g. Guerin et al., 2019; Schafer et al., 2023; Rosser et al., 2007). Work completed thus far has focused on development of a tactical rockfall monitoring solution that provides alarming capabilities for safety critical areas. Further research is needed to better understand and document potential applications of thermal imaging beyond tactical rockfall monitoring. Strategic thermal monitoring and analytical tools should be explored for:

- Detecting, delineating, and monitoring the evolution of groundwater seeps, which can provide information about the state of potentially destabilizing groundwater in the slope.
- Evaluating catch bench performance based on the data output from the Phase 2 algorithm.
- Monitoring large-scale slope movements to inform slope management and time-of-failure predictions (Schafer et al., 2023; Rosser et al., 2007).
- Identifying rock bridges and thus potential points of future failure in a mining environment, expanding upon methods used on El Capitan in Yosemite National Park (Guerin et al., 2019).

8.3 Rockfall Forecasting and Statistical Modeling

The objective of this phase of the project was to support the development of weather-related trigger action response plans for geotechnical engineers. To achieve this, the following tasks were completed:

1. Construction of two databases:
 - a. A rockfall database generated by the GCE's automated rockfall detection algorithm from archived thermal video from Mines 7 and 8.
 - b. A meteorological database compiled from temperature, precipitation, wind speed, and solar irradiance data collected during deployment.
2. Empirical data analysis to prioritize meteorological parameters based on their predictive power. This was done by combining both databases to calculate Weight of Evidence and Information Value for each meteorological parameter.
3. Logistic regression modeling to establish relationships between meteorological parameters and rockfall occurrence. Parameters identified as potential predictors in the previous task were combined with the rockfall dataset to build site-specific logistic regression models.

Initial models without segmentation of meteorological data had limited predictive power. To improve this, segmentation through binning and trend categorization was introduced. The results indicate that models with segmentation (binning and trend categorization) show improved predictive performance. Statistically significant parameters across both sites include solar irradiance and 24-hour precipitation, suggesting these factors have a broad influence on rockfall initiation, regardless of local climate differences.

Future work will build on the findings detailed in Section 6 and focus on refinement of the modeling procedures. A more exhaustive validation effort is currently under way involving detailed human review of all algorithm-identified events from the Mine 7 and Mine 8 datasets. The analysis and modeling will then be re-run with the validated dataset to determine whether the findings are impacted by the reduction of any existing false positives. The results of this effort will also be used to further refine the algorithm and better understand the site-specific parameters necessary to reduce false positives. Additionally, future work should explore the application of different classification methods to improve the accuracy of rockfall forecasting.

9 Acknowledgments

The research presented in this report would not have been possible without research collaboration and funding provided by industry, government, and academic collaborators. The Geotechnical Center of Excellence gratefully acknowledges the financial support provided by the National Institute of Occupational Safety and Health (NIOSH BAA#: 75D301-22-R-61070) and the ongoing support of our industry members. Data gathering across both phases of this project was possible due to research collaboration agreements with ASARCO, Capstone Copper, Elk Valley Resources, Freeport McMoRan, Inc., Kinross Gold, Newmont, Rio Tinto, and Teck Resources. Sean Warren at NIOSH provided thermal video of human-induced rockfall from the Highwall Safety Project which was used for design and calibration of the automated detection algorithm. Kirk Schafer was instrumental in facilitating the comparison between human and algorithm rockfall detection prior to the Leo slope failure at the Bingham Canyon Mine. We thank GroundProbe, Inc. for construction and maintenance of the prototype tactical system, Canary Systems for donating additional hardware to extend the capabilities of the tactical system, and IDS for guidance and maintenance of the MMP system constructed during Phase 1. We are grateful to James Warner for facilitating system testing and development at the University of Arizona's San Xavier Mining Laboratory. We also acknowledge the Rio Tinto Kennecott personnel who graciously supported the MMP deployment during this study: Dustin Gale, Dustin Hicks, Jon Lytle, Alexander Urive, Steven Moore, and Taylor Gallagher.

This paper benefited from the thoughtful reviews of Andrew Bidwell, Megan Gaida, Heather Lawson, Jessica Azure, Lucho Tejada-Alvarez, Hanjalika Hazwezwe, and John Combs. Any remaining errors or omissions are the authors' own.

The University of Arizona and the School of Mining and Mineral Resources provides a home and support for the GCE's research efforts. We respectfully acknowledge the University of Arizona is on the land and territories of Indigenous peoples. Today, Arizona is home to 22 federally recognized tribes, with Tucson being home to the O'odham and the Yaqui. Committed to diversity and inclusion, the University strives to build sustainable relationships with sovereign Native Nations and Indigenous communities through education offerings, partnerships, and community service.

[Note on Text Rephrasing:](#)

Certain sections of this report have been rephrased using ChatGPT, an AI language model developed by OpenAI, to enhance clarity and readability. The use of this tool was limited to language refinement, and all technical content and conclusions are the original work of the authors.

References

- Beale, G., & Read, J., eds. (2014). Guidelines for evaluating water in pit slope stability. CSIRO Publishing.
- Bhalla, Deepanshu. “Weight of Evidence (WOE) and Information Value (IV) Explained.” ListenData (blog). Accessed June 10, 2024. <https://www.listendata.com/2015/03/weight-of-evidence-woe-and-information.html>.
- Cloud Software Group, Inc. “Information Value and Weight of Evidence Analysis.” Concept. Cloud Software Group, Inc. Accessed June 27, 2024. https://docs.tibco.com/pub/sfire-dsc/6.5.0/doc/html/TIB_sfire-dsc_user-guide/GUID-07A78308-525A-406F-8221-9281F4E9D7CF.html.
- D’Amato, J., Didier, H., Guerin, A., Jaboyedoff, M., Baillet, L., & Mariscal, A. (2016). “Influence of Meteorological Factors on Rockfall Occurrence in a Middle Mountain Limestone Cliff.” *Natural Hazards and Earth System Sciences* 16, no. 3 (March 15, 2016): 719–35. <https://doi.org/10.5194/nhess-16-719-2016>.
- Duque, L.F. (2020). “IETD: Inter-Event Time Definition,” March 10, 2020. <https://doi.org/10.32614/CRAN.package.IETD>.
- Guerin, A., Jaboyedoff, M., Collins, B.D., Derron, M.H., Stock, G.M., Matasci, B., Boesiger, M., Lefevre, C., and Podladchikov, Y.Y. (2019). “Detection of Rock Bridges by Infrared Thermal Imaging and Modeling.” *Scientific Reports* 9 (1): 13138. <https://doi.org/10.1038/s41598-019-49336-1>.
- Kalman, R. E. (1960). “A New Approach to Linear Filtering and Prediction Problems.” *ASME. Journal of Basic Engineering*, 82(1) (March 1, 1960): 35–45. <https://doi.org/10.1115/1.3662552>.
- “Logistic Regression: Definition, Use Cases, Implementation.” Accessed August 26, 2024. <https://encord.com/blog/what-is-logistic-regression/>.
- Macciotta, R. (2019). “Review and Latest Insights into Rock Fall Temporal Variability Associated with Weather.” *Geotechnical Engineering* 172 (March 8, 2019). <https://doi.org/10.1680/jgeen.18.00207>.
- Munkres, J. (1957). “Algorithms for the Assignment and Transportation Problems.” *Journal of the Society for Industrial and Applied Mathematics* 5, no. 1 (1957): 32–38. <https://doi.org/10.1137/0105003>.
- Nigrelli, Guido, Marta Chiarle, Andrea Merlone, Graziano Coppa, and Chiara Musacchio. “Rock Temperature Variability in High-Altitude Rockfall-Prone Areas.” *Journal of Mountain Science* 19, no. 3 (March 1, 2022): 798–811. <https://doi.org/10.1007/s11629-021-7073-z>.
- Nissen, K. M., Rupp, S., Kreuzer, T. M., Guse, B., Damm, B., & Ulbrich, U. (2022). “Quantification of Meteorological Conditions for Rockfall Triggers in Germany.” *Natural Hazards and Earth System Sciences* 22, no. 6 (June 23, 2022): 2117–30. <https://doi.org/10.5194/nhess-22-2117-2022>.
- Pedro J.R.P., & Eagleson, P. S. (1982) “Identification of Independent Rainstorms.” *Journal of Hydrology* 55, no. 1 (February 1, 1982): 303–19. [https://doi.org/10.1016/0022-1694\(82\)90136-6](https://doi.org/10.1016/0022-1694(82)90136-6).
- Prescott, B., Wellman, E. C., Ross, B. J., & Potter, J.J. (2022). “Comparison of Doppler Radar to Thermal Infrared Rockfall Detection.” In *Slope Stability Symposium*. Tucson, Arizona.

- Robinson, J. D., Vahedifard, F., & AghaKouchak, A. (2017). Rainfall-triggered slope instabilities under a changing climate: Comparative study using historical and projected precipitation extremes. *Canadian Geotechnical Journal*, 54(1), 117–127. <https://doi.org/10.1139/cgj-2015-0602>
- Rosser, N., Lim, M., Petley, D., Dunning, S., & Allison, R. (2007) “Patterns of Precursory Rockfall Prior to Slope Failure.” *Journal of Geophysical Research* 112, no. F4 (December 19, 2007): F04014. <https://doi.org/10.1029/2006JF000642>.
- Schafer, K., Bakken, K., Ergun, S., Potter, J.J., Ross, B.J., Telfer, J., & Williams, C.P. (2023) “Rockfalls as Precursory Strain Indicators Leading to a Large Slope Failure (‘Leo Failure’) at Bingham Canyon Mine, USA.” In *SSIM 2023: Third International Slope Stability in Mining Conference*, 721–32. Australian Centre for Geomechanics, Perth, 2023. https://doi.org/10.36487/ACG_repo/2335_49.
- Siddiqi, Naeem, ed. *Credit Risk Scorecards: Developing and Implementing Intelligent Credit Scoring*. 1st ed. Wiley, 2006. <https://doi.org/10.1002/9781119201731>.
- Sidele, R.C. (2007). Using Weather and Climate Information for Landslide Prevention and Mitigation. In *CLIMATE AND LAND DEGRADATION* (Issue 9783540724377, pp. 285–307). Springer Berlin Heidelberg. https://doi.org/10.1007/978-3-540-72438-4_15.
- Walton, G., & Weidner, L. (2023). “Accuracy of Rockfall Volume Reconstruction from Point Cloud Data—Evaluating the Influences of Data Quality and Filtering.” *Remote Sensing* 15, no. 1: 165. <https://doi.org/10.3390/rs15010165>.
- Wellman, E. C., Schafer, K. W., Prescott, B., Williams, C. P., and Ross, B. J. (2022). “Findings from the Thermal Imaging for Rockfall Detection Project.” In *Slope Stability Symposium*. Tucson, Arizona.

Appendix A: Details of Automated Rockfall Detection Process

A.1: Overall Algorithmic Process

The detection algorithm consists of the following steps:

- Create averaged background
- Compare current image to background
- Identify motion regions
- Motion prediction
- Track assignment
- Evaluate movement
- Alarm

In order to identify and track separate moving objects which may appear intermittently or simultaneously, a tracking data structure is built for each identified movement.

A.2: Movement Tracks

Each moving object is recorded and monitored by a “track” – a data structure including information about the movement’s origin, pathway over time, speed, and a built-in location prediction (Kalman filter).

A.3: Create Averaged Background

Thermal video is inherently noisy. Surface temperatures observed during the project can fluctuate rapidly. Figure A-1 shows point temperature fluctuations over 29 frames of thermal video (approximately 2 seconds) recorded using a FLIR A400 radiometric thermal camera. Motion detection in video relies on brightness comparisons between frames. To minimize false motion detections, per-pixel brightness values are averaged over the previous 50 frames to create a background image for comparison with the current video frame.



Figure A-1. Depiction of Thermal Video Noise. The left frame shows a detail of a radiometric thermal video taken with the FLIR A400 scientific thermal camera, with a single pixel highlighted. The right frame shows the temperature change of this pixel over 29 frames, representing approximately 2 seconds of elapsed time.

A.4: Compare current image to background

The averaged background brightness values and the current pixel values are differenced (subtracted). The absolute value of the result is then compared with a user-defined threshold, and any pixel with a change exceeding this value is considered a “motion.” A new binary image (all pixels are either 100% black or 100% white) is created, and any identified motion pixels are set to white in this image (Figure A-2).

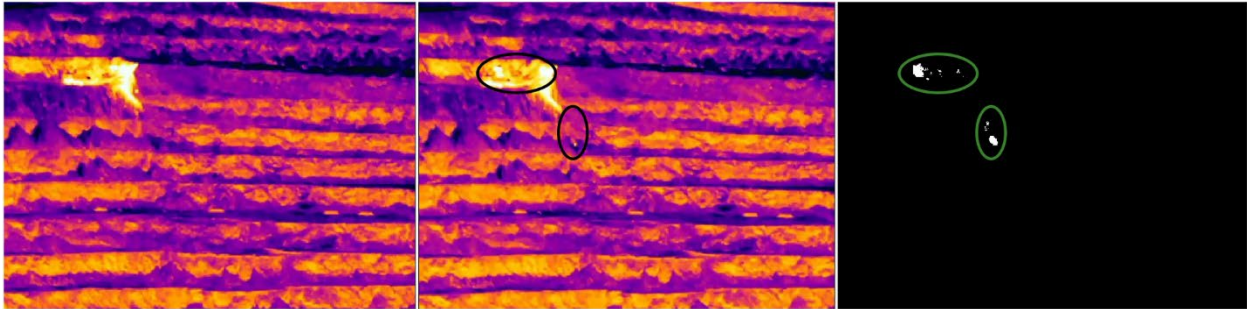


Figure A-2. Background Segmentation Process. The left frame represents the averaged background image. The center frame shows the current frame, with differences to the background image highlighted (black ovals). The right frame shows the built binary image with white regions indicating areas of difference between current and background frames (highlighted in green ovals for visibility).

A.5: Identify motion regions

Each contiguous area of white pixels in the binary image is considered an area of motion. Optionally, the outer edge of the pixel areas can be expanded and then contracted (closing holes inside of areas of motion and merging multiple small moving objects into a single larger motion). This can reduce the number of nearby movements tracked (Figure A-3). If this optional step is performed it is important that the edges of motion regions not be contracted more than they were expanded, and expansion must happen before contraction. Failing to follow these guidelines could result in completely losing very small areas of motion.



Figure A-3. Motion Region Refinement. The left frame represents the areas of motion identified in the right frame of Figure A-2 above. The right frame shows these regions after the dilation and contraction process, consolidating nearby movements.

A.6: Motion prediction

Each track's internal Kalman filter is queried to determine the expected current position of all known moving objects (Figure A-4). The Kalman filter builds an estimate based on past object locations and velocity. The results of those estimates are then passed to the track assignment step.

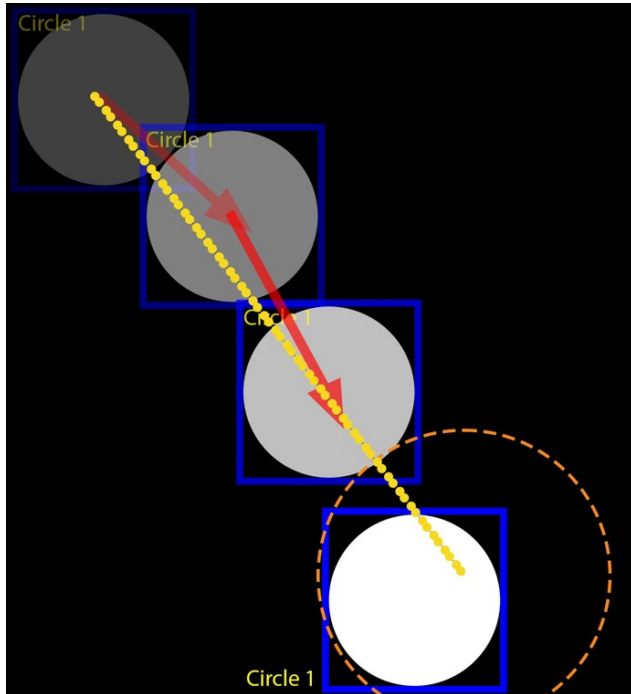


Figure A-4. Kalman Filtering of Motion Detections Over Time. The white circle and gray box represent the current location of a moving object, and the darker gray circles and boxes are previously identified locations of the same moving object. Red arrows represent movement of the object between individual detections. Based on the previous locations of the object, a projected direction/speed is estimated (yellow dotted line), and the estimated new location region is defined (orange dashed circle). Current-frame movement detections within this area will be evaluated as possible continuations of the observed object's movement.

A.7: Track assignment

The Munkres/Hungarian algorithm with thresholding is used to determine the best match between existing tracked objects and the current frame's movements. A linear least squares comparison is performed, with a cost threshold that adjusts likelihood of assignment vs non-assignment. Possible outcomes of this process follow:

- Match between a motion and an existing track
 - The existing track's current position is updated with the assigned motion results
- Track with no matching motion
 - The track is flagged as "unseen" and the expected location is updated for the next frame.
- Motion with no matching track
 - The motion is identified as a new moving object. A track is created for the new object

At the end of this step, all motions are associated with a track (Figure A-5).

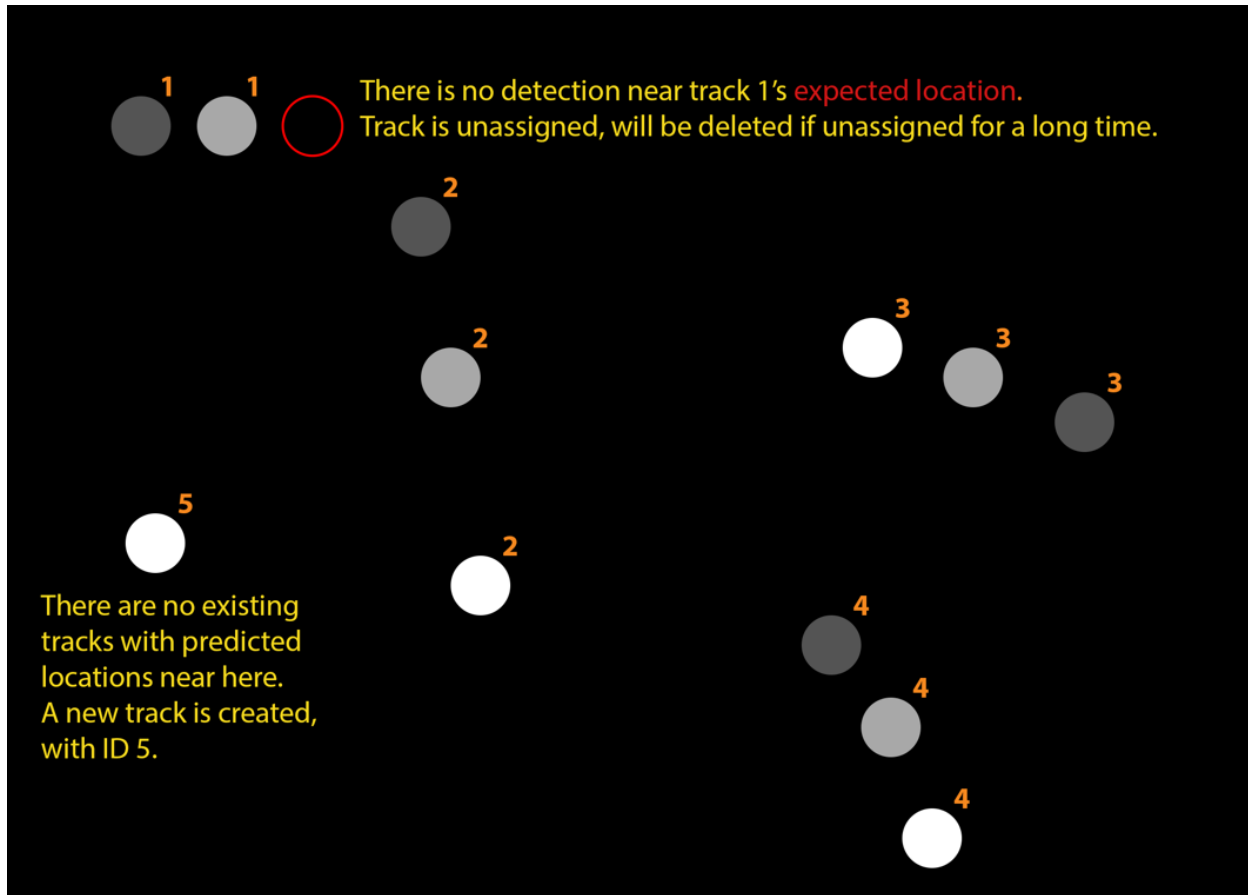


Figure A-5. Assignment of Movement Detections to Tracks. Individual tracks are labeled with orange numbers. The dark gray circles represent the position of the object 2 frames ago, medium gray circles represent the position of the object 1 frame ago, and white circles represent current position. The red circle to the right of track 1 indicates the expected position of the tracked movement based on the track's internal Kalman filter prediction.

A.8: Evaluate Movement

Each track's motion is evaluated heuristically. In order to separate hazardous falling objects from other movements, track movements are compared to direction, speed, and motion consistency criteria. Direction of motion is compared to an allowable cone of fall angles (which can be adjusted based on underlying slope characteristics). Speed of motion is compared to minimum and maximum thresholds. Motions which have been tracked as moving upwards for more than a threshold length of time are eliminated from consideration. Movements that meet all of these criteria are designated as "falling" objects. These falls are then compared to a minimum fall distance (in pixels) and time (in frames). Falling objects which exceed these minimums are designated as hazardous falling objects and alarmed for.

A.9: Alarm

The rockfall detection system has multiple alert options.

A.9.1: Visual

The visual alerts have adjustable options for width and color. By default, fall events that are spatiotemporally distinct are represented on-screen by different colors of movement traces (Figure

A-6). Falling rocks can break apart or dislodge other debris, and the resulting secondary fall events share a color with their “parent” event. The randomization of colors can be disabled in favor of a singular alert color if desired. The surface area magnitude of the fall event is represented by line width of the motion trace, which is based on the natural log of the moving surface area (larger apparent movements are traced with thicker lines).

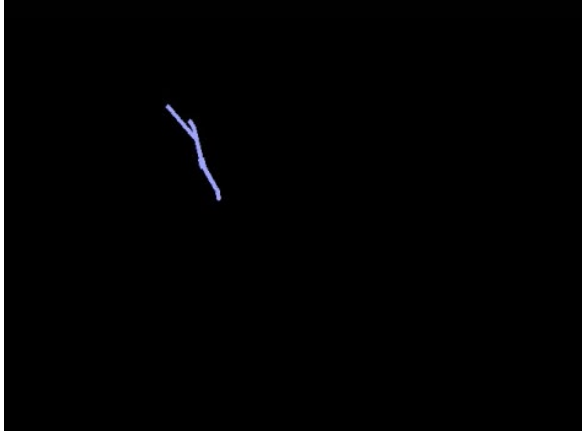


Figure A-6. Visual Trace/Alert of Movement Extracted from a Thermal Video. The blue line represents the motion trace of a rockfall event.

A.9.2: Audio

Audio alerts are currently implemented for computers using the Windows operating system. The current audio alarm sound is a system alert/error sound repeated every 0.5 seconds during a detected fall, and ends once the falling motion is no longer detected.

A.9.3: File output

Rockfall events can be written to a text file in .csv format. Algorithm outputs used for the empirical correlations described in Section 6 recorded the initiation of any rockfall discovered in the phase 1 thermal video recordings from Mines 7 and 8. The output files included timestamp, 2D pixel location, source video file, and frame number of the detection. Timestamps for archived sources are calculated by the video start time (included in filename), frame number, and framerate, and are thus unaffected by the speed or system time of the computer running the algorithm.

Appendix B: Meteorological Data and Modeling Results

B.1 Precipitation Events

Precipitation events were delineated using the Coefficient of Variation method for calculation of Inter-Event Time Definition, which determines the minimum time between precipitation pulses to consider them as coming from independent precipitation events.

Table B-1: Precipitation Events and Intensity of Precipitation Event at each Mine.

Mine 7		Mine 8	
Event	Intensity (mm/hr)	Event	Intensity (mm/hr)
1	0.38	1	1.55
2	0.18	2	1.10
3	0.27	3	6.99
4	0.21	4	1.16
5	0.46	5	1.69
6	0.14	6	0.52
7	0.07	7	2.23
8	0.11	8	0.64
9	0.37	9	1.82
10	0.40	10	1.54
11	0.10	11	2.09
12	0.15	12	6.33
13	1.10	13	0.70
14	0.18	14	0.32
15	0.57	15	6.02
16	0.13	16	1.25
17	0.17	17	0.67
18	0.41	18	3.65
19	0.16	19	1.71
20	0.28	20	0.64
21	0.16	-	-
22	0.55	-	-
23	0.14	-	-
24	0.32	-	-
25	0.13	-	-
26	0.10	-	-
27	0.23	-	-
28	0.79	-	-
29	0.18	-	-
30	0.06	-	-
Average	0.28	Average	2.13

B.2 Weight of Evidence and Information Value

Table B-2: Raw Calculated Values for Weight of Evidence (WOE) & Information Value (IV) at Mine 7. Event refers to an instance of rockfall initiation observed while Non-Event refers to an instance of no rockfall initiation observed.

Temperature								
Bin	Instance Count	Percent Total Instances	Non-Event	Event	Event Empirical Probability	WOE	Bin IV	Parameter IV
[-Inf,-29.45)	1	0.08%	0	1	100.00%	-7.54E-01	1.04E-03	2.79E-02
[-29.45,-14.71)	101	8.44%	44	57	56.44%	-5.05E-01	2.31E-02	2.79E-02
[-14.71,0.02)	898	75.02%	275	623	69.38%	5.37E-02	2.14E-03	2.79E-02
[0.02,14.77)	196	16.37%	60	136	69.39%	5.42E-02	4.76E-04	2.79E-02
[14.77,Inf)	1	0.08%	1	0	0.00%	-7.74E-01	1.09E-03	2.79E-02
Wind								
[-Inf,1.76)	943	78.78%	295	648	68.72%	2.40E-02	4.53E-04	8.77E-03
[1.76,3.52)	209	17.46%	71	138	66.03%	-9.83E-02	1.71E-03	8.77E-03
[3.52,5.23)	37	3.09%	13	24	64.86%	-1.50E-01	7.11E-04	8.77E-03
[5.23,7.05)	7	0.58%	1	6	85.71%	1.03E+00	4.86E-03	8.77E-03
[7.05,Inf)	1	0.08%	0	1	100.00%	-7.53E-01	1.03E-03	8.77E-03
Solar Irradiance								
[-Inf,261.50)	995	83.20%	296	700	70.28%	9.79E-01	7.82E-03	4.89E-02
[261.50,522.83)	102	8.52%	44	58	56.8%	-4.87E-01	2.17E-02	4.89E-02
[522.83,784.15)	75	6.26%	33	42	56.00%	-5.21E-01	1.84E-02	4.89E-02
[784.15,1045.47)	23	1.92%	7	16	69.56%	6.38E-02	7.73E-05	4.89E-02
[1045.47,Inf)	1	0.08%	0	1	100.00%	-7.53E-01	1.03E-03	4.89E-02
Precipitation								
[-Inf,0.51)	1184	98.91%	377	807	68.16%	-4.21E-03	1.75E-05	1.52E-02
[0.51,1.03)	10	0.84%	1	9	90.00%	1.43E+00	1.20E-02	1.52E-02
[1.03,1.54)	1	0.08%	1	0	0.00%	-7.75E-01	1.10E-03	1.52E-02
[1.54,2.05)	1	0.08%	1	0	0.00%	-7.75E-01	1.10E-03	1.52E-02
[2.05,Inf)	1	0.08%	0	1	100.00%	-7.55E-01	1.04E-03	1.52E-02
Rolling Sum of Precipitation Past 24 Hours								
[-Inf,1.89)	1047	87.47%	340	707	67.53%	-3.34E-02	9.81E-04	6.40E-02
[1.89,3.78)	79	6.60%	18	61	77.22%	4.55E-01	1.24E-02	6.40E-02
[3.78,5.67)	30	2.51%	3	27	90.00%	1.43E+00	3.60E-02	6.40E-02
[5.67,7.56)	25	2.09%	12	13	52.00%	-6.85E-01	1.07E-02	6.40E-02
[7.56,Inf)	16	1.34%	7	9	56.25%	-5.14E-01	3.81E-03	6.40E-02
Precipitation Intensity								
[-Inf,0.18)	1154	96.41%	371	783	67.85%	-1.33E-02	1.72E-04	1.28E-02
[0.18,0.37)	9	0.75%	1	8	88.89%	1.32E+00	9.46E-03	1.28E-02
[0.37,0.55)	31	2.59%	8	23	74.19%	2.96E-01	2.13E-03	1.28E-02
[0.55,0.73)	1	0.08%	0	1	100.00%	-7.50E-01	1.03E-03	1.28E-02
[0.73,Inf)	2	0.17%	0	2	100.00%	-5.71E-02	8.21E-06	1.28E-02
Freezing Potential								
[-Inf,7.37)	843	70.43%	247	596	70.70%	1.18E-01	9.58E-03	8.55E-02
[7.37,14.73)	253	21.14%	89	164	64.82%	-1.52E-01	4.98E-02	8.55E-02
[14.73,22.10)	86	7.18%	43	43	50.00%	-7.63E-01	4.59E-02	8.55E-02
[22.10,29.46)	14	1.17%	1	13	92.86%	1.80E+00	2.39E-02	8.55E-02
[29.46,Inf)	1	0.08%	0	1	100.00%	-7.53E-01	1.03E-03	8.55E-02

Table B-3: Raw Calculated Values for Weight of Evidence (WOE) & Information Value (IV) Mine 8. Event refers to an instance of rockfall initiation observed while Non-Event refers to an instance of no rockfall initiation observed.

Temperature								
Bin	Instance Count	Percent Total Instances	Non-Event	Event	Event Empirical Probability	WOE	Bin IV	Parameter IV
[-Inf,22.49)	239	11.85%	96	143	59.83%	5.82E-01	4.01E-02	1.89E-01
[22.49,28.44)	693	34.36%	433	260	37.52%	-3.26E-01	3.57E-02	1.89E-01
[28.44,34.39)	520	25.78%	333	187	35.96%	-3.93E-01	3.86E-02	1.89E-01
[34.39,40.34)	437	21.67%	193	244	55.84%	4.18E-01	3.81E-02	1.89E-01
[40.34,Inf)	128	6.35%	46	82	64.06%	7.62E-01	3.64E-02	1.89E-01
Wind								
[-Inf,1.08)	1806	89.54%	978	828	45.85%	1.73E-02	2.67E-04	3.64E-03
[1.08,2.16)	195	9.67%	115	80	41.03%	-1.79E-01	3.07E-03	3.64E-03
[2.16,3.24)	14	0.69%	7	7	50.00%	1.84E-01	2.36E-04	3.64E-03
[3.24,4.32)	1	0.05%	1	0	0.00%	1.74E-01	2.99E-05	3.64E-03
[4.32,Inf)	1	0.05%	0	1	100.00%	1.94E-01	3.72E-05	3.64E-03
Solar Irradiance								
[-Inf,288.24)	1461	72.43%	857	604	41.34%	-1.66E-01	1.97E-02	9.20E-02
[288.24,576.47)	119	5.90%	38	81	68.07%	9.41E-01	5.07E-02	9.20E-02
[576.47,864.71)	157	7.78%	75	82	52.23%	2.73E-01	5.84E-03	9.20E-02
[864.71,1152.95)	263	13.04%	125	138	52.47%	2.83E-01	1.05E-02	9.20E-02
[1152.95,Inf)	17	0.84%	6	11	64.71%	7.90E-01	5.18E-03	9.20E-02
Precipitation								
[-Inf,5.28)	1995	98.91%	1101	894	44.81%	-2.07E-02	4.23E-04	5.21E-02
[5.28,10.58)	15	0.74%	0	15	100.00%	2.91E+00	4.50E-02	5.21E-02
[10.58,15.86)	4	0.20%	0	4	100.00%	1.58E+00	5.50E-03	5.21E-02
[15.86,26.43)	1	0.05%	0	1	100.00%	1.98E-01	3.87E-05	5.21E-02
[26.43,Inf)	2	0.10%	0	2	100.00%	8.91E-01	1.15E-03	5.21E-02
Rolling Sum of Precipitation Past 24 Hours								
[-Inf,10.73)	1715	85.03%	957	758	44.20%	-4.83E-02	1.97E-03	2.83E-02
[10.73,21.46)	187	9.27%	99	88	47.06%	6.71E-02	4.18E-04	2.83E-02
[21.46,32.19)	71	3.52%	32	39	54.93%	3.83E-01	5.18E-03	2.83E-02
[32.19,42.93)	42	2.08%	13	29	69.05%	9.87E-01	1.96E-02	2.83E-02
[42.93,Inf)	2	0.10%	0	2	100.00%	8.88E-01	1.14E-03	2.83E-02
Precipitation Intensity								
[-Inf,3.55)	1987	98.51%	1098	889	44.75%	-2.44E-02	5.90E-05	4.71E-02
[3.55,7.11)	23	1.14%	3	20	86.96%	2.08E+00	3.98E-02	4.71E-02
[7.11,10.66)	1	0.05%	0	1	100.00%	1.97E-01	3.84E-05	4.71E-02
[10.66,17.77)	4	0.20%	0	4	100.00%	1.58E+00	5.49E-03	4.71E-02
[17.77,Inf)	2	0.10%	0	2	100.00%	8.89E-01	1.14E-03	4.71E-02

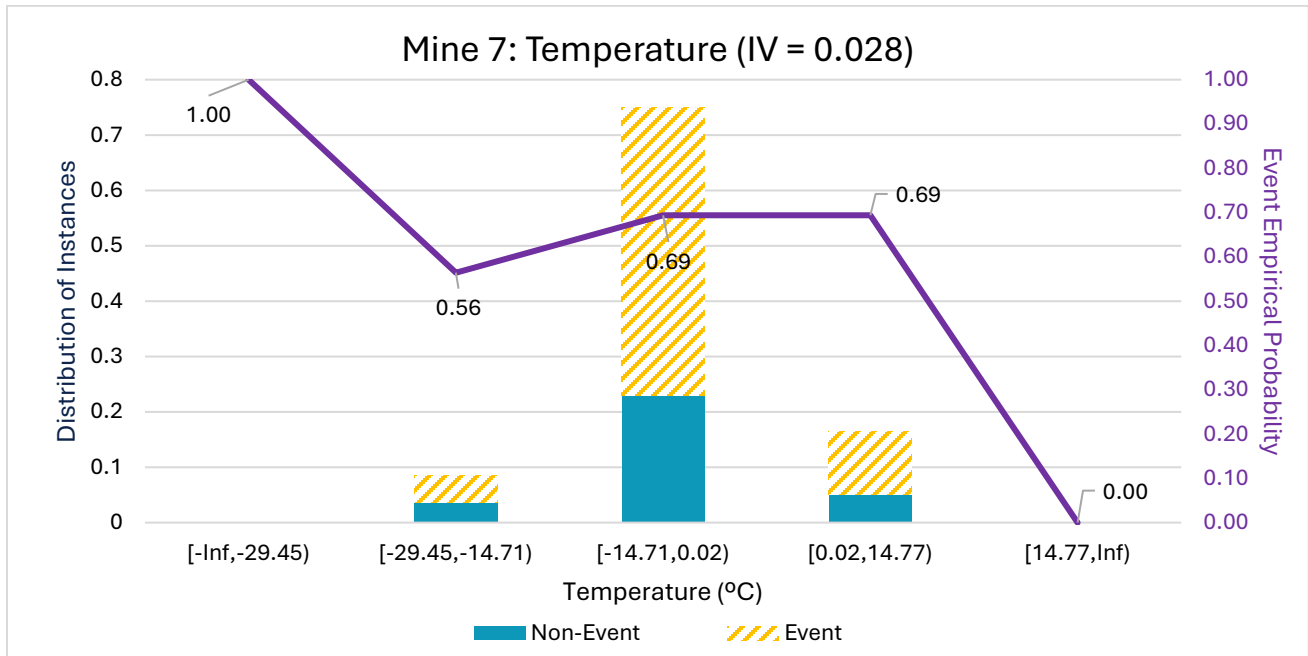


Figure B-1: Empirical Event Probability based on Distribution of Instances for Temperature at Mine 7.

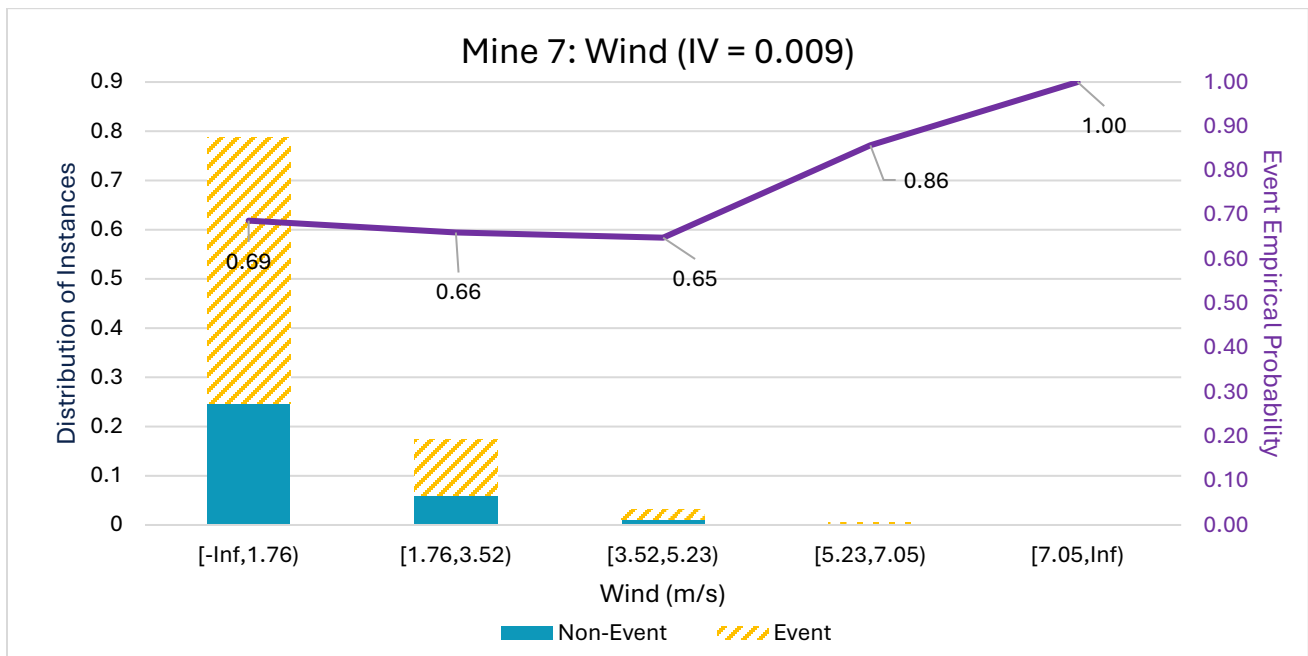


Figure B-2: Empirical Event Probability Based on Distribution of Instances for Wind at Mine 7.

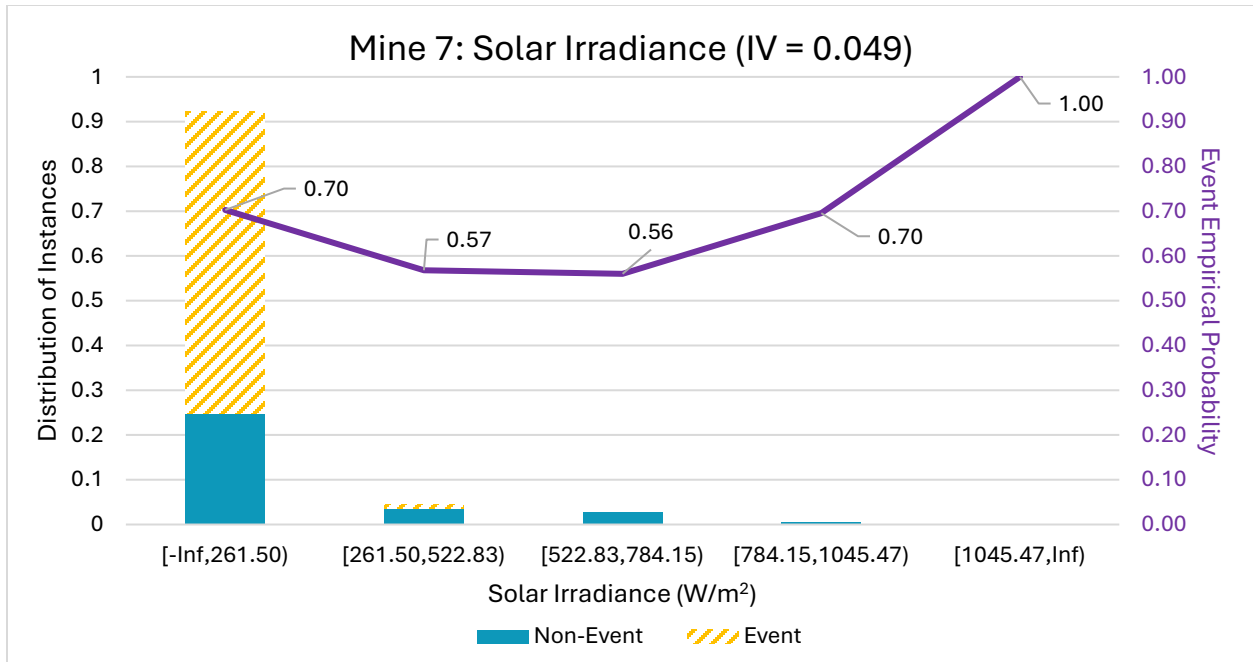


Figure B-3: Empirical event probability based on distribution of instances for solar irradiance at Mine 7.

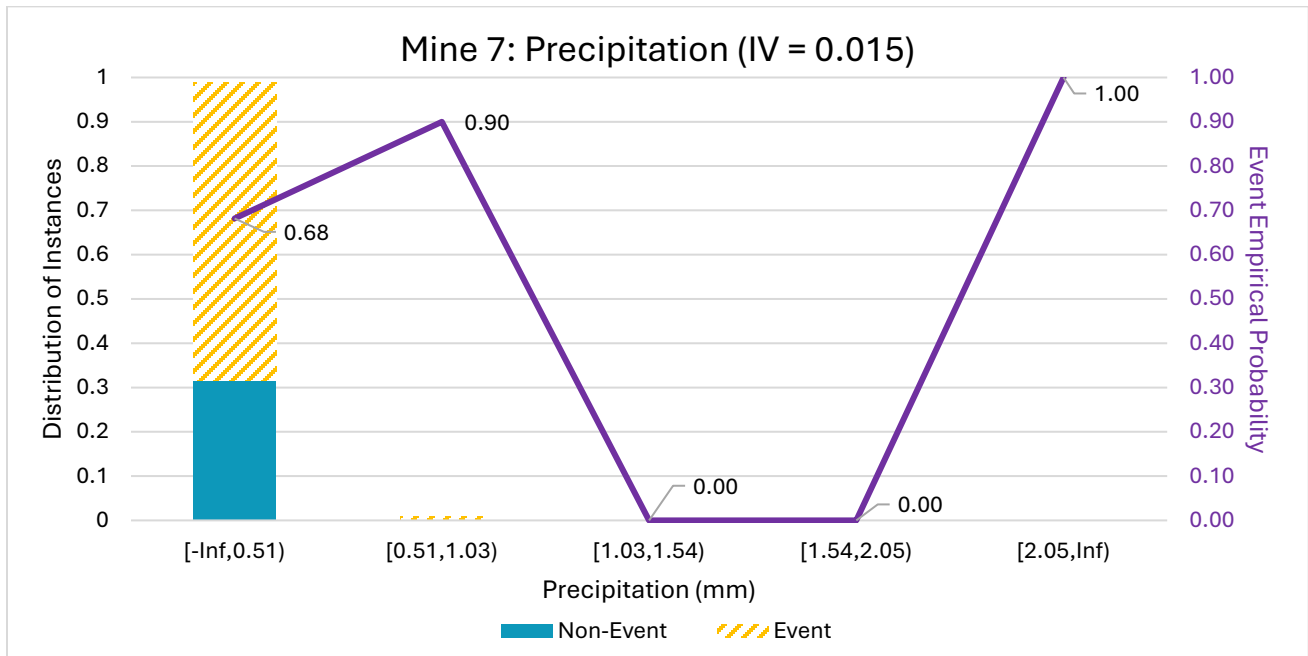


Figure B-4: Empirical event probability based on distribution of instances for precipitation at Mine 7.

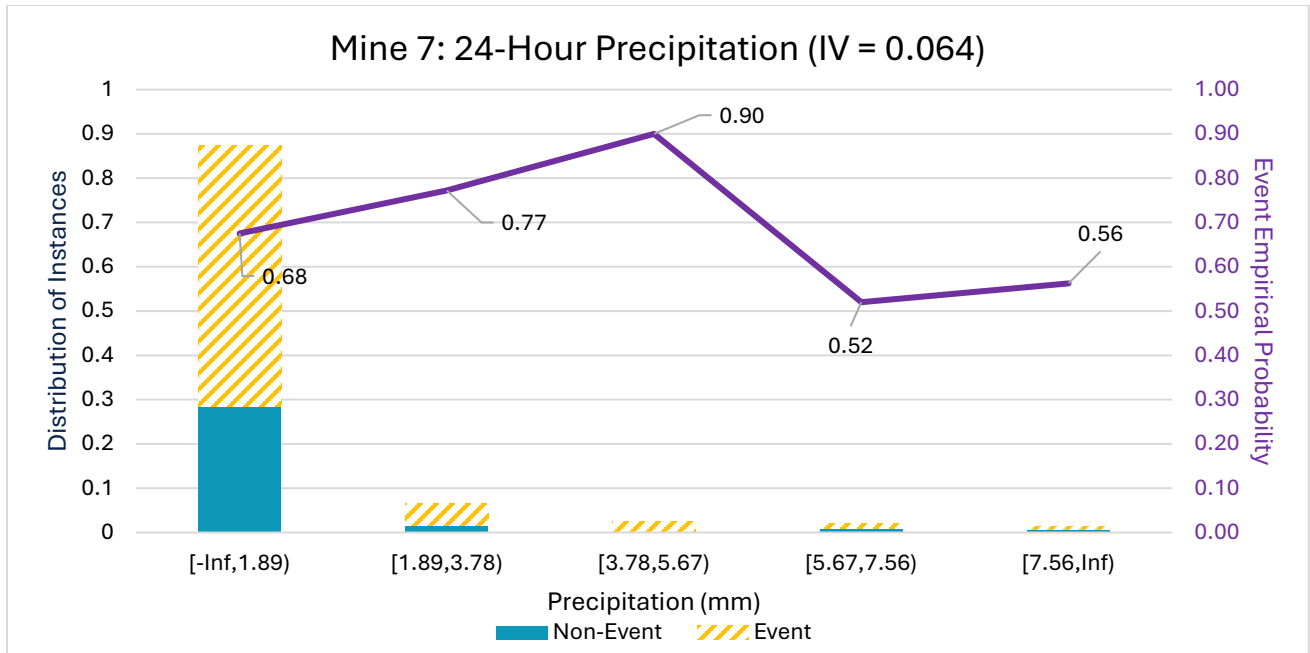


Figure B-5: Empirical Event Probability Based on Distribution of Instances for 24-Hour Precipitation at Mine 7.

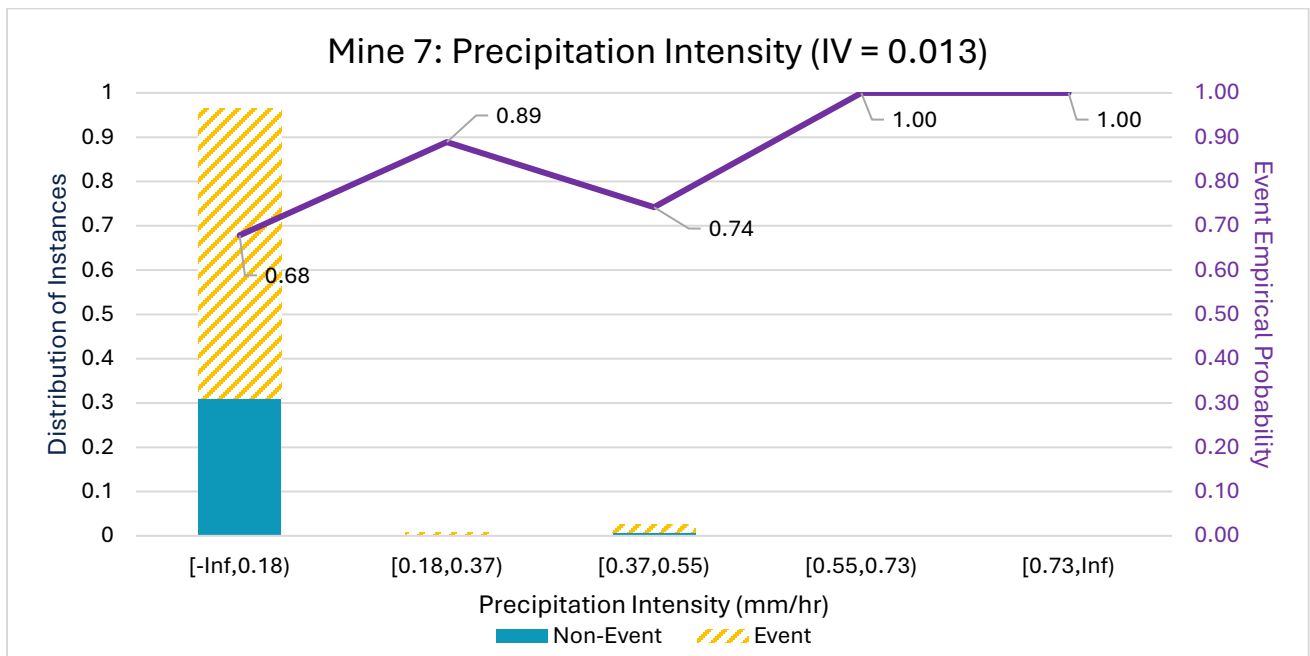


Figure B-6: Empirical Event Probability Based on Distribution of Instances for Precipitation Intensity at Mine 7.

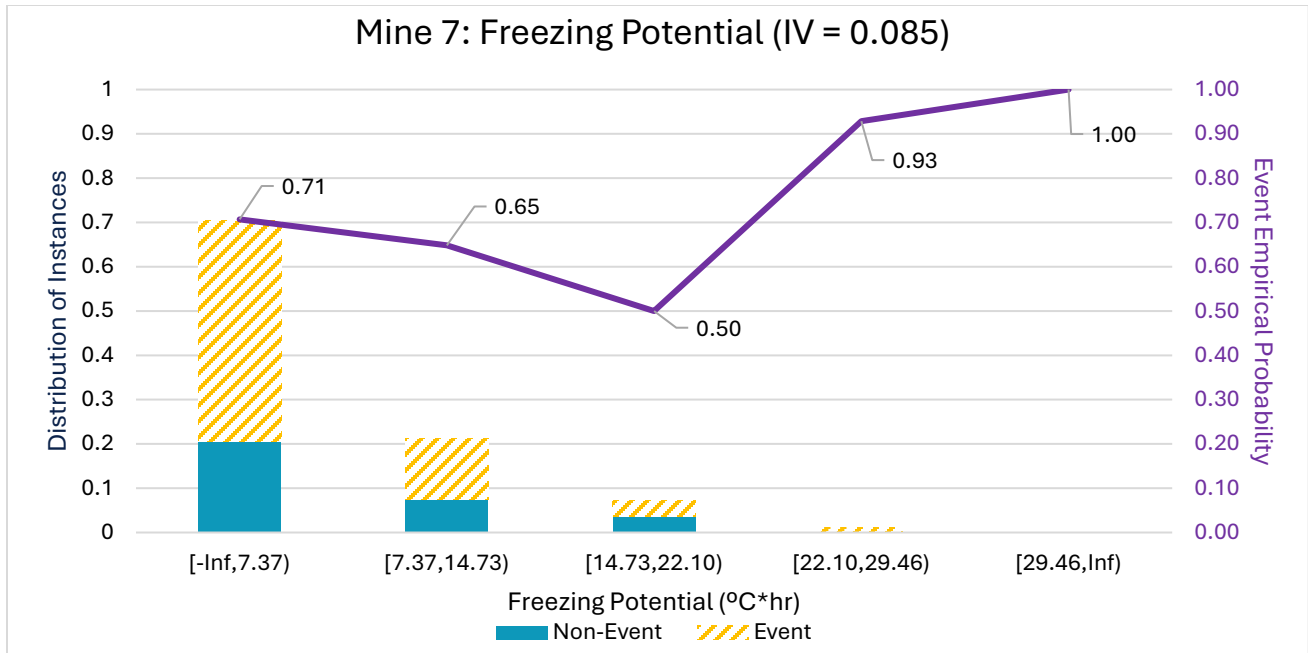


Figure B-7: Empirical Event Probability Based on Distribution of Instances for Freezing Potential at Mine 7.

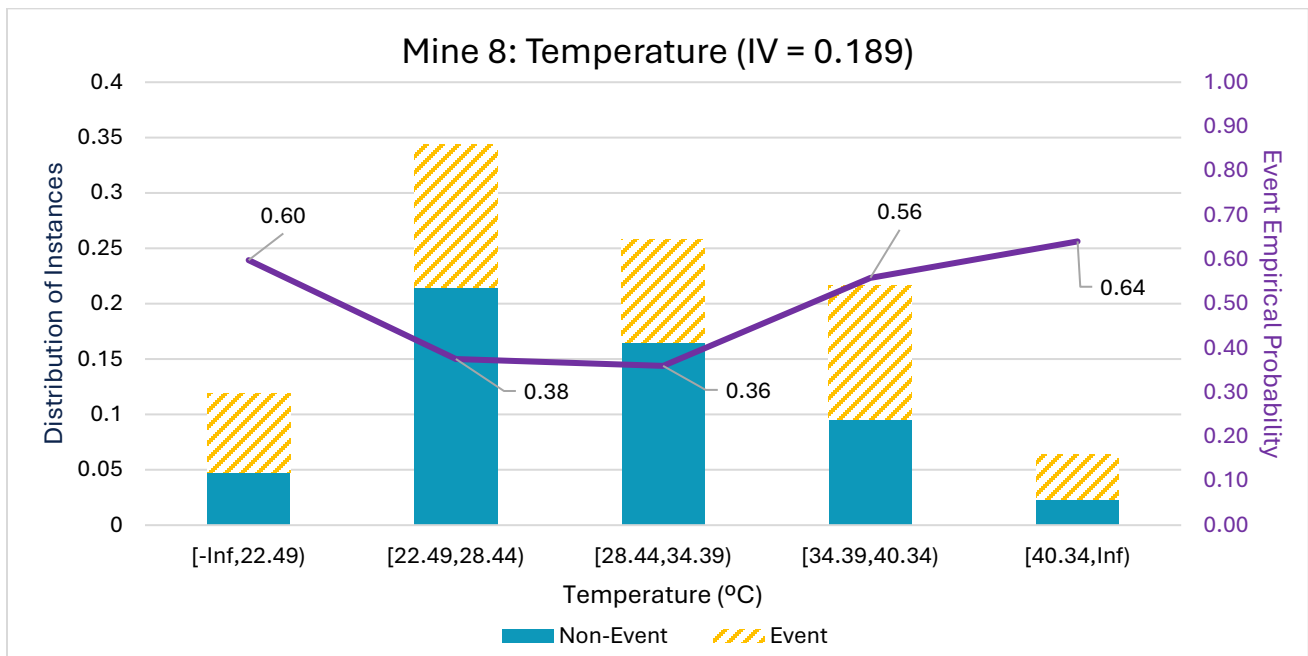


Figure B-8: Empirical Event Probability Based on Distribution of Instances for Temperature at Mine 8.

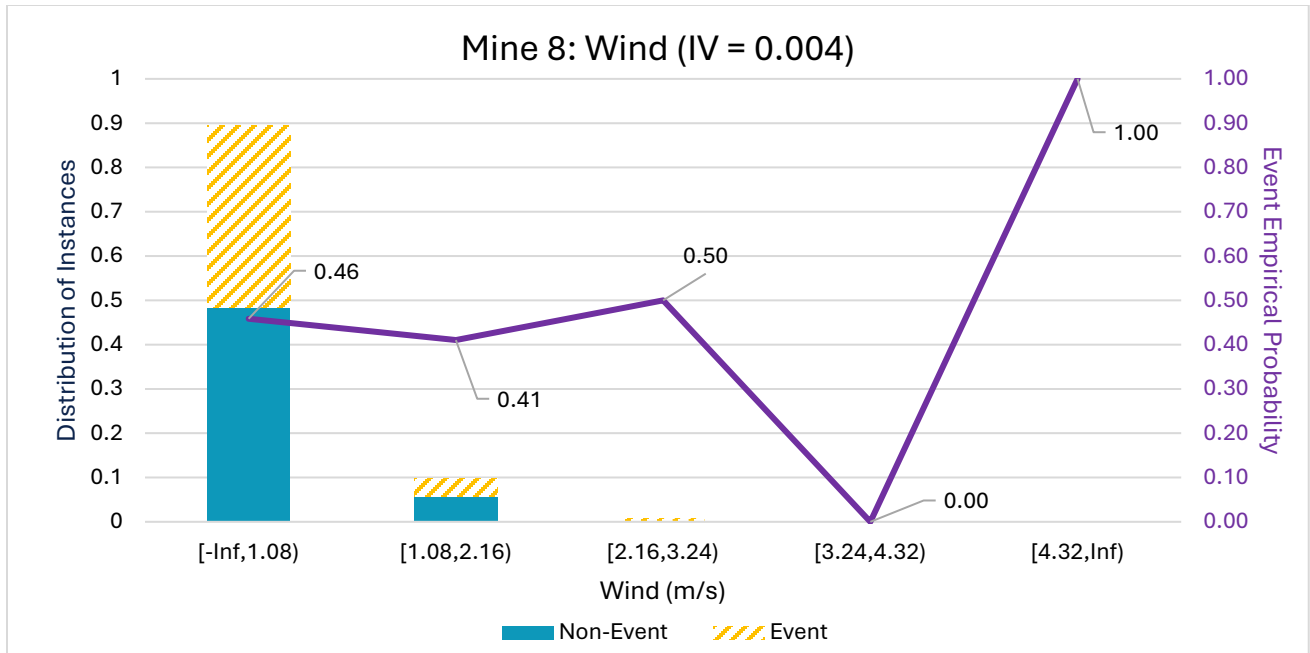


Figure B-9: Empirical Event Probability Based on Distribution of Instances for Wind at Mine 8.

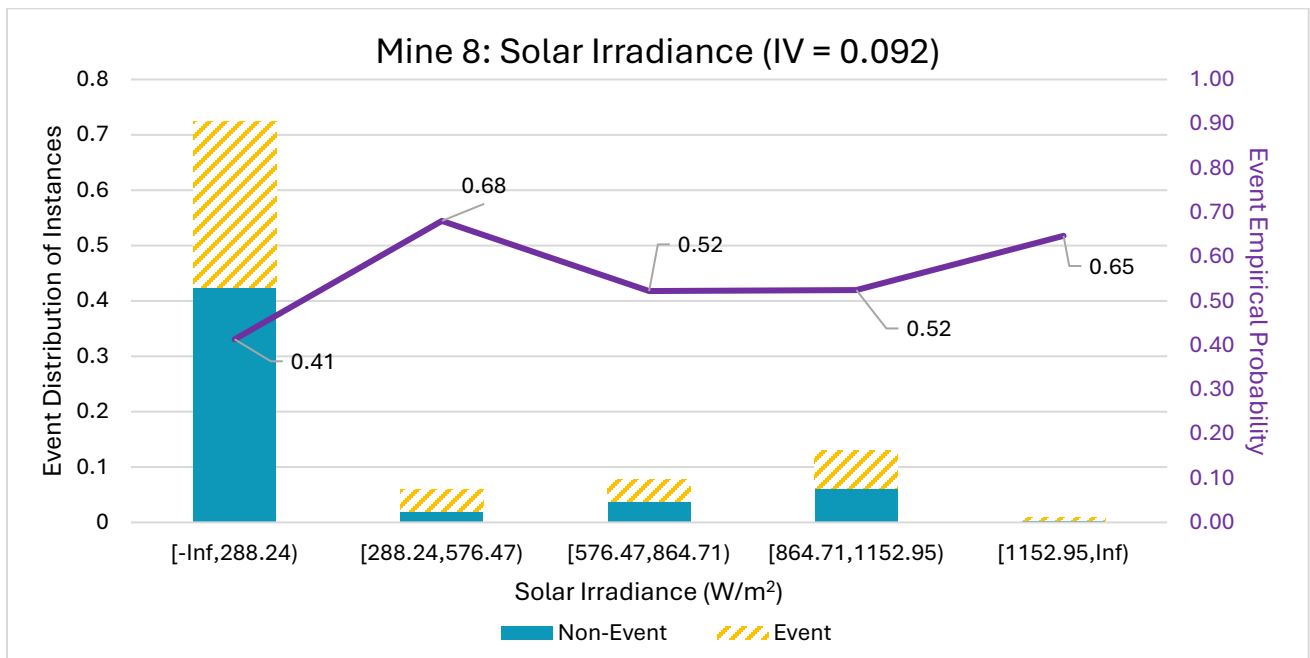


Figure B-10: Empirical Event Probability Based on Distribution of Instances for Solar Irradiance at Mine 8.

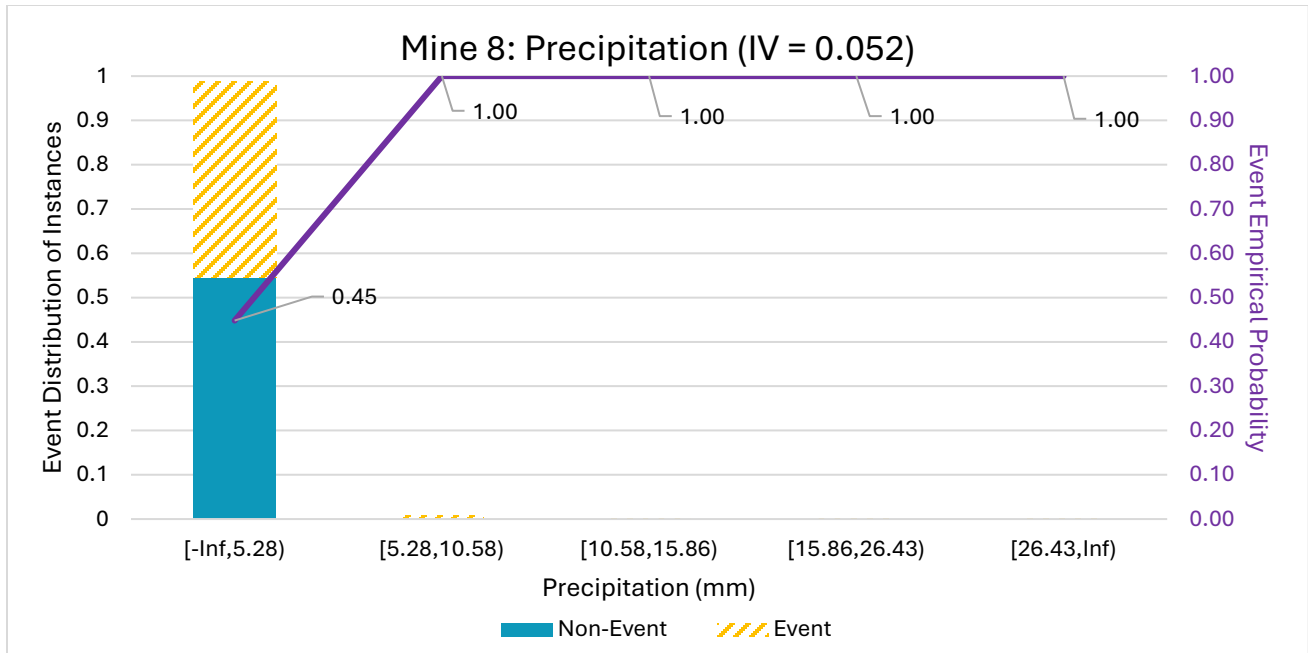


Figure B-11: Empirical Event Probability Based on Distribution of Instances for Precipitation at Mine 8.

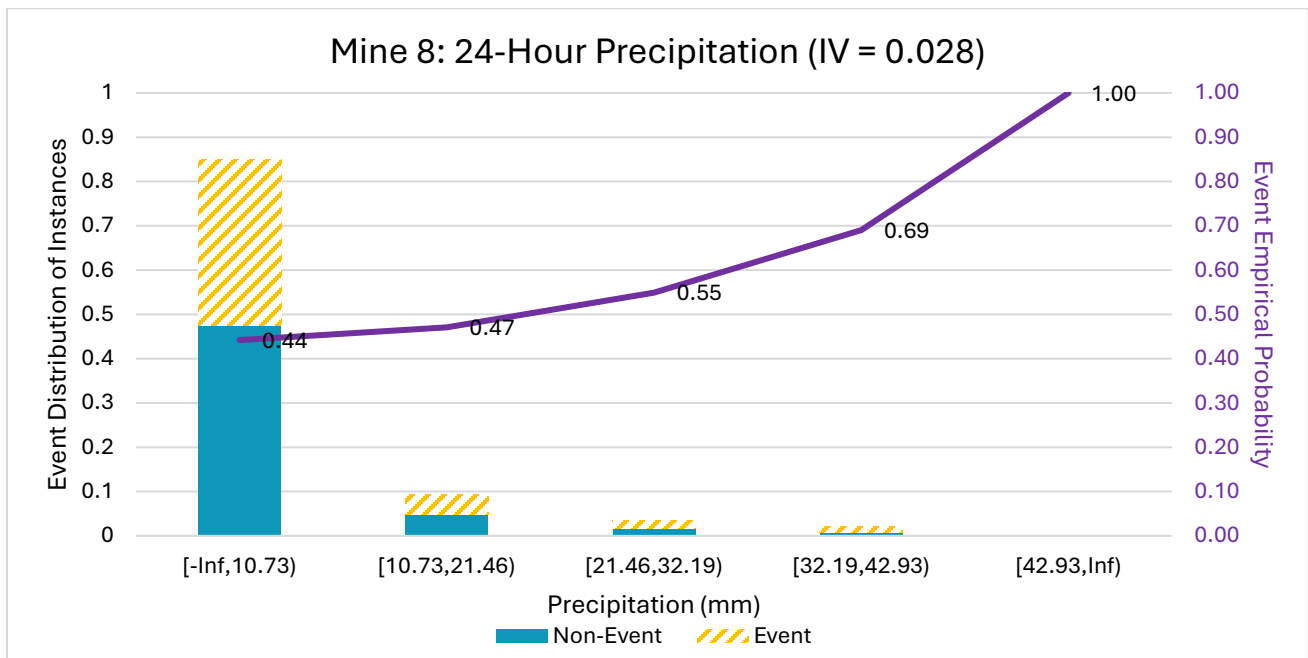


Figure B-12: Empirical Event Probability Based on Distribution of Instances for 24-hour Precipitation at Mine 8.

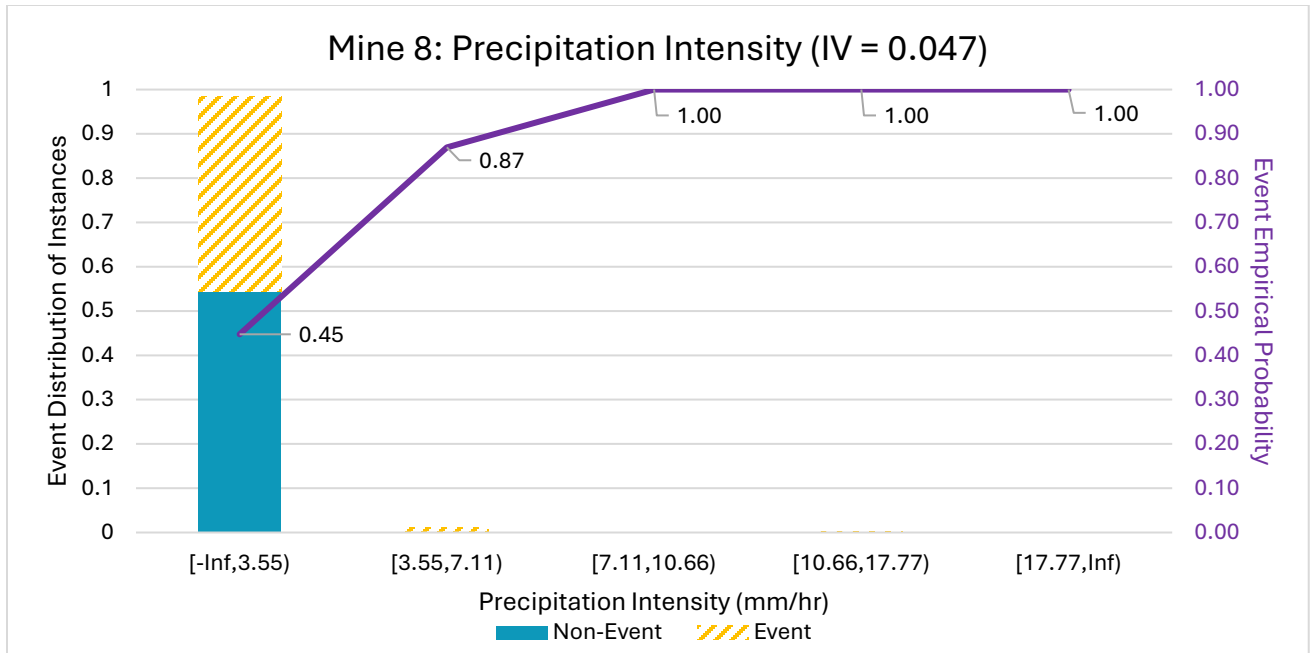


Figure B-13: Empirical Event Probability Based on Distribution of Instances for Precipitation Intensity at Mine 8.

B.3 Logistic Regression Outputs

Table B-4: Calculated P-Values of Parameters Fit to Logistic Regression Model for Mine 7. Trend reflects how each value in each bin is changing in time relative to the previous value. Significance values denoted by asterisks. See Figure X for example time series of trends.

Parameter	Interval	P-Values ¹		
		Increasing Trend	Decreasing Trend	Static Trend
Freezing Potential (°C*hour)	0 to 5.89	0.159	NA	0.088
	5.89 to 11.78	0.25	0.285	NA
	11.78 to 17.68	0.438	0.932	NA
	17.68 to 23.57	0.23	0.973	NA
	23.57 to 29.46	0.98	0.837	NA
Temperature (°C)	-29.45 to -20.61	0.93	NA	NA
	-20.61 to -11.76	0.838	0.42	NA
	-11.76 to -2.92	0.192	NA	0.786
	-2.92 to 5.93	0.343	0.658	NA
	5.93 to 14.77	NA	NA	0.682
Rolling Sum of Precipitation in Previous 24 Hours (mm)	0 to 1.89	0.054	NA	0.003**
	1.89 to 3.78	0.011*	0.473	0.811
	3.78 to 5.68	0.381	0.993	0.543
	5.68 to 7.57	0.001***	0.985	0.06
	7.57 to 9.46	0.786	0.001***	0.993
Solar Irradiance (W/m ²)	0.01 to 11.83	0.001***	NA	0.355
	11.83 to 23.65	0.665	0.077	NA
	23.65 to 35.48	0.108	0.058	NA
	35.48 to 47.31	0.354	0.787	NA
	47.31 to 59.14	0.85	0.986	NA

1: * $p < .05$, ** $p < 0.01$, *** $p < 0.001$

Table B-5: Calculated P-Values of Parameters Fit to Logistic Regression Model for Mine 8. Trend reflects how each value in each bin is changing in time relative to the previous value. Significance values denoted by asterisks. See Figure X for example time series of trends.

Parameter	Interval	P-Values ¹		
		Increasing Trend	Decreasing Trend	Static Trend
Rolling Sum of Precipitation Past 24 Hours (mm)	0 to 3.38	0.174	NA	0.288
	3.38 to 6.76	0.674	0.333	0.17
	6.76 to 10.14	0.175	0.033*	0.074
	10.14 to 13.52	0.989	0.993	0.81
	13.52 to 16.9	0.988	0.584	0.286
Precipitation Intensity (mm/hr)	0 to 1.40	0.607	NA	0.468
	1.40 to 2.80	0.986	NA	0.261
	2.80 to 4.20	0.999	NA	NA
	4.20 to 5.60	NA	NA	NA
	5.60 to 7.0	0.992	NA	1
Solar Irradiance (W/m ²)	0 to 16.61	0.001***	NA	0.01**
	16.61 to 33.22	0.001***	0.004**	NA
	33.22 to 49.83	0.015*	0.235	NA
	49.83 to 66.44	0.028*	NA	NA
	66.44 to 83.0	0.002**	NA	NA
Temperature (°C)	16.54 to 22.49	0.003**	0.001***	0.94
	22.49 to 28.44	0.818	0.001***	0.994
	28.44 to 34.39	0.161	0.413	0.995
	34.39 to 40.34	0.298	0.887	0.994
	40.34 to 62.83	0.136	NA	0.357
Precipitation (mm)	0 to 2.29	0.98	0.995	NA
	2.29 to 4.58	0.99	NA	NA
	4.58 to 6.87	0.996	NA	NA
	6.87 to 9.16	NA	NA	NA
	9.16 to 11.45	0	0	0

1: * $p < .05$, ** $p < 0.01$, *** $p < 0.001$

B.4 Meteorological Summaries

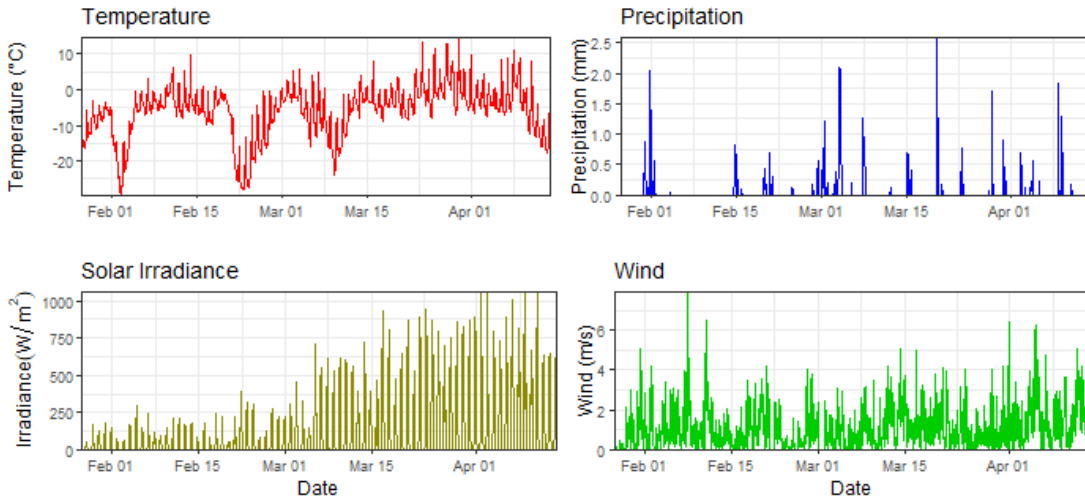


Figure B-14: Time Series of Meteorological Conditions over the Course of Deployment – Mine 7

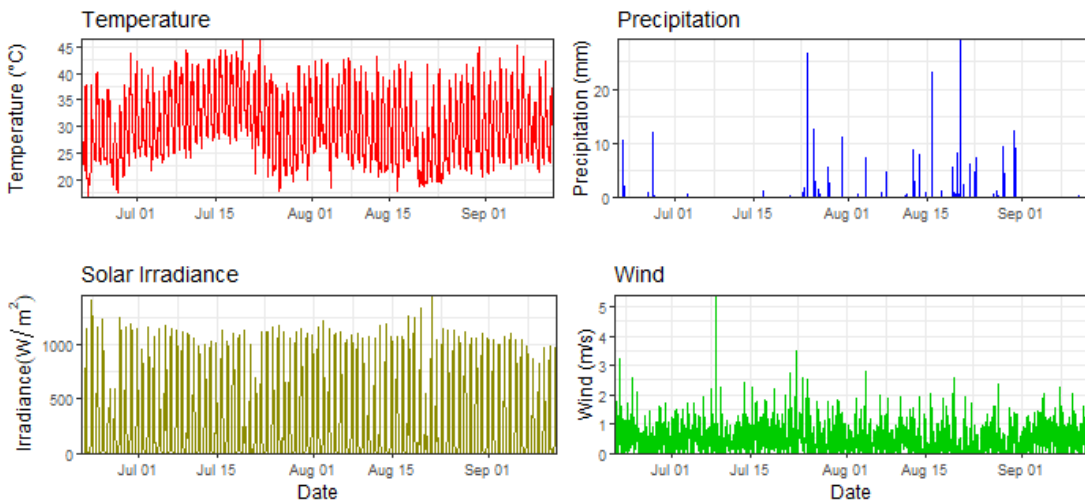


Figure B-15: Time Series of Meteorological Conditions over the Course of Deployment – Mine 8

B.5 Meteorological Trends

Meteorological trends were determined by considering how each data point changes in reference to the preceding data point.

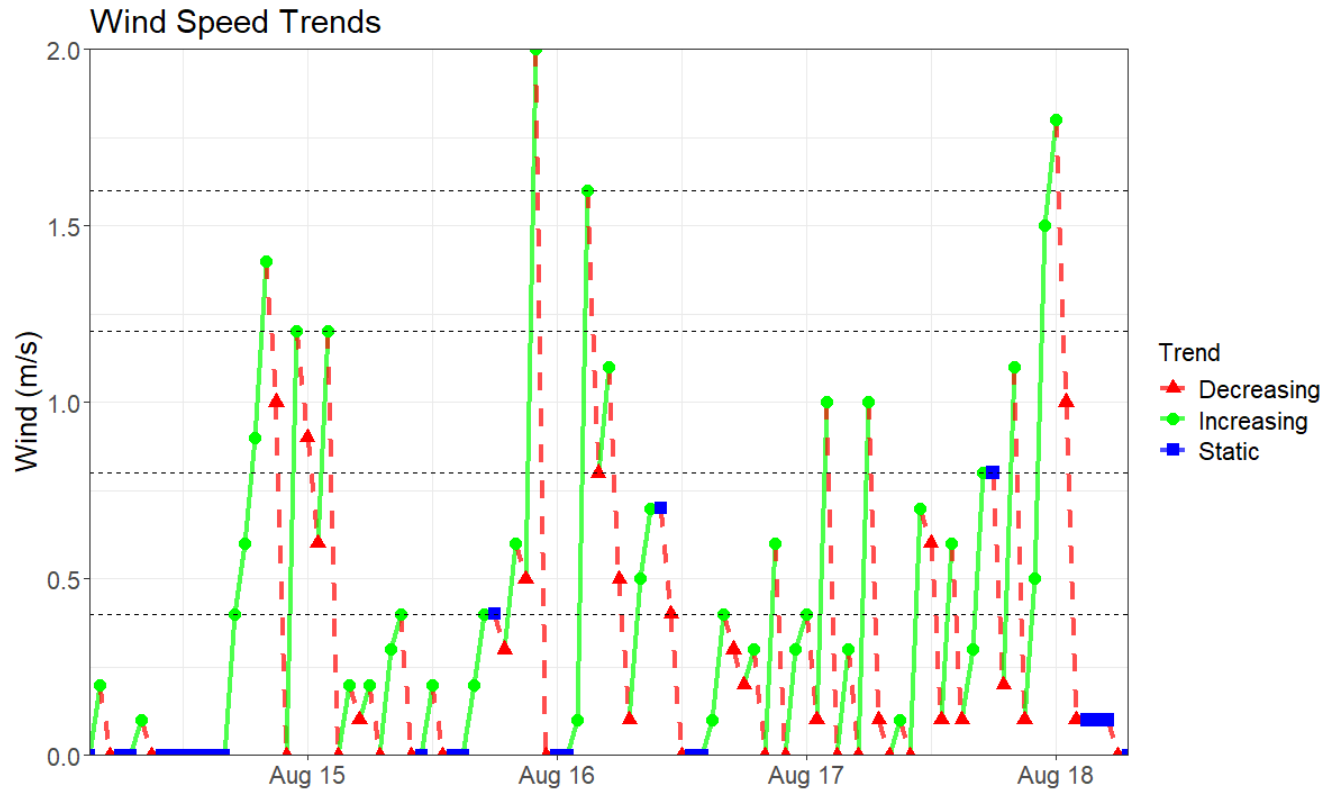


Figure B-17: Example Visualization of 20% Bins Schema and Trends Based on Wind at Mine 8.

B.6 Receiver Operating Characteristic Curves

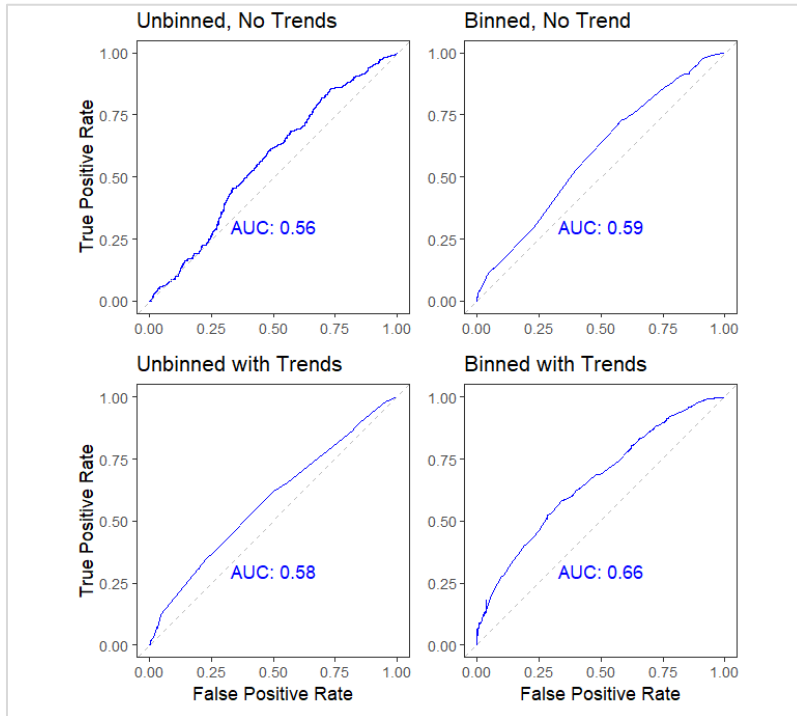


Figure B-18: Mine 7 Receiver Operating Characteristic curve for each logistic regression model.

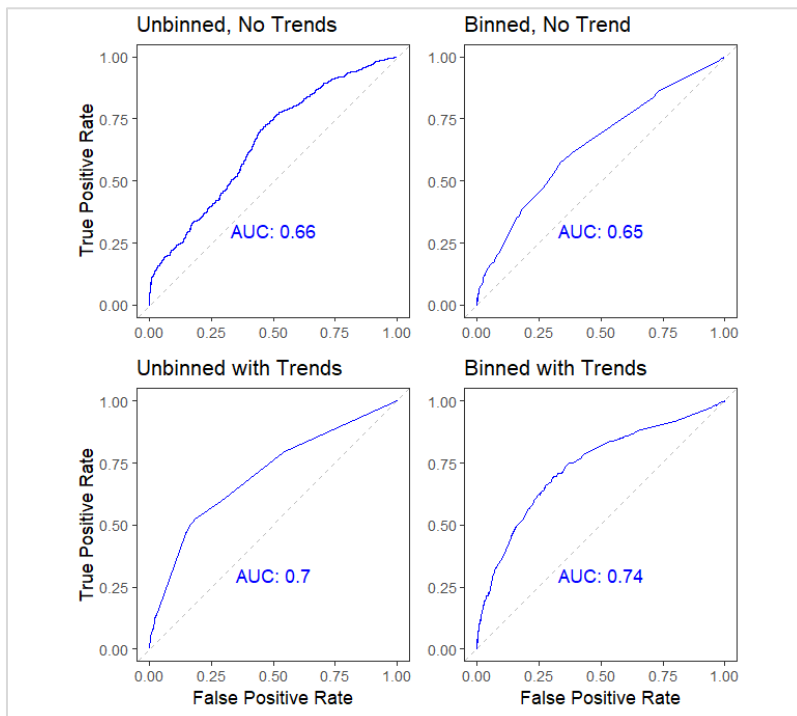


Figure B-19: Mine 8 Receiver Operating Characteristic curve for each logistic regression model.

B.7 Coefficients, Odds Ratio, P-Values, and Confidence Intervals for Preliminary Model Runs.

Table B-6: Odds ratios, confidence intervals, and p-values for Mine 7, bins only

Parameter	Interval	OR	CI(95%)	P-Value
Freezing Potential (°C*hour)	0 to 5.89	--	--	--
	5.89 to 11.78	0.84	0.61	0.32
	11.78 to 17.68	0.88	24.07	0.93
	17.68 to 23.57	0.88	27.86	0.94
	23.57 to 29.46	2.27	182.67	0.69
Temperature (°C)	-29.45 to -20.61	1.49	64.52	0.82
	-20.61 to -11.76	0.71	19.24	0.82
	-11.79 to -2.92	--	--	--
	-2.92 to 5.93	1.00	0.74	0.99
	5.93 to 14.77	1.10	2.12	0.83
Rolling Sum of Precipitation in Previous 24 Hours (mm)	0 to 1.892	--	--	--
	1.892 to 3.784	1.54	1.91	0.14
	3.784 to 5.676	4.15	16.13	0.021 *
	5.676 to 7.568	0.46	0.85	0.06
	7.568 to 9.46	0.52	1.29	0.20
Solar Irradiance (W/m2)	0 to 11.827	--	--	--
	11.827 to 23.653	0.55	0.53	0.01*
	23.653 to 35.481	0.40	0.40	0.001***
	35.481 to 47.307	0.63	0.95	0.19
	47.307 to 59.145	1.10	3.64	0.88

Table B-7: Odds ratios, confidence intervals, and p-values for Mine 7, untrended, no binning

Parameter	OR	CI(95%)	P-Value
Temperature	1.0229601	0.155	0.5538
Solar Irradiance (W/m2)	0.9988511	0.021	0.001**
Rolling Sum of Precipitation in Previous 24 Hours (mm)	0.9954998	0.155	0.91
Freezing Potential (°C*hour)	0.9927684	0.169	0.87

Table B-8: Odds ratios, confidence intervals, and p-values for Mine 7, trended, no binning

Parameter	OR			CI(95%)			P-Value		
	Increasing Trend	Decreasing Trend	Static Trend	Increasing Trend	Decreasing Trend	Static Trend	Increasing Trend	Decreasing Trend	Static Trend
Freezing Potential (°C*hour)	1.74	--	1.84	2.69	--	2.02	0.12	--	0.02*
Temperature (°C)	1.38	--	1.91	1.99	--	40.61	0.34	--	0.59
Rolling Sum of Precipitation in Previous 24 Hours (mm)	0.49	--	0.53	0.78	--	0.69	0.06	--	0.049*
Solar Irradiance (W/m2)	1.59	--	0.00	0.85	--	--	0.00	--	0.97

Table B-9: Odds ratios, confidence intervals, and p-values for Mine 8, bins only

Parameter	Interval	OR	CI(95%)	P-Value
Precipitation Intensity (mm/hr)	0 to 3.55	--	--	--
	3.55 to 7.11	3.51	12.04	0.06
	7.11 to 10.66	1.46	--	1.00
	10.66 to 14.21	--	--	--
	14.21 to 17.77	381178.9	--	0.99
Temperature (°C)	16.54 to 22.49	--	--	0.82
	22.49 to 28.44	0.42	0.26	0.00
	28.44 to 34.39	0.34	0.23	0.00
	34.39 to 40.34	0.73	0.59	0.12
	40.34 to 46.30	1.08	1.19	0.77
Rolling Sum of Precipitation in Previous 24 Hours (mm)	0 to 8.59	--	--	--
	8.59 to 17.17	1.11	0.69	0.50
	17.17 to 25.76	0.77	0.85	0.32
	25.76 to 34.34	2.22	2.94	0.01
	34.34 to 42.93	1.85	2.90	0.09
Solar Irradiance (W/m2)	0 to 288.24	--	--	--
	288.24 to 576.47	2.66	2.41	0.00
	576.47 to 864.71	1.00	0.85	0.99
	864.71 to 1152.92	1.04	0.75	0.84
	1152.95 to 1441.18	2.15	5.38	0.15
Precipitation (mm)	0 to 5.82	--	--	--
	5.82 to 11.63	2372164	3.32E+305	0.97
	11.63 to 17.45	4286261	--	0.98
	17.45 to 23.27	19.44	--	1.00
	23.27 to 29.08	5.92	--	1.00

Table B-10: Odds ratios, confidence intervals, and p-values for Mine 8, untrended, no binning

Parameter	OR	CI(95%)	P-Value
Temperature	0.99	0.041	0.22643
Solar Irradiance (W/m2)	1.00	0.001	0.0001***
Precipitation (mm)	3.42	8.939	0.01*
Rolling Sum of Precipitation in Previous 24 Hours (mm)	1.02	0.024	0.001**
Precipitation Intensity (mm/hr)	1.69	1.401	0.001**

Table B-11: Odds ratios, confidence intervals, and p-values for Mine 8, trended, no binning

Parameter	OR			CI(95%)			P-Value		
	Increasing Trend	Decreasing Trend	Static Trend	Increasing Trend	Decreasing Trend	Static Trend	Increasing Trend	Decreasing Trend	Static Trend
Precipitation Intensity (mm/hr)	4.07	--	1.00	34.48	--	2.33	0.15	--	1.00
Temperature (°C)	2.36	--	1.60	0.96	--	13.49	0.00	--	0.65
Precipitation (mm)	2.02	--	0.54	4.47	--	1.39	0.14	--	0.25
Rolling Sum of Precipitation in Previous 24 Hours (mm)	0.62		0.50	1.47		1.17	0.35		0.17
Solar Irradiance (W/m2)	2.19	--	0.00	0.85	--	NA	0.00	--	0.97

Appendix C: Data Access

The data used in Phase 2 of the thermal project will be stored by the University of Arizona for a period of at least 4 years. This data can include, but is not limited to, unprocessed thermal video, weather data, rockfall detection algorithm output, camera calibration data, and tables of analyses. Ownership of original video materials remains with the mine sites at which video was collected, and availability of these videos may vary based on confidentiality and privacy agreement terms with various site operators. Please contact project primary investigators with any questions about data ability or the use of data from this BAA for further research. The online data repository is accessible at the following URL:

https://data.cyverse.org/dav-anon/iplant/projects/rockfall/NIOSH_Thermal_imaging_data/Phase2DataRepository/